Universität Stuttgart
Institut für Strömungsmechanik und
Hydraulische Strömungsmaschinen

J. Wack

Numerical Investigation of the Full Load Instability in a Francis Turbine

Mitteilung Nr. 44 2020

Numerical Investigation of the Full Load Instability in a Francis Turbine

Von der Fakultät Energie-, Verfahrens- und Biotechnik
der Universität Stuttgart zur Erlangung der Würde
eines Doktors der Ingenieurswissenschaften (Dr.-Ing.)
genehmigte Abhandlung

vorgelegt von

Jonas Wack

aus Kulmbach

Hauptberichter: Prof. Dr.-Ing. S. Riedelbauch
Mitberichter: Prof. O. G. Dahlhaug

Tag der mündlichen Prüfung: 21.09.2020

Institut für Strömungsmechanik und Hydraulische
Strömungsmaschinen der Universität Stuttgart

2020

ISBN 978-3-948328-03-0

Universität Stuttgart
Institut für Strömungsmechanik und
Hydraulische Strömungsmaschinen
Pfaffenwaldring 10
D-70550 Stuttgart

Tel.: +49-711-685-63260
Fax: +49-711-685-53255
Email: sekretariat@ihs.uni-stuttgart.de
http://www.ihs.uni-stuttgart.de

D 93 Stuttgart

Schau ganz tief in die Natur,
und dann verstehst Du alles besser.

(Albert Einstein)

Vorwort

Jeder der schon mal eine Dissertation geschrieben hat, kann sicher gut nachvollziehen, dass man den Hauptteil der Zeit in der Krise steckt. Löst man ein Problem, entstehen dadurch spätestens einen halben Tag später drei neue. In dieser Zeit ist es wirklich ein Segen sich freitags mal ins Wochenende zu verabschieden mit dem Gefühl etwas zum Laufen gebracht zu haben - auch wenn am Montag die Simulationsergebnisse zeigen werden, dass das nicht der Fall ist. Immerhin hatte man mal ein sorgenfreies Wochenende. Die ständigen Rückschläge zehren das ein ums andere Mal an der Psyche und man stellt sich immer wieder die Frage nach dem Sinn der Arbeit. Ich muss zugeben, dass ich auf dem Weg zur Fertigstellung meiner Doktorarbeit schon kurz davor war hinzuschmeißen, doch es gibt viele Menschen in meinem Umfeld, die mich auf die unterschiedlichsten Arten motiviert haben weiter zu machen oder auch einfach von den Arbeitssorgen abgelenkt haben. Bei euch allen möchte ich mich herzlich bedanken. Ohne euch hätte ich diese Arbeit niemals zu Ende gebracht.

Zunächst möchte ich mich bei Professor Stefan Riedelbauch für die Betreuung dieser Arbeit und die hilfreichen Anmerkungen zur Ausarbeitung bedanken. Danke, dass Sie mir die vielen Freiheiten gewährt haben, so dass ich dieses Dissertationsthema für mich finden konnte. I would also like to thank Professor Ole Gunnar Dahlhaug as co-rapporteur of this thesis. Tusen takk.

Vielen Dank an alle Mitarbeiter des IHS mit denen ich die letzten Jahre zusammenarbeiten durfte. Jeder hat mir auf seine Weise bei der Fertigstellung dieser Arbeit geholfen. Sei es durch hilfreiche fachliche Diskussionen und Denkanstöße, die ein oder andere Kaffepause nachdem ich mir zuvor etwas zu viele meiner "Kartoffeln" angeschaut hatte oder den sportlichen Ausgleich in der Lauf- oder Bouldergruppe. Das ein oder andere Feierabendbier hat sicherlich auch die Motivation aufrecht erhalten immer wieder ans IHS zu kommen und dort dann auch die Dissertation voranzutreiben. Vielen Dank an unsere Admins Holger und Alex. Oft sieht man nicht den Aufwand der dahinter steckt die IT des Instituts am Laufen zu halten. Ich weiß euren Einsatz sehr zu schätzen, auch wenn dabei der Server das ein oder andere Mal unnötig heruntergefahren wird. Besonders bedanken möchte ich mich bei Albert und Olli. Ihr hattet immer ein offenes Ohr für mich und habt mir viele wertvolle

Stunden eurer Arbeits- und Ruhestandszeit geschenkt um mit mir meine Instabilitätsprobleme und "Kartoffeln" zu diskutieren und viel wichtigen Input beim Korrekturlesen meiner Arbeit gegeben. Albert, bei unsren vielen Diskussionen ist mir besonders unsere philosophische Diskussion im Gedächtnis hängen geblieben, wie man die Volllastintabilität von einer Instabilität der numerischen Lösung unterscheiden kann. Und Olli, du hast mir im entscheidenden Moment den richtigen Denkanstoß gegeben. Dadurch hatte ich das große Glück, dass endlich alles zusammengepasst hat und nach dem Lösen des Problems tatsächlich statt der typischen neuen Probleme endlich die Erkenntnis da war. Vielen Dank dafür! Und dann noch vielen Dank an Caleb, dafür dass du mir die wichtigsten Seiten dieser Arbeit sprachlich korrekturgelesen hast.

Die Grundidee für diese Dissertation entstand im Rahmen des EU-Projektes HYPERBOLE. I would like to thank all involved project partners for the many fruitful discussions, especially during the CFD workshops. Special thanks to the PhD students of the EPFL. You gave me a lot of important input for the use of the experimental data.

Und dann möchte ich mich noch bei meinen Freunden und meiner Familie bedanken. Ihr wart in den letzten Jahren immer für mich da und habt mich gerade in Zeiten des größten Zweifelns wieder aufgebaut und mir gezeigt, dass es wichtigere Dinge im Leben gibt als Volllastinstabilitäten. Ihr habt zwar fachlich keinen Beitrag zu dieser Arbeit geleistet, doch habe ich nur durch eure Hilfe nicht hingeschmissen. Ohne euch hätte ich diese Arbeit nie zu Ende gebracht. Besonderer Dank gilt Carina, David, Hanna und Felix. Es ist ein Wunder, dass ich trotz der vielen Besuche bei euch mein Gewicht im Zeitraum der Dissertation nicht verdoppelt habe. Und natürlich vielen vielen Dank Mama, Papa, Johanna, Ralf und Anton. Ihr habt mich die ganze Zeit unterstützt und an mich geglaubt. Ihr habt zwar wahrscheinlich keine Ahnung was genau ich die letzten Jahre genau untersucht habe, aber das ist ja auch egal.

Abstract

For the integration of volatile renewable energies like wind or photovoltaics, hydropower plants received increased attention due to their suitability to stabilize the electrical grid. Thus, turbines are often operated at off-design conditions where undesirable flow phenomena like the full load instability can occur. It is of great importance to understand these phenomena in order to assess their hazard potential and consequently define an appropriate operating range. Even though the physical mechanism behind the full load instability has been investigated in the past, it has not been fully understood to this day. For that reason, the main goal of this thesis is to close this gap and develop a complete understanding of this phenomenon.

By means of numerical simulations a Francis turbine was analyzed at full load in the region of the instability onset. First, it was investigated for constant cavitation numbers how characteristic quantities like pressure, swirl number or cavitation volume differ between stable and unstable conditions. In the second step, the transition from stable to unstable conditions was investigated by gradually decreasing the pressure. It was then concluded that the full load instability is a result of the interaction between cavitation on the runner blades and the cavitating draft tube vortex. The negative damping of the oscillation is a result of the pressure oscillations traveling at the speed of sound, while swirl variations are transported with the flow. Furthermore, oscillations of the cavitation volume generate pressure fluctuations. All in all, an explanation for the physical mechanism behind the full load instability is given.

Kurzfassung

Zur Integration volatiler erneuerbarer Energien wie Wind oder Photovoltaik werden Wasserkraftwerke immer häufiger dafür verwendet Netzschwankungen auszugleichen. Dabei werden diese oft in Betriebspunkten abseits des Auslegungspunktes betrieben, in denen es zum Auftreten ungewollter Strömungsphänomene, wie zum Beispiel der Volllastinstabilität, kommen kann. Es ist von großer Bedeutung diese Phänomene zu verstehen, um deren Gefahrenpotential abzuschätzen und somit einen sinnvollen Betriebsbereich für eine Turbine zuzulassen. Der Entstehungsprozess der Volllastinstabilität wurde zwar in der Vergangenheit untersucht, allerdings gibt es bis heute keine vollständige Erklärung für dieses Phänomen. Daher war es Ziel der Arbeit diese Wissenslücke zu schließen.

Mit Hilfe numerischer Strömungssimulationen wurde eine Francis-Turbine untersucht, bei der die Volllastinstabilität auftritt. Dabei wurde zunächst bei Vorgabe eines konstanten Druckniveaus untersucht, wie sich charakteristische Größen (z.B. Druck, Drallzahl, Kavitationsvolumen) zwischen stabilen und instabilen Bedingungen unterscheiden. Im zweiten Schritt wurde der Übergang von stabilen zu instabilen Bedingungen durch gleichmäßige Druckabsenkung untersucht. Daraus konnte eine Erklärung abgeleitet werden wie es zur Entstehung der Volllastinstabilität kommt. Dabei konnte gezeigt werden, dass die Volllastinstabilität ein Resultat der Interaktion von Kavitation auf den Laufschaufeln mit dem kavitierenden Wirbelzopf ist. Zum Aufschwingen kommt es, weil sich Druckschwankungen mit Schallgeschwindigkeit ausbreiten, während Dralländerungen mit der Strömung transportiert werden und außerdem Oszillationen des Kavitationsvolumens wiederum Druckschwingungen generieren.

Contents

List of Variables

Latin Letters

a	s^{-2}	Model parameter for self-oscillation
A	m^2	Area
b	s^{-2}	Model parameter for self-oscillation
c	s	Model parameter for self-oscillation
c	m	Chord length
c_m	m/s	Meridional velocity component
c_p	$-$	Pressure coefficient
c_u	m/s	Circumferential velocity component
C_c	m^2	Cavitation compliance: $C_c = \partial V_c / \partial h$
C_D	$-$	Drag coefficient
C_1	$-$	Coefficient for negatively damped linear oscillation
C_2	$-$	Coefficient for negatively damped linear oscillation
d	m	Diameter
$D_{\bar{1}}$	m	Outer runner outlet diameter
f_s	$-$	Shielding function
F_c	$-$	Empirical calibration coefficient for cavitation model
F_D	N	Drag force
F_e	$-$	Empirical calibration coefficient for cavitation model
g	$\mathrm{m/s}^2$	Gravity
G_{ang}	$\mathrm{m}^5/\mathrm{s}^2$	Axial flux of angular momentum
G_{ax}	$\mathrm{m}^5/\mathrm{s}^2$	Axial flux of axial momentum
h	m	Piezometric head state variable
h_m	m	Maximum thickness of NACA0009 hydrofoil
H	m	Head
n	min^{-1}	Rotational speed
n_q	min^{-1}	Specific speed

n_{ED}	min^{-1}	Speed factor: $n_{ED} = nD/\sqrt{gH}$
p	Pa	Pressure
p_a	Pa	Acoustic pressure
p_{vap}	Pa	Vapor pressure
q	m	Deflection
Q	m^3/s	Discharge
Q_{ED}	$-$	Discharge factor: $Q_{ED} = Q/(D^2\sqrt{gH})$
r	m	Radius
R	m	Radius
$R_{\bar{1}}$	m	Outer runner outlet radius
Re	$-$	Reynolds number
S	$-$	Swirl number
S^{int}	$\mathrm{kg}/(\mathrm{m}^2\mathrm{s}^2)$	Interfacial source terms
St	$-$	Stokes number
t	s	Time
T	s	Period duration
T	K	Temperature
u	m/s	Velocity - x-component
u	m/s	Peripheral velocity
u_τ	m/s	Friction velocity
u_1	m/s	Runner exit peripheral velocity
U	m/s	Velocity
v	m/s	Velocity - y-component
v_S	m/s	Swirl transport velocity
V	m^3	Volume
V_c	m^3	Cavitation volume
V_{cone}	m^3	Volume of the draft tube cone
w	m/s	Velocity - z-component
w	m/s	Relative velocity
x	m	Coordinate
y	m	Distance to the nearest wall
y	m	Coordinate
y^+	$-$	Dimensionless wall distance

y_0	$-$	Amplitude
Δy	$-$	Shift for negatively damped linear oscillation
z	m	Coordinate

Greek Letters

α	$^\circ$	Angle of attack
α	$-$	Volume fraction
β	$^\circ$	Relative flow angle
β_1	$^\circ$	Blade angle at runner outlet
ϵ	$\mathrm{m^3s}$	Rotational speed gain factor: $\epsilon = \partial V_c / \partial n$
γ	$-$	Swirl parameter
γ	$\mathrm{s^{-1}}$	Parameter for negatively damped oscillation
Γ	$\mathrm{kg/(m^3s)}$	Interfacial mass source
λ	m	Distance for separation of sheet cavitation
μ	kg/(ms)	Dynamic viscosity
μ_t	kg/(ms)	Eddy viscosity
ν	$\mathrm{m^2/s}$	Kinematic viscosity
ρ	$\mathrm{kg/m^3}$	Density
σ	$-$	Cavitation number
σ_P	$-$	Prandtl number
τ	$-$	Normalized tip clearance: $\tau = \frac{gap\ width}{h_m}$
τ_F	s	Characteristic time scale
τ_T	$-$	Transformed time scale
τ_V	s	Momentum response time
ϕ_0	rad	Phase
Φ	$-$	Flow coefficient
χ	s	Mass flow gain factor: $\chi = \partial V_c / \partial Q$
ψ	$\mathrm{m^2}$	Cavitation gain factor: $\psi = \partial V_c^* / \partial h$
ω	$\mathrm{s^{-1}}$	Angular frequency
ω^2	$\mathrm{s^{-2}}$	Parameter for negatively damped oscillation

Indices

b	Bubble
c	Continuous phase
c	Cavitation
d	Dispersed phase
exp	Experiment
in	Inlet
l	Liquid phase
m	Mixture
nuc	Nucleation site
out	Outlet
p	Particle
ref	Reference
rel	Relative
v	Vapor phase
∞	Reference in undisturbed conditions
1	Location runner outlet
2	Location outlet of draft tube cone

Abbreviations

BEP	Best efficiency point
CFD	Computational Fluid Dynamics
CO_2	Carbon dioxide
DNS	Direct Numerical Simulation
DT	Draft tube
EVM	Eddy Viscosity Model
GGI	General Grid Interface
LDA	Laser Doppler Anemometry
LED	Light-emitting diode
LES	Large Eddy Simulation
M	Million (mesh size)

MDR	Maximum Density Ratio
MUSIG	Multiple size group
NACA	National Advisory Committee for Aeronautics
PIV	Particle Image Velocimetry
RANS	Reynolds Averaged Navier Stokes
RMS	Root Mean Square
RSM	Reynolds Stress Model
RU	Runner
SAS	Scale Adaptive Simulation
SBES	Stress Blended Eddy Simulation
SC	Spiral case
SRS	Scale Resolving Simulation
SST	Shear Stress Transport
SSTwCC	SST model with curvature correction
SVGV	Stay and guide vanes
TLV	Tip Leakage Vortex
VoF	Volume of Fluid
WALE	Wall-Adapting Local Eddy-viscosity
1D	One-Dimensional
1P	Single-Phase
2D	Two-Dimensional
2P	Two-Phase
3D	Three-Dimensional

1 Introduction

In 2017, the carbon dioxide (CO_2) emissions from fossil fuels and industry reached peak levels [82]. As the emission of greenhouse gases, like CO_2, verifiably has a relevant effect on global warming [152], the Paris Agreement was adopted in 2015. It has the goal that the global average temperature does not increase more than 2 °C compared to pre-industrial levels [161]. To achieve this goal, the peak in CO_2 emissions should not be later than 2020 and from then on the emissions should be halved every decade [135]. The most important measures to reduce CO_2 emissions are increasing energy efficiency, reforestation and the expansion of wind and solar power [160]. The latter have a huge potential to significantly increase the share of renewable energy sources in the electricity market [155].

The disadvantage of wind and solar power is that a high share of these technologies endangers electrical grid stability [157]. To compensate the imbalance caused by these technologies, hydropower can play an important role in preserving grid stability [49, 97]. However, the flexible operating range for storage power plants results in flow phenomena that are not present for the best efficiency point (BEP). At these off-design conditions, the amplitude of pressure fluctuations increases. Furthermore, cavitation may occur in the runner and draft tube due to strongly swirling flows. For the safe operation of a hydropower plant, it is crucial to limit the operating range to a region of moderate pressure fluctuations. This comes across with the necessity to investigate flow instabilities that may represent a potential risk in the operation of the power plant.

In a Francis turbine, different operating points exist that are vulnerable to severe pressure pulsations. At deep part load, the occurrence of inter-blade vortices results in severe pressure fluctuations that show a stochastic nature and could result in strong mechanical vibrations of turbine components [46]. Draft tube instabilities may be present at part load that are caused by the vortex rope rotation [108]. At high discharge, the full load instability may develop at a specific pressure level due to the interaction of cavitation in runner and draft tube. A theory of the physical mechanism behind the full load instability has been proposed by Müller [121] based on experimental results. In the scope of this work, this theory is investigated using nu-

merical simulations. The main goal is to obtain a deeper insight into the physical mechanism that results in the development of the full load instability. With this new knowledge it is possible to derive measures to suppress the instability or at least shift it to stronger off-design conditions.

1.1 State of the Art

This section is divided into three parts. The first part gives a general overview of numerical and experimental studies on cavitation in hydraulic machinery. After that, the focus lies on literature that deals specifically with the full load draft tube surge. Finally, relevant studies for the two-phase modeling are presented.

Numerical and Experimental Investigations on Cavitation in Hydraulic Machinery

Cavitation has always played an important role in the design process of hydraulic machinery. However, in former years the focus was on cavitation free conditions at best efficiency point. Consequently, a lot of numerical and experimental studies focused on non-cavitating conditions. With a more flexible operation of turbines, nowadays, cavitation phenomena can be the limiting factor of the operating range and are more and more investigated.

One operating range where high pressure fluctuations can occur is at very small discharge, also called deep part load conditions. At these conditions, inter-blade vortices can be observed in the runner that cause pressure oscillations of stochastic nature [171]. Whether these vortices cavitate, strongly depends on the speed factor n_{ED} [173]. Yamamoto et al. [174] developed a new visualization technique that enables a better optical access to the runner. While one guide vane is instrumented with a boroscope with swivel deflecting prism, the adjacent guide vanes are equipped with a power LED light source. Applying binary image processing to experimental results shows that there is a high probability that cavitating inter-blade vortices are connected to the runner hub [172]. This is in good agreement with numerical results [175]. Further simulations were performed by Conrad et al. [38] for two different cavitation numbers. They observed that the amplitude of pressure oscillations is higher for the lower cavitation number. For an accurate numerical simulation, it has been identified that a proper boundary treatment at the draft tube outlet is important due

to the strong backflow and a small time step size has to be selected. Furthermore, a fine mesh in the runner is necessary to resolve the pressure minimum in the vortex core [162]. Moreover, the selection of the turbulence model is important. While the SST model fails to predict the stochastic nature of the pressure fluctuations, the SAS model is able to resolve this flow feature [167].

Several studies on cavitation at part load operating points have been performed. A severe instability can develop at higher part load for some Francis turbines with middle and high specific speed. This phenomenon is related to an elliptical cross section of the vortex rope and can lead to severe pressure pulsations [93]. The vortex volume changes in breathing like pattern and a correlation between cavitation number and pressure fluctuations can be observed [128]. Iliescu et al. [78] conducted PIV measurements on a Francis turbine at a part load operating point. Using image processing, they estimated the rope diameter and the position of the vortex center. The highest standard deviations of investigated quantities were observed at the cavitation number, where the rope excitation coincided with one of the eigenfrequencies of the system. Further experimental investigations regarding the influence of the cavitation number were carried out by Favrel et al. [59]. They observed that with increasing cavitation number the precession frequency of the vortex rope increases only slightly, while the natural hydro-acoustic frequency of the draft tube changes significantly. When these two frequencies coincide, it comes to resonance with high pressure fluctuations. However, the velocity field is almost unaffected by the occurrence of resonance in the hydraulic system [60]. Two-phase simulations for the same turbine at higher discharge factor Q_{ED} indicate that axial and circumferential velocity distributions are influenced by the cavitation number. At this part load operating point the helical shape of the vortex rope is less pronounced, which results in regions of permanent cavitation during one vortex rope rotation that has an effect on the velocity profiles [164]. Houde et al. [75] showed with PIV measurements for a Kaplan turbine that the velocity field changes from cavitating to non-cavitating conditions.

A comparison of single-phase and two-phase simulation results indicates that neglecting the vapor phase on the one hand leads to a significant underestimation of the pressure pulsation amplitude. On the other hand the two-phase simulations show a better agreement with measurements [88]. Other studies at part load and deep part load operating points of Francis turbines [169, 182] as well as simulations for a pump turbine [104] also come to the conclusion that two-phase simulations are more accurate for the prediction of cavitating flows.

In a numerical study, Gohil and Saini [67] investigated the impact of temperature, suction head and operating point on cavitation rate and efficiency loss in a cavitating Francis turbine. The derived correlations are intended to help power plant operators to estimate reductions in performance. Two-phase simulations of a redesigned Francis runner were performed by Celebioglu et al. [28]. They observed an increased operating range with cavitation free conditions compared to the old design. The cavitation behavior of three turbines at different specific speed was analyzed by Kurosawa et al. [99]. They demonstrate that the efficiency drop that occurs when reducing the cavitation number is caused by increased losses in the draft tube.

Different types of instabilities can occur in turbomachines. Tsujimoto et al. [158] investigated the characteristics of four different instabilities: surge, rotating stall, cavitation surge and rotating cavitation. While the first two phenomena have the cause that the head-capacity curve has a positive slope, the others are characterized by a positive mass flow gain factor. Iga et al. [77] numerically analyzed three different types of surging oscillations in the presence of cavitation in a three-blade cyclic flat-plate cascade. The phenomenon with the highest oscillation amplitude could be traced back to small-vortex cavity shedding. For this phenomenon, the frequency is not affected by the cavity volume. The second phenomenon corresponds to the cavitation surge and is accompanied by cloud cavity shedding. In the last phenomenon, a system instability could be observed together with a local instability. Braisted and Brennen [20] investigated the occurrence of cavitation surge in inducers. They concluded that the instability develops when the cavitation number falls below a certain threshold. The cavitation surge is then accompanied by a dramatic increase in pressure and mass flow rate fluctuations.

Full Load Draft Tube Surge

Power swings in hydro turbines that are caused by a draft tube surge were already reported in 1940 [134]. Prénat and Jacob [131] experimentally investigated pressure pulsations in a Francis turbine at model scale that are of self-amplified nature caused by a negative damping of the oscillations [83].

Much research has been carried out to develop 1D tools to investigate surge phenomena in hydraulic systems at part load and full load operating points. All the studies are based on the key quantities mass flow gain factor and cavitation compliance that were first introduced by Brennen and Acosta [22]. An important role for the development of a full load draft tube surge is assigned to the diffusor effect of the draft

tube [31, 32, 178]. The diffusor effect enhances the occurrence of the instability as it comes to negative damping when the diffusion factor of the draft tube is bigger than the loss coefficient of the draft tube. This effect affects the whole operating range and has consequently also an impact on part load instabilities. Further experiments on the diffusor effect have been performed by Chen et al. [29, 30] that highlight that for a straight pipe no low-frequency pressure fluctuations occur that are present for a diffuser. According to Chen, the swirl effect is caused by a variation of the velocity triangle at the runner outlet when the upstream discharge changes. The swirl effect is stated to enhance instabilities for part load conditions, while it has a stabilizing impact for full load.

A dissent can be found in literature concerning the definition of the mass flow gain factor. While some researchers (e.g. [5, 63]) use the discharge downstream the cavity, it is also possible to apply the upstream discharge. A discussion on the reference discharge has been performed by Dörfler [47], who highlights that the usage of the discharge downstream the cavitation region has a strong destabilizing effect on the simulation results. By means of 3D two-phase simulations, it has been identified that using the discharge upstream of the cavity and applying a dead time that accounts for the travelling of the swirl from the runner outlet to the cavity, is a suitable reference [45]. Furthermore, the use of an upstream and downstream mass flow gain factor can be found in literature [4]. Experimental results for a micro turbine at self-oscillating conditions show significant deviations in the behavior of the discharge upstream and downstream of the cavitation region [126]. This highlights that the choice of a suitable reference is very important.

Research by Landry et al. [100] shows that due to the presence of cavitation, the wave speed in the draft tube of a Francis turbine can reduce significantly. This indicates that the convective part that is often neglected in 1D models is relevant. Based on these results, the convective part has been considered in a 1D model by Alligné et al. [6]. They concluded that the convective part has a stabilizing effect. Furthermore, the results from Chen et al. [31] confirmed that the divergent geometry of the draft tube has a destabilizing effect, while the swirl effect stabilizes the flow at full load operating point.

Extensive measurements on the self-excited pressure oscillation at full load in a Francis turbine at model scale were performed by Müller [121]. By means of LDA measurements, wall pressure measurements and high speed visualization of the vortex rope, he investigated the behavior of pressure, axial and circumferential velocity during one

cycle of cavitation volume oscillation [122]. Further visualization of cavitation on the runner blades in combination with the calculation of the swirl number indicates an interaction of vortex rope with blade cavitation [124]. The proposed physical mechanism behind the self-excited behavior is explained by a variation of cavitation on the runner blades that results in different inflow conditions into the runner that cause the oscillation of the cavitating draft tube vortex. Different numerical investigations on this Francis turbine also showed the variation of swirl number during one cycle of oscillation [21, 44]. However, in both studies only one cycle of oscillation could be evaluated as the simulations diverged at the moment of occurring pressure peak when the cavitation volume collapses. Furthermore, experimental results show that the mechanical torque varies significantly during one cycle of oscillation, which could be explained by the oscillation of vapor volume on the runner blades [123, 125]. The observation of cavitation erosion on the runner suction side close to the trailing edge in a Francis turbine prototype that is facing pressure pulsations at full load agrees with the proposed mechanism [57]. In another study, the measurements of the pressure pulsations were compared between model and prototype scale [132]. For the full load operating point, the pressure oscillations show a similar behavior. Consequently, it should be possible to transfer findings from model to prototype scale.

Different numerical studies (e.g. [34, 118]) investigate the full load pressure surge on Francis turbines at prototype scale with 3D two-phase simulations that are coupled with a 1D simulation for the rest of the hydraulic system. Chirkov et al. [35–37] investigated different measures to reduce the pressure oscillations. They concluded that the shape of the runner cone has only a negligible effect on the pressure amplitude. Significant improvements concerning pressure pulsations could be observed either for air injection with a certain mass flow or a change in the design of the runner blades that changes the velocity profiles. The runner designs with the smallest pressure oscillations are characterized by velocity profiles that have a high axial velocity and a low swirl near the hub [37]. In terms of simulation accuracy compared to measurements, Mössinger and Jung [119] concluded that a proper cavitation and turbulence modeling is important.

Two-Phase Modeling

The selection of the two-phase modeling approach depends on the application. For bubble column simulations two-fluid models are often used. Gupta and Roy [72] concluded that for the investigated application the use of a population balance approach

has no big relevance, while it is necessary to take into account lift and virtual mass force. Ničeno et al. [127] used a two-fluid model in combination with LES turbulence modeling. They emphasized the mesh requirements in Euler-Euler simulations with LES, where the grid size must be bigger than the bubbles. In another publication, numerical simulations were performed for a bubble column with a two-fluid model that takes into account mass transfer [137].

For two-phase simulations of hydraulic machinery it is common practice to use the Euler-Euler approach with simplified two-phase modeling like the homogeneous model. Nevertheless, there are some publications that use more advanced two-phase modeling approaches for applications with cavitation. There are two studies [1, 170] on Euler-Lagrange methods in cavitating flows. They state that Euler-Lagrange methods are advisable in applications with strong vortical flow as they can capture the bubble trajectory more accurately. However, this method is computationally more expensive and two-way coupling is necessary in regions of large cavitation regions. This probably is the cause why this method did not find application in hydraulic machinery so far. The development of compressible two-fluid models that can consider the mass transfer caused by cavitation were developed by Saurel and Lematayer [139] and Habchi et al. [73, 74]. These models are able to deal with shock waves and liquid jet atomization.

For cavitation models that contain model constants, it is common practice to calibrate these constants to the application. Morgut et al. [117] calibrated the model constants for three different cavitation models for a cavitating hydrofoil by means of an optimization process. For applications on a marine propeller and a Kaplan turbine a good agreement between simulation and experiments is stated with the calibrated models [115]. Due to the calibration, the three different cavitation models lead to similar simulation results. The application of the calibrated models to a Venturi nozzle indicates the ability for qualitative analyses for steady sheet cavitation. However, deviations to measurements were observed for unsteady sheet and sheet-cloud cavitation [17]. A study on the constants of the Zwart cavitation model has been performed by Escaler et al. [58]. They varied the model constants in a range of some orders of magnitude. Furthermore, they investigated the sensitivity of the nucleation site volume fraction and the bubble radius of the nucleation site. A sensitivity regarding the inception and closure regions of inlet edge cavitation to the four parameters is stated.

Another important modeling aspect is the turbulence model. A lot of studies have been performed on the impact of the selected turbulence model on simulation accuracy for single-phase investigation in hydraulic turbines (e.g. [89, 109]). They have in

common that they highlight the importance of the turbulence model on the simulation accuracy. Turbulence plays also a major role in two-phase flows. For the flow around a twisted hydrofoil with occurring shedding cavitation, Ji et al. [87] concluded that RANS models are not able to predict the unsteady cavitation shedding.

1.2 Research Objective

The primary goal of this thesis is to examine the physical mechanism that causes the development of the full load instability by means of numerical simulations of a Francis turbine at model scale. An experimental investigation of this instability has already been performed on the same model turbine by Müller [121], who proposed a theory for the physical mechanism. However, he concluded that this theory "should be verified or disproved" [121]. The uncertainties of his theory are intended to be analyzed within this thesis.

As the full load instability occurs at cavitating conditions, the first step is identifying suitable two-phase and cavitation models. This is achieved by numerically investigating a NACA66mod hydrofoil with quasi steady sheet cavitation and a NACA0009 hydrofoil where cloud cavitation and a cavitating tip vortex occur. After selecting appropriate models for each of the test cases, these models are applied to simulations of the Francis turbine to answer the question: What causes the development of the full load instability? One aspect of interest that is analyzed is the difference of the flow field between a stable full load operating point at high pressure and the associated unstable operating point at low pressure.

Furthermore, by means of gradually decreasing the pressure in transient simulations, the development of the instability is examined in more detail. This procedure promises to give a better understanding of the ongoing physical mechanism. It further allows investigating the interaction between cavitation in the runner and draft tube, which gives the opportunity to assess the validity of the proposed physical mechanism by Müller [121]. To the best of the authors' knowledge, the procedure of investigating the full load instability by gradually decreasing the pressure level in a transient simulation has not been part of a research study so far.

Based on the findings of the physical mechanism that causes the development of the full load instability, the transferability to other operating points can be investigated.

Furthermore, new findings of this research allow for the further development of a 1D model that can be applied in future studies in this research field.

2 Fundamentals on Cavitation

For the design of hydraulic machinery, cavitation is an important phenomenon that has to be considered, as it can lead to severe damage of turbine components. Cavitation is defined as the evaporation of a liquid in regions where pressure is falling below vapor pressure and the re-condensation in regions of high pressure. Due to static and dynamic delay the onset of cavitation can be affected, which is described more detailed in literature [24, 65].

An important parameter for cavitation investigations is the cavitation number σ

$$\sigma = \frac{p_\infty - p_{vap}(T_\infty)}{\frac{1}{2}\rho_l U_\infty^2} \tag{2.1}$$

as it specifies the pressure level. There are different forms how cavitation can develop. Figure 2.1 shows the simultaneous occurrence of isolated bubbles, attached sheet cavitation and cloud cavitation on a hydrofoil.

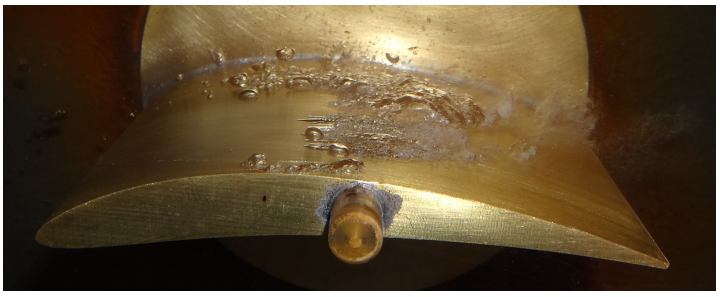

Figure 2.1: Different forms of cavitation on a hydrofoil [142].

2.1 Sheet Cavitation

The occurrence of sheet cavitation is typically accompanied by a region of flow separation. For hydrofoils, it is typically located on the suction side close to the leading edge. Which type of cavitation develops, depends on the angle of attack α and the cavitation number. While for small values of α and σ the presence of traveling bubble cavitation is probable, for increased angle of attack sheet cavitation is forming [24, 65].

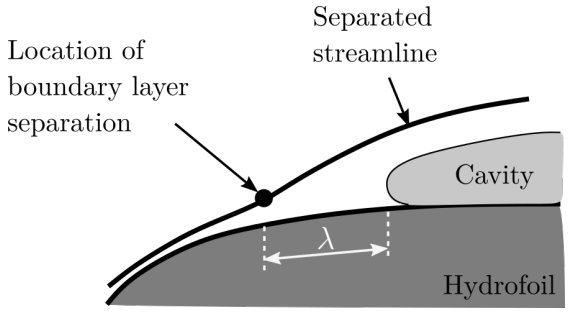

Figure 2.2: Separation region of sheet cavitation - modified from [10].

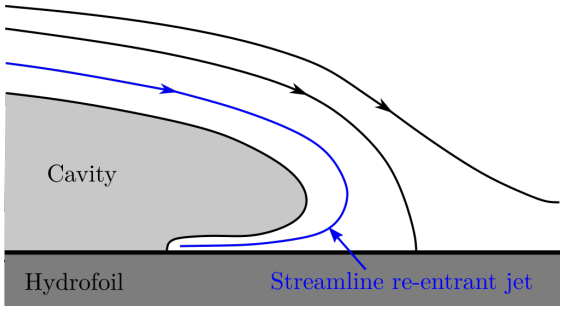

Figure 2.3: Formation of re-entrant jet - modified from [65].

The cavity forms some distance λ downstream of the location of boundary layer separation [10, 103] and acts as forward facing step to the surrounding flow (see figure 2.2). This changes the flow conditions compared to non-cavitating conditions [103].

In terms of stability, the angle of attack and cavitation number play a significant role as they affect the length and thickness of the developing cavity [101]. A stability analysis performed by Acosta [2] shows that for a hydrofoil the cavity length correlates with $\sigma/2\alpha$. In different studies (see e.g. [55, 66]), it has been confirmed that this parameter can identify the onset of instability. For sheet cavitation that is short and thin, the length is rather constant and a stable cavity develops. Under these conditions no re-entrant jet is forming [68], or it is only weekly noticeable and only few vapor structures can be observed in the wake [65].

Contrary to that, thick cavities experience the appearance of a re-entrant jet, which develops in the closure region of the cavity and moves upstream along the hydrofoil wall (see figure 2.3). The occurrence of a re-entrant jet comes across with an unstable behavior of the cavity that results in the formation of cloud cavitation. According to Franc [64], there are two conditions for the onset of cloud cavitation. On the one hand, the closure of the cavity must be in a region of high adverse pressure gradient and on the other hand, the cavity needs a relevant thickness. For a cavity thickness in the range of the re-entrant jet thickness, it comes to an interaction between the re-entrant jet and the cavity interface. This results in a cavity that consists of many small structures with a rather constant length [26]. For thick cavities, which corresponds to higher angles of attack, it comes to periodic cloud shedding as the re-entrant jet cuts of the vapor cloud regularly when it reaches the leading edge of the cavity [41]. An irregular cloud shedding can occur, for smaller angles of attack, when the cavity is not thick enough so that the re-entrant jet does not reach the leading edge of the cavity.

In hydraulic turbines, the onset of sheet cavitation at the leading edge of the runner blades is influenced by the flow incidence angle and the blade geometry while the cavitation number only plays a minor role. Consequently, it cannot be avoided at off-design conditions [14]. As the leading edge cavitation on the suction side is very aggressive when it becomes unstable, it has to be considered for erosion risk [56]. The occurrence of cloud cavitation in hydraulic machinery may be induced by the periodic flow disturbance caused by the rotor stator interaction [24].

2.2 Traveling Bubble Cavitation

Traveling bubble cavitation typically occurs for small incidence angles and cavitation numbers. One main parameter that strongly affects the range of traveling bubbles is the amount of nuclei in the flow [65]. These microbubbles serve as origin of bubble growth in regions of low pressure. The maximum bubble size strongly depends on the nuclei density as few nuclei permit the existence of big bubbles. For the presence of many microbubbles, smaller bubbles occur as neighboring bubbles limit the growth, which results in a smaller erosive potential [40].

In Francis turbines, this type of cavitation typically appears on the suction side of the runner near the trailing edge [56]. The growth of the bubbles limits the pressure drop, which results in decreased lift and for fully developed cavitation reduces efficiency of the turbine [65]. As this cavitation type strongly depends on the cavitation number, the σ-value of the plant is specified on traveling bubble cavitation [14]. For hydraulic turbines this phenomenon is most pronounced for full load conditions [106].

2.3 Vortex Cavitation

Vortices are a main issue in many practical flows. They are characterized by a pressure minimum in the vortex core. As the pressure drop due to vortices can be very strong, the inception of vortex cavitation often takes place at higher cavitation numbers compared to other cavitation types [65].

There are different types of vortex cavitation that differ in their formation. In hydraulic machinery, tip vortex cavitation can be observed in pump impellers or Kaplan turbines due to the leakage flow from pressure to suction side through the gap between shroud and runner blades. The leakage flow acts as a jet, which generates the

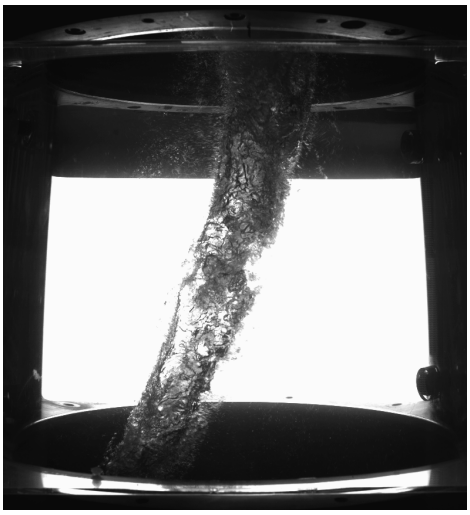

a) Vortex rope at part load.

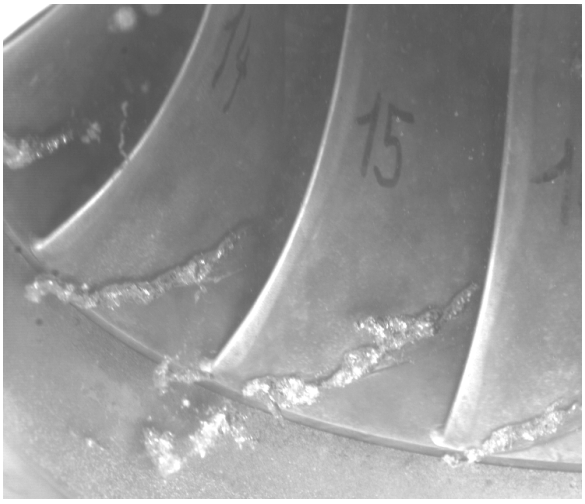

b) Inter-blade vortices at deep part load.

Figure 2.4: Vortex cavitation in a Francis turbine. Measurements performed at EPFL by A. Favrel (part load) and K. Yamamoto (deep part load).

tip vortex [120]. The minimum pressure of the tip vortex is typically at 10 - 30% of chord length, which can be found from cavitation inception [13, 65, 179]. This means that for moderate cavitation numbers the cavitating tip vortex is not connected to the leading edge. Depending on the cavitation number, the tip vortex can develop standalone or interact with other cavitation types like sheet cavitation [12].

Another important form of vortex cavitation develops due to the swirling flow in the draft tube of water turbines and is called cavitating vortex rope. The formation of the vortex rope significantly depends on the flow coefficient ϕ, while the size of the cavity volume depends on σ. At full load conditions, an axisymmetric vortex rope is forming that is counter rotating compared to the runner and for part load conditions the helically vortex rope (see figure 2.4a) is rotating in the same direction as the runner at 0.25 - 0.4 times the runner rotational frequency [14].

When the discharge is further decreased compared to part load conditions, the vortex rope in the draft tube disappears and inter-blade vortices occur in the runner channels, as displayed in figure 2.4b. At this deep part load operating point, the flow at the runner inlet is highly misaligned, which causes the generation of the inter-blade vortices as secondary flow phenomenon. This far off-design point comes across with high broadband pressure fluctuations [56].

2.4 Shear Cavitation

In hydraulic machinery, shear cavitation can occur behind the trailing edge of the runner. Due to manufacturing requirements the trailing edge is typically blunt, which results in a turbulent shear flow in the wake of the blades. There, rotational structures arise that can cavitate if the pressure in the vortex core is falling below the vapor pressure. Experimental investigations on a two-dimensional wedge showed the existence of three different vortical structures [15]. Directly behind the wedge, it comes to periodically shedding of small-scale vortices. After a transition region, the far wake begins with two-dimensional Bénard-Kármán vortices whose dynamics are strongly influenced by the occurrence of cavitation [65]. As third type, streamwise three-dimensional vortices are forming. In case of a lock-in phenomenon, this cavitation form can cause severe pressure pulsations in hydraulic machinery [56].

2.5 Full Load Surge

In hydraulic turbines, at certain full load operating conditions a self-excited surge event may occur that is characterized by strong pressure fluctuations. Several different names can be found in literature for this phenomenon, like full load surge, self-excited pressure surge or full load instability. Nowadays, theory links the occurrence of this phenomenon to variations of the swirl at the runner exit [45, 48]. According to Müller [121], full load surge is furthermore linked to an interaction between cavitation in the runner and the draft tube.

A similar phenomenon that is called cavitation surge or auto-oscillation can be found in pumps. It is characterized by periodical oscillations that are typically in the range of 0.1 - 0.4 times the runner rotational frequency [23]. Furthermore, investigations show that the frequency of the cavitation surge oscillations depends on the cavitation number [23, 158, 159].

Mass Flow Gain Factor and Cavitation Compliance

For the assessment of instabilities in hydraulic machinery, it has been shown that cavitation compliance and mass flow gain factor are key quantities (see e.g. [31, 158]). These two parameters where first introduced by Brennen and Acosta [22] for pump instabilities. Koutnik et al. [94] showed that in Francis turbines the system becomes

unstable if the ratio of mass flow gain factor and cavitation compliance exceeds the dissipation damping of the system. Consequently, mass flow gain factor has a destabilizing character, while cavitation compliance stabilizes the flow. This fact can also be found for pumps [158].

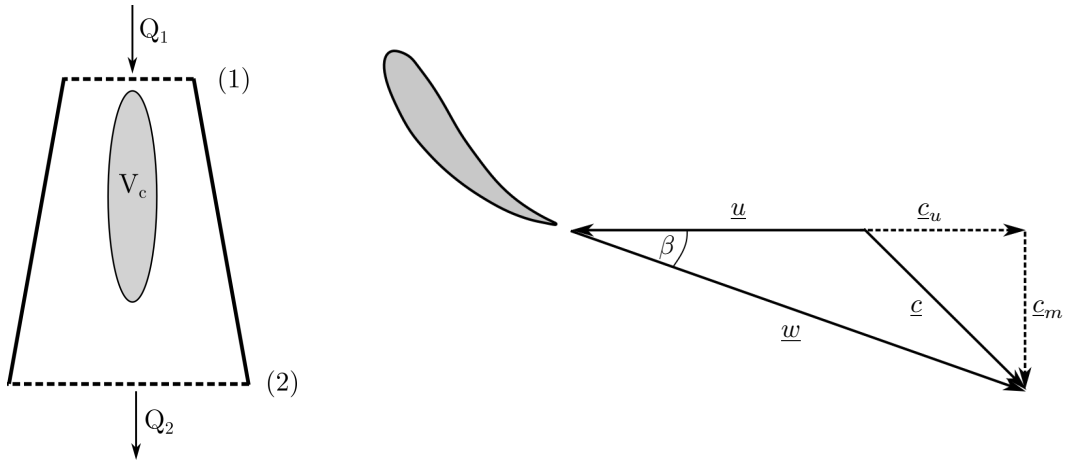

Figure 2.5: Control volume for continuity balance (left) and velocity triangle at the draft tube inlet (right).

Continuity balance for a control volume ranging from the runner outlet (1) to the outlet of the draft tube cone (2) (see figure 2.5 left) can be derived as a function of cavitation compliance and mass flow gain factor. The following derivation is based on Alligné et al. [6] with the assumption that the rotational speed is constant. For the full load surge, a fluctuating cavitation volume V_c is considered in the draft tube, which depends on the inlet swirl parameter γ and the piezometric head state variable h.

$$V_c = f(\gamma, h) \tag{2.2}$$

Consequently, the time derivative of the vapor volume can be expressed as:

$$\frac{dV_c}{dt} = \frac{\partial V_c}{\partial \gamma}\frac{d\gamma}{dt} + \frac{\partial V_c}{\partial h}\frac{dh}{dt} \tag{2.3}$$

According to Chen et al. [31], the swirl parameter is a function of the blade angle at the runner outlet β_1 and the runner exit peripheral velocity u_1 (see figure 2.5 right):

$$\gamma = \frac{c_{u1}}{c_{m1}} = cot\beta_1 - \frac{u_1 A_1}{Q_1} \tag{2.4}$$

For a turbine that runs at constant rotational speed, only the discharge Q_1 is time dependent. Hence, the time derivative of γ is:

$$\frac{d\gamma}{dt} = \frac{u_1 A_1}{Q_1^2} \frac{dQ_1}{dt} \tag{2.5}$$

The time derivative of the cavitation volume can be deduced from equations 2.3 and 2.5 with the assumption of constant rotational speed:

$$\frac{dV_c}{dt} = -\chi \frac{dQ_1}{dt} - C_c \frac{dh}{dt} \tag{2.6}$$

Therein, C_c denotes the cavitation compliance that represents how the vapor volume in the draft tube V_c changes due to variations in the pressure level:

$$C_c = -\frac{\partial V_c}{\partial h} \tag{2.7}$$

The mass flow gain factor χ is defined as the reply of the cavity volume to variations in the mass flow at the inlet Q_1 and consequently to changes of the swirl:

$$\chi = -\frac{\partial V_c}{\partial Q_1} \tag{2.8}$$

The continuity equation for the control volume from figure 2.5 for a cavitation volume of variable size yields to:

$$Q_1 - Q_2 = -\frac{dV_c}{dt} = \chi \frac{dQ_1}{dt} + C_c \frac{dh}{dt} \tag{2.9}$$

Swirl Number and Relative Flow Angle

According to Müller [121], the full load instability comes across with the occurrence of cavitation on the runner blades that is linked to a modification of relative flow angle β and swirl number S in the draft tube. The latter is defined as the ratio of axial flux of the angular momentum G_{ang} and axial flux of the axial momentum G_{ax}:

$$S = \frac{G_{ang}}{G_{ax}} = \frac{\int_0^R r^2 c_u c_m \, \mathrm{d}r}{R_{\bar{1}} \int_0^R r c_m^2 \, \mathrm{d}r} \tag{2.10}$$

Therein, $R_{\bar{1}}$ denotes the outer runner outlet radius. The relative flow angle β can be calculated with the following expression (see figure 2.5):

$$\beta = \tan^{-1}\left(\frac{c_m}{u - c_u}\right) \tag{2.11}$$

Cavitation on the runner blades affects this quantity, which is contrary to the assumption leading to equation 2.5.

Theory on Self-Oscillation

The full load instability can be assigned to a self-oscillation, that is also called self-excited or auto-oscillation. According to Jenkins self-oscillation can be defined as follows: "Self-oscillation is the generation and maintenance of a periodic motion by a source of power that lacks a corresponding periodicity: the oscillation itself controls the phase with which the power source acts on it" [85]. One famous example of an auto-oscillation is the disaster of the Tacoma Narrows Bridge [16].

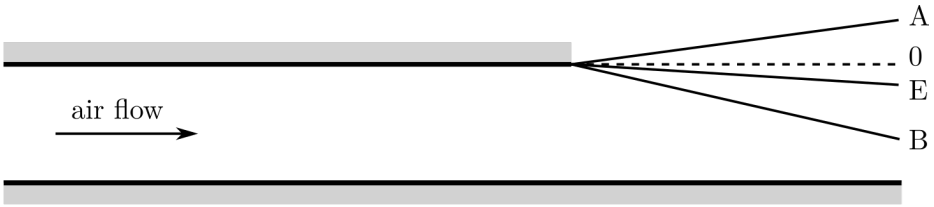

Figure 2.6: Sketch of the open tube experiment. Modified from Willis [168].

To the author's knowledge, the first publication on self-oscillation can be traced back to the 19th century. There, Willis [168] investigates the operation of the human voice. The theory of self-oscillation can be explained with his experimental setup that consists of an open tube, where one wall at the end is replaced by a flexible membrane (see figure 2.6). The tube has the form of a rectangular prism and the used medium is air. If no air flows through the tube, the membrane is oriented horizontal, which is illustrated by position 0. For a steady airflow exists an equilibrium position E that is slightly below position 0. In case that the membrane sits in position B, which is below equilibrium position, the membrane experiences a force that pushes the membrane outwards. If the membrane is in a position above equilibrium position, like position A, a force pushes the membrane inwards. Consequently, the membrane may come into an oscillation about equilibrium position E when the airflow is turned on.

Typically, an oscillation around the equilibrium position should be damped out by friction and the resistance of air. However, for a self-oscillation this is not the case and a permanent oscillation persists. Both, Willis [168] and Airy [3] explained this with the fact that the restorative force acts time-delayed. Airy proposed to model the self-oscillation as a harmonic oscillator:

$$\ddot{q} = -a \cdot q(t) - b \cdot q(t - c) \tag{2.12}$$

Therein, the last term on the right side takes into account that the restoring force depends in parts on the deflection q at an earlier time. By the use of first-order perturbation theory, Airy demonstrated that the amplitude of the oscillation grows if $0 < b \ll a$ and $0 < c\sqrt{a} < \pi$. According to Jenkins [85], for $b = 0$ the oscillator would always be pushed back to its equilibrium position, but for the limits from Airy the delayed restoring force does for some time not reverse its sign when the oscillator passes the position of zero deflection ($q = 0$). This causes the oscillator to be pushed away from equilibrium position. It results in a positive feedback, as with increasing amplitude this pushing grows. Regarding the full load instability the importance of a time delay has been pointed out by Dörfler et al. [45]. They explained this dead time physically to be the time that the local swirl needs to travel from the outlet of the runner to the relevant position in the draft tube cone.

In case that $0 < c\sqrt{a} \ll 1$ equation 2.12 can be transformed into an equation for a negatively damped linear oscillation, with the help of a Taylor expansion:

$$\ddot{q} - \gamma\dot{q} + \omega^2 q = 0 \tag{2.13}$$

Therein, γ and ω^2 are defined as follows:

$$\begin{aligned} \gamma &= bc \\ \omega^2 &= a + b \end{aligned} \tag{2.14}$$

For a negatively damped oscillation, one component of the force is in phase with the velocity $\dot{q}$. This introduces energy into the system and as a consequence leads to an exponentially growing oscillation. At some point nonlinear effects get important, which limits the amplitude and results in a regular self-oscillation.

2.6 Cavitation Noise

Tremendous noise production can be observed when vapor bubbles collapse. These bubbles do even emit a sound wave, when they change their volume, which might be caused by an external pressure variation or by some instability of the cavity itself [50]. The radiated acoustic pressure p_a, that is caused by the volume change of the cavity, is proportional to the second time derivative of the vapor volume which stands for the volumetric acceleration forced upon the flow:

$$p_a \sim \frac{d^2 V_c}{dt^2} \tag{2.15}$$

This correlation has been derived in several different ways in literature (e.g. [18, 24, 50]) and is valid in a sufficiently large distance from the cavity [62]. It has to be emphasized that equation 2.15 is independent of the bubble shape, which means that the change of bubble shape, for instance due to impingement on a rigid surface, without any volume pulsation does not result in sound [153, 154]. In the far field, the cavity can be considered as a simple source [24], so that several bubbles can be treated as one collective. The maximum emission of sound can be observed when the cavity is close to its minimum size [23]. Furthermore, the radiated acoustic pressure increases with increasing cavity size that collapses [18]. The connection between radiated acoustic pressure and second time derivative of the vapor volume has been experimentally confirmed for surge instability on a cavitating propeller [55].

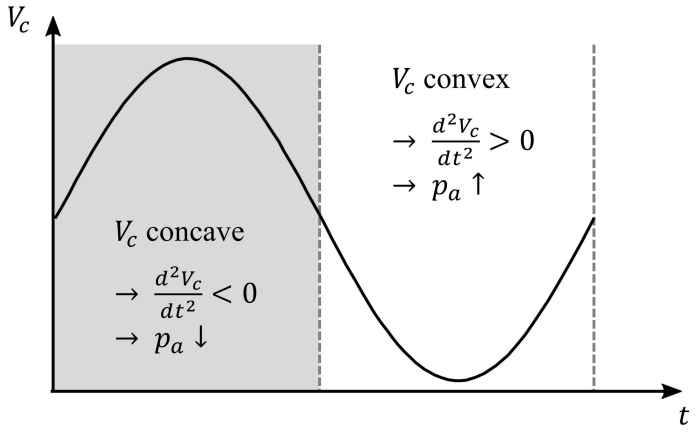

Figure 2.7: Visualization of the correlation between radiated acoustic pressure and second time derivative of the vapor volume.

In figure 2.7 the correlation between radiated acoustic pressure and second time derivative of the vapor volume from equation 2.15 is illustrated. The acceleration of cav-

itation volume that causes the pressure radiation is equivalent to the curvature of temporal course of cavitation volume. When the cavitation volume is shaped concave a smaller pressure can be expected compared to the case when cavitation volume is shaped convex.

3 Fundamentals on Computational Fluid Dynamics

For the numerical simulation of cavitating flows, a suitable setup is necessary to correctly reproduce the existing flow phenomena. The selection of the two-phase modeling approach as well as the cavitation model plays a major role. Furthermore, the appropriate choice of turbulence model is important. This chapter is intended to provide the relevant basics for CFD of cavitating flows.

3.1 Modeling of Two-Phase Flows

For two-phase flows, the selection of a suitable multiphase modeling approach is of main importance as it can significantly affect the accuracy of the simulation results and has a big influence on the computational effort. The suitability of the different models strongly depends on the multiphase flow regime [9, 80, 177]. The main different flow regimes can be classified in dispersed flows, mixed or transitional flows and separated flows [80, 177]. While dispersed flows are characterized by the presence of small bubbles, droplets or particles in a continuous phase, separated flows consist of different fluids with a distinct interface. Cavitating flows are typically dispersed flows, for example in cavitation clouds, or transitional flows, when huge cavitation regions are forming.

Typically, the simulation methods for multiphase flows can be divided into the approaches Euler-Lagrange and Euler-Euler. The Euler-Lagrange method consists of one continuous phase treated in the Eulerian framework (control volume is fixed) and the Lagrangian tracking of single particles or bubbles. This method is limited to dispersed flows. The Euler-Euler approach treats the different phases as interpenetrating continua. It can be subdivided into different models. The most complex approach is the inhomogeneous model as every phase has its own velocity field. A more simplified method is the mixture model, where the different phases are treated as a single fluid with variable properties. It enables the phases to have different velocities as some slip

between the phases is allowed [177]. If, as further simplification, it is assumed that the different phases share a common velocity field, the homogeneous model is derived.

3.1.1 Inhomogeneous Model

The inhomogeneous model, also called two-fluid model, is the most general approach of the Euler-Euler models. It allows having separate velocity fields for every phase. Similar to single-phase modeling, the governing equations can be derived from balance of mass, momentum and energy on an infinitesimal control volume. Nevertheless, the presence of a second phase results in a more complex modeling, as the interaction between the phases has to be considered. For most practical purposes, it is not possible and necessary to resolve all microscopic motions and it is thus common practice to apply some averaging process in the derivation of the governing equations [177]. The derivation of the governing equations of the inhomogeneous model can be found in literature (e.g. [51, 79, 84, 177]). The resulting equation for the conservation of mass is:

$$\frac{\partial\left(\alpha^k\rho^k\right)}{\partial t}+\frac{\partial\left(\alpha^k\rho^k U_j^k\right)}{\partial x_j}=\Gamma^k \tag{3.1}$$

Therein, the superscript k denotes the phase. For cavitating flows, this results in two equations, one for the liquid phase l and one for the vapor phase v. The concept of phasic volume fraction ensures that the volume occupied with one phase cannot be filled with the other phase [9]. Consequently, the sum of volume fractions α^k is equal to one:

$$\sum_{k=1}^{2}\alpha^k=1 \tag{3.2}$$

Γ represents the interfacial mass source, which needs to be modeled with a cavitation model and has to fulfill the following constraint:

$$\sum_{k=1}^{2}\Gamma^k=\Gamma^l+\Gamma^v=0 \tag{3.3}$$

All in all, equation 3.1 is similar to mass conservation for single-phase flows, with the two differences that the volume fraction α is introduced by the averaging and that the interfacial mass source Γ accounts for mass transfer between the phases.

The derivation of the momentum balance is based on Newton's second law of motion, which states that the growth rate of momentum of the fluid element is the sum of the forces that act on the fluid element. After the averaging process the governing equations for the conservation of momentum are:

$$\begin{aligned} &\frac{\partial\left(\alpha^k\rho^k U_i^k\right)}{\partial t}+\frac{\partial\left(\alpha^k\rho^k U_i^k U_j^k\right)}{\partial x_j}=-\alpha^k\frac{\partial p}{\partial x_i} \\ &+\frac{\partial}{\partial x_j}\left(\alpha^k\left(\mu^k+\mu_t^k\right)\frac{\partial U_i^k}{\partial x_j}\right)+\alpha^k\rho^k g_i+S_i^{int} \end{aligned} \tag{3.4}$$

It has to be mentioned that this equation already contains the assumption that the applied turbulence model is based on the eddy viscosity hypothesis. Furthermore, both phases share the same pressure field. This assumption is common practice in Euler-Euler models (see e.g. [9, 27, 80, 177]). The presence of two phases results in interfacial source terms S^{int}. They take into account interfacial momentum transfer that is caused due to the interaction of the phases and interfacial mass transfer. As the separate phases have their own solution field, the liquid and vapor phase can have different velocity fields that tend to come to equilibrium due to interphase drag [7].

Interfacial Forces

The modeling of the interfacial momentum transfer is of main importance for the inhomogeneous model. For the subsequent descriptions the interaction between a vapor bubble or particle and the surrounding liquid is described[1]. The interfacial momentum transfer can be computed with a linear combination of the interfacial forces acting on the bubble because of the interaction with the liquid phase [27, 80]: Typically, drag, lift, turbulent dispersion and virtual mass force are considered. Other forces like the wall lubrication force and the Basset force are neglected as they are less important [27].

For most practical multiphase flow applications, the drag force is of main importance [177]. It is caused due to the relative motion U_{rel} between the bubble and the surrounding fluid and is defined as follows:

$$F_D=\frac{\pi}{8}C_D\rho^l d_b^2 U_{rel}|U_{rel}| \tag{3.5}$$

[1]For better readability the following descriptions are made for a bubble. However, they are also valid for particles.

Therein, d_b represents the diameter of the bubble. Different models are applicable for the selection of the drag coefficient C_D. From solid particle theory, a constant drag coefficent

$$C_D = 0.44 \tag{3.6}$$

can be selected for sufficiently large particle Reynolds numbers Re_p from 1000 to 200,000 [141]. The Schiller Naumann drag model [140] also takes into account the transitional regime for particle Reynolds numbers between 0.1 and 1000:

$$C_D = max\left(\frac{24}{Re_p}\left(1 + 0.15Re_p^{0.687}\right), 0.44\right) \tag{3.7}$$

For sufficiently small particle Reynolds numbers, bubbles behave like solid spherical particles. This normally is the case for small bubble diameters up to approximately one millimeter [80]. Thus, the Schiller Naumann drag model is well suited in this regime. At higher particle Reynolds numbers, the bubbles change their shape and consequently the drag coefficient differs from solid spherical particles. In this case other models like the Ishii-Zuber model [81] have to be applied.

The lift force is caused by a shear flow, which is typically present close to a wall. It acts perpendicular to the bubble motion. However, the direction depends on the bubble size. While small spherical bubbles are pushed to the wall, big deformed bubbles move to the center [136]. For spherical fluid particles, the Legendre and Magnaudet lift force model [102] is applicable. For further information regarding the lift force it is referred to literature (e.g. [39, 151, 156, 180]).

The physical cause of the turbulent dispersion force is the interaction of single bubbles with the turbulent eddies of the continuous phase. This force has the effect that bubbles move from regions of high to low concentration. More detailed information about the modeling of the turbulent dispersion force can for instance be found in [80, 145, 176].

The virtual mass force can be explained by the fact that the acceleration of a bubble causes a force to move the fluid around the bubble. Detailed information about the modeling can be found in literature (e.g. [39, 80, 180]).

In the scope of this work, the conservation of energy is not discussed in detail, as the phases are considered incompressible and no heat transfer is considered. The incompressible treatment can be justified with the low Mach number flow [177]. Even

though the speed of sound in water reduces due to the presence of a vapor phase, it is still significantly larger compared to transport velocity of the flow. For further information on the conservation of energy for multiphase flows it has to be referred to literature (e.g. [51, 80, 177]).

Treatment of the Vapor Phase

For the inhomogeneous model three different treatments of the vapor phase are possible: continuous, monodisperse and polydisperse. When a huge connected cavitation volume forms, like stable sheet cavitation at the leading edge of a hydrofoil, this phase can be handled continuous. On the other hand, cavitation often occurs in the form of single bubbles, for instance in cloud cavitation. Then, a dispersed treatment of the vapor phase should be selected. If the bubbles have a similar size they can be handled monodisperse. As criterion whether the bubbles are close to a single size, the standard deviation of the mean bubble diameter should be less than ten percent [39]. For a wider range of bubble sizes, a polydisperse treatment is advisable, which requires additional modeling with a population balance approach. It considers on the one hand that a wide range of different bubble sizes exists, which is relevant as the size has a significant impact on the flow behavior. On the other hand, a population balance approach takes into account coalescence and breakup of bubbles and hence is able to resolve changes in the bubble size distribution.

In the scope of this work, the multiple size group (MUSIG) model is applied, which is a class method approach. The basic idea behind the MUSIG model is to discretize the particle size distribution into a discrete number of size fractions. Changes in the particle size distribution caused by coalescence and breakup are considered by interfraction mass transfer to balance mass conservation [80]. For the simpler homogeneous MUSIG model, all bubbles move with one common gas velocity, while the inhomogeneous MUSIG model, firstly introduced by Shi et al. [146] takes into account different velocity classes. The application of the inhomogeneous MUSIG model is necessary when the radial separation of small and large bubbles is relevant, while otherwise the homogeneous MUSIG model is sufficient [96]. To account for the interaction of bubbles, models for coalescence and breakup have to be applied. For the simulations with the MUSIG model, the breakup model of Luo and Svendsen [105] and the coalescence model of Prince and Blanch [133] are used. There is a variety of other population balance approaches available that are not applied within this study. For further information it is referred to literature (e.g. [33, 80, 114]).

3.1.2 Homogeneous Model

The application of the inhomogeneous model is quite complex and simulations are time consuming. Thus, simplified two-phase modeling approaches may be more feasible for certain types of flows. The homogeneous model can be derived from the two-fluid model with the assumption that the relative motion between the phases can be neglected [92]. This corresponds to equilibrium between the phases that is caused by a large interface transfer rate [7] when the two phases are strongly coupled [80]. As a consequence, the two-phase system can be handled as one mixture m. This results in the fact that the computational effort is significantly decreased compared to the inhomogeneous model, as only one set of equations needs to be solved for the mixture. For the homogeneous model, the continuity equation is

$$\frac{\partial \rho^m}{\partial t} + \frac{\partial \left(\rho^m U_j^m\right)}{\partial x_j} = 0 \tag{3.8}$$

and the momentum equations are:

$$\frac{\partial \left(\rho^m U_i^m\right)}{\partial t} + \frac{\partial \left(\rho^m U_i^m U_j^m\right)}{\partial x_j} = -\frac{\partial p}{\partial x_i} + \frac{\partial}{\partial x_j}\left(\left(\mu^m + \mu_t^m\right)\frac{\partial U_i^m}{\partial x_j}\right) + \rho^m g_i \tag{3.9}$$

Furthermore, a transport equation for the volume fraction α needs to be solved. This equation takes into account transport of the different phases as well as the mass transfer caused by cavitation.

$$\frac{\partial \rho^l \alpha^l}{\partial t} + \frac{\partial \left(\rho^l U_j^m \alpha^l\right)}{\partial x_j} = \Gamma^l \tag{3.10}$$

Equation 3.2 and 3.3 are also valid for the homogeneous model. For problems where the total behavior of the two-phase mixture, rather than the local flow of each phase, is of main interest, the homogeneous model can be effective in many cases [19, 80].

3.1.3 Volume of Fluid Method

The Volume of fluid (VoF) method is a widely used approach for two-phase modeling and can be considered as related to the homogeneous model. However, the homogeneous model can be applied to flows with interpenetrating fluids - e.g. dispersed phase in a continuous phase - while for the VoF method the fluids are typically separated

and the interface is tracked. Thus, the VoF method becomes of interest when there is a distinct separation between the different phases like for stratified or slug flows [9]. As in Francis turbines cloud cavitation might be present on the runner blades, which does not fulfill the criterion that the fluids do not interpenetrate, the VoF method is not further considered in the scope of this study.

3.1.4 Two-Phase Model Selection

As already highlighted in the model descriptions, the appropriate selection of the two-phase modeling approach depends on the flow conditions. The dimensionless Stokes number is a good measure for the flow behavior of a bubble in a moving liquid [9]:

$$St = \frac{\tau_V}{\tau_F} = \frac{\frac{\rho_v d_b^2}{18\mu_l}}{\tau_F} \tag{3.11}$$

Therein, τ_V denotes the momentum response time, which is a function of density of the vapor phase ρ_v, bubble diameter d_b and dynamic viscosity of the liquid phase μ_l. The characteristic time scale of the flow field τ_F can be approximated by the ratio of a characteristic length and velocity scale.

The Stokes number determines the kinetic equilibrium of the bubbles with the surrounding liquid. In the easiest case ($St \ll 1$) the bubbles can be considered to be in velocity equilibrium with the surrounding liquid. Thus, the bubbles have enough time to adapt to changes in the flow field. Consequently, the problem can be seen one-way coupled and the homogeneous model should be applied as it is less expensive. On the other hand, for large Stokes numbers ($St \gg 1$) the bubbles have a slow response to changes in the surrounding liquid. As a result, velocity equilibrium does not occur and the inhomogeneous model is advisable for this two-way coupled problem. [39, 177]

Brennen [25] describes a different concept for the selection of the two-phase modeling approach. Nevertheless, this concept is similar as it is also based on the ratio of momentum response time and flow field time scale. Thus, it is not described in more detail.

3.1.5 Cavitation Model

Mass transfer between two phases needs to be considered by a cavitation model. The mass transfer is considered in the governing equations by the interfacial mass source

Γ (see equations 3.1 and 3.10). In the scope of this study, the Zwart model [183] is applied. It is based on a simplified Rayleigh-Plesset equation and distinguishes between evaporation and condensation process that are treated differently:

$$\begin{aligned} \Gamma^l &= -F_e \frac{3\alpha_{nuc}(1-\alpha_v)\rho_v}{R_{nuc}} \sqrt{\frac{2}{3}\frac{p_{vap}-p}{\rho_l}} \quad if \;\; p < p_{vap} \\ \Gamma^l &= F_c \frac{3\alpha_v \rho_v}{R_{nuc}} \sqrt{\frac{2}{3}\frac{p-p_{vap}}{\rho_l}} \quad if \;\; p > p_{vap} \end{aligned} \tag{3.12}$$

Both processes have in common that they are driven by the difference between static pressure p and vapor pressure p_{vap}. Condensation takes place when pressure exceeds vapor pressure, while evaporation happens when pressure is falling below vapor pressure. The Zwart model contains the radius R_{nuc} and volume fraction α_{nuc} of the nucleation site, which are model constants. Furthermore, F_e and F_c denote the empirical calibration coefficients for evaporation and condensation process. In the scope of this study, two different sets of model constants are applied. On the one hand, the recommended model parameters by Zwart et al. [183] are used. On the other hand, Morgut et al. [116, 117] determined F_e and F_c by calibrating these coefficients for the flow around a NACA66mod hydrofoil. The constants for both parameter sets are listed in table 3.1.

Table 3.1: Cavitation model constants.

	F_e	F_c	$R_{nuc}\,[\mu m]$	α_{nuc}
Zwart [183]	50	0.01	1.0	0.0005
Morgut [117]	300	0.03	1.0	0.0005

A variety of other cavitation models are available in literature. Models that are also often used are for instance the Kunz model [98], the Full Cavitation Model [147] or the Schnerr and Sauer model [143]. However, simulation results by Morgut et al. [116, 117] indicate that no significant differences can be noticed for different cavitation models with calibrated cavitation constants. Thus, in this work, only the Zwart model is applied.

The huge density difference between liquid and vapor phase of water can lead to stability issues in the numerical treatment. For that reason in ANSYS CFX a maximum density ratio is implemented into the transport equation of the volume fraction that by default is set to 1,000 [7]. The impact of maximum density ratio has been stud-

ied in different publications [86, 181]. Both studies conclude that a higher maximum density ratio leads to a larger cavitation volume and can result in a better agreement to measurements. However, it has to be evaluated whether numerical stability issues arise.

3.2 Turbulence Modeling

For numerical simulations of hydraulic machines, turbulence modeling is an important aspect. As a Direct Numerical Simulation (DNS) for this high Reynolds number application is nowadays impossible [11], Reynolds-Averaged-Navier-Stokes (RANS) models and Large-Eddy-Simulation (LES) can be considered to account for capturing effects caused by turbulence.

3.2.1 RANS

The idea behind the RANS approach is that for many engineering applications averaged values (e.g. of velocity or pressure) are of main interest. Consequently, an instantaneous quantity ϕ is described by its time-mean value $\bar{\phi}$ and the fluctuation ϕ':

$$\phi = \bar{\phi} + \phi' \tag{3.13}$$

Applying this relation to the Navier-Stokes-Equations and performing a time average, results in the RANS formulation. The averaging process introduces Reynolds stresses. To close the system of equations a turbulence model has to be applied. Typically, either eddy-viscosity models (EVMs) or Reynolds stress models (RSMs) are used. For a more detailed review of the different models it is referred to literature (see e.g. [11]).

In the scope of this study, the Shear-Stress-Transport (SST) model by Menter [111] is applied, which is assigned to EVMs. It is a state-of-the-art two-equation model that is validated against many practical applications like for example turbomachines [11]. However, EVMs are based on the assumption of homogeneous turbulence, which comes across with the fact that they cannot capture effects like system rotation and streamline curvature [148]. As RSMs are less robust and computationally more expensive Spalart and Shur [150] developed an approach to overcome this weakness of EVMs. An adaption to the SST model - in the following called curvature correction - has been performed by Smirnov and Menter [148] that shows promising results.

Wall functions are often used in CFD simulations to reduce grid size and consequently decrease the computational effort. In terms of wall functions, the dimensionless wall distance y^+ plays a major role. It is defined by the friction velocity u_τ, the distance to the nearest wall y and the local kinematic viscosity ν:

$$y^+ = \frac{u_\tau y}{\nu} \tag{3.14}$$

If no wall functions are used, the boundary layer resolution should be down to $y^+ \approx 1$. This allows to properly resolve the viscous sublayer. The theory of wall functions is based on the existence of a region in wall proximity where the boundary profile in wall normal direction follows a logarithmic law [61]. With no further treatment wall functions should only be applied to $y^+ > 30$ [61]. However, as this criterion cannot be fulfilled in complex flows that can face detachment, further developments of wall functions have been made like the automatic wall treatment proposed by Menter and Esch [110]. The automatic wall treatment blends between wall resolved regions and regions of the logarithmic law.

3.2.2 LES

LES is an approach that is between RANS and DNS for both, accuracy and computation cost. In LES simulations, the large scales are fully resolved, while the small scales are modelled. The separation of resolved large eddies and small sub-grid scales is obtained by spatially filtering the Navier-Stokes equations. The use of LES is getting more and more popular. However, due to the significant higher computational effort of LES, in industry applications RANS is nowadays still applied in most cases. For hydraulic turbine simulations, a wall-resolved LES is still at the limits of feasibility. Krappel et al. [95] applied meshes up to 300 million elements that still did not completely fulfill the requirements of wall layer resolution ($y^+ < 1$, $\Delta x^+ \approx 50 - 150$ and $\Delta z^+ \approx 15 - 40$) [130].

3.2.3 Scale Resolving Simulation

As simulations based on RANS turbulence models cannot capture certain flow features and LES is nowadays not completely feasible, hybrid RANS-LES modeling concepts have been developed. These so called scale resolving simulation (SRS) approaches can at least resolve a part of the turbulence spectrum [112]. The motivation of SRS

models is on the one hand an increased accuracy compared to RANS models and on the other hand their ability to resolve flow features that cannot be captured with RANS simulations, which is important for instance for vortex cavitation [112]. In the scope of this work, the Stress-Blended Eddy Simulation (SBES) model [113] is applied that uses the RANS model in the boundary layers and resolves the large eddies away from the wall [112].

The idea behind the SBES model is to blend between RANS and LES models by a shielding function f_s. This shielding is carried with the stresses. In the event that both models are EVMs the blending can be directly performed for the eddy viscosity μ_t:

$$\mu_t = \mu_t^{RANS} f_s + \mu_t^{LES} (1 - f_s) \tag{3.15}$$

For the applications in this work, the SST and WALE model are selected as RANS or LES model respectively. [113]

3.2.4 Turbulence in Two-Phase Flows

For numerical simulation of two-phase flows, turbulence modeling is still of main importance and is even more complicated compared to single-phase flows. The reason is that it comes to interaction of the different phases, which leads to a modified turbulence behavior [25]. Particles that are small compared to the most energetic eddy do absorb energy from eddies which results in a reduction of turbulent energy [69]. On the other hand, large particles are not following the turbulent fluid motion which causes wakes that add turbulent energy. These explanations indicate that the turbulence behavior is significantly affected by the Stokes number.

The following statements on turbulence modeling are all made for EVMs, as all the applied models are based on this concept. This comes across with the assumption that the eddy viscosity hypothesis is also valid for each phase in multiphase flows [8]. First of all, turbulence modeling in multiphase flows depends on whether the homogeneous or inhomogeneous model is applied. For the homogeneous model, the mixture is treated as one fluid and thus a single turbulence field is solved for the mixture [7]. Consequently, for this approach the turbulence modeling is equivalent to single-phase simulations.

For the inhomogeneous model, the turbulence modeling becomes more complex. One widely used approach is to apply standard turbulence models like the k-ϵ model and

add specific production and dissipation terms [70, 149]. Another common approach that is used within this work is to compute the turbulent viscosity of the continuous phase (c) as the sum of a shear induced and a particle induced component:

$$\mu_{t,c} = \mu_{t,s} + \mu_{t,p} \tag{3.16}$$

The particle induced eddy viscosity can for example be modeled with the Sato model [138].

To save computational time by reducing the number of transport equations that need to be solved, it is common practice to use a simpler approach for the turbulence modeling of a dispersed phase [177]. In the Dispersed Phase Zero Equation Model, the turbulent viscosity of the dispersed phase is derived from the continuous phase in the following way:

$$\mu_{t,d} = \frac{\mu_{t,c}}{\sigma_P} \frac{\rho_d}{\rho_c} \tag{3.17}$$

The Prandtl number σ_P is often set to one, which is applicable when the particle relaxation time is short compared to time scales of turbulence dissipation [8, 177]. For more detailed explanations on turbulence modeling in multiphase flows it has to be referred to literature (e.g. [114, 177]).

4 Investigation of Different Test Cases

The simulation of two-phase flows with phase change is a challenging task. Suitable modeling approaches are necessary to correctly predict the existing flow conditions. For the selection of appropriate models for the Francis turbine simulations, test cases on two different hydrofoils are investigated in this chapter. The focus lies on the discussion how different models and model parameters affect the accuracy of the simulation result.

4.1 NACA66mod

First, the cavitating flow around a NACA66mod hydrofoil is investigated. This test case is characterized by a quasi-steady sheet cavity that develops close to the leading edge of the suction side. The measurements were performed in the high-speed water tunnel at the California Institute of Technology [90] by Shen and Dimotakis [144].

4.1.1 Setup

Contrary to the numerical investigations of Morgut et al. [117], this test case is investigated three-dimensional (3D). In spanwise direction the cavitation tunnel has a width of 0.152 m. The length of the simulation domain is 9 times the chord length of the hydrofoil, with the hydrofoil being located approximately 3 chords downstream of the inlet boundary condition (see figure 4.1). This is in good agreement to the simulation domain used by Morgut et al. [117].

All simulations are performed steady state with an inlet velocity $U_\infty = 12.2\,\mathrm{m/s}$. At the outlet, the static pressure p_{ref} is prescribed to set a cavitation number $\sigma = 1.0$ according to the definition of equation 2.1. The incidence angle of the hydrofoil is 4°. The SST model is applied for turbulence and at the inlet a turbulence intensity of 5% and a turbulent length scale that corresponds to 5% of the chord length are assumed. For spatial discretization the high resolution scheme is used.

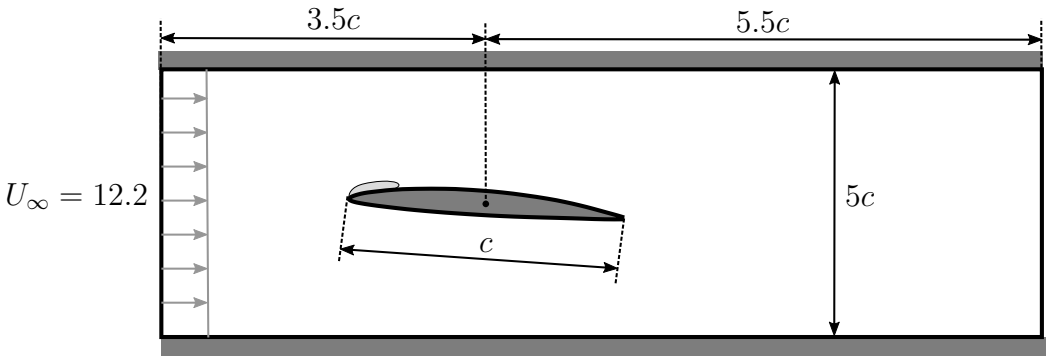

Figure 4.1: Sketch of the simulation domain of the NACA66mod case (not drawn in scale).

A mesh independence study has been performed with single-phase simulations in a preliminary study. The final mesh has a total number of approximately 1.6 million hexahedrons and an averaged y^+-value of 34. The results of the mesh independence study are in good agreement with the 2D results of Morgut et al. [117] and are thus not presented more detailed.

4.1.2 Numerical Investigations

For the NACA66mod hydrofoil homogeneous and inhomogeneous two-phase modeling approaches are applied including variations of model parameters. The results are compared to experimental results to select suitable models with respect to accuracy and computational effort. Measurements are available for negative pressure coefficient $-c_p$ at different locations along the suction side of the hydrofoil, which is defined as follows:

$$-c_p = \frac{p_{ref} - p}{0.5\rho_l U_\infty^2} \tag{4.1}$$

For validation of the computational setup serves a simulation at non-cavitating conditions. The course of negative pressure coefficient along the suction side of the hydrofoil is displayed on the left side of figure 4.2. A good agreement between simulation and measurement can be stated. Consequently, the described setup is applied for further investigations at cavitating conditions.

Homogeneous Model

As initial simulation (iniHomog) serves the setup using the homogeneous model, the cavitation model constants from Zwart et al. [183] and a maximum density ratio of 1000. Compared to this simulation, the cavitation model constants are changed to the recommended constants from Morgut et al. [117] in setup CcCvMorgut (see also table 3.1). The second variation - called MDR20000 - uses the Zwart constants but a maximum density ratio of 20000 as proposed by Zhang et al. [181].

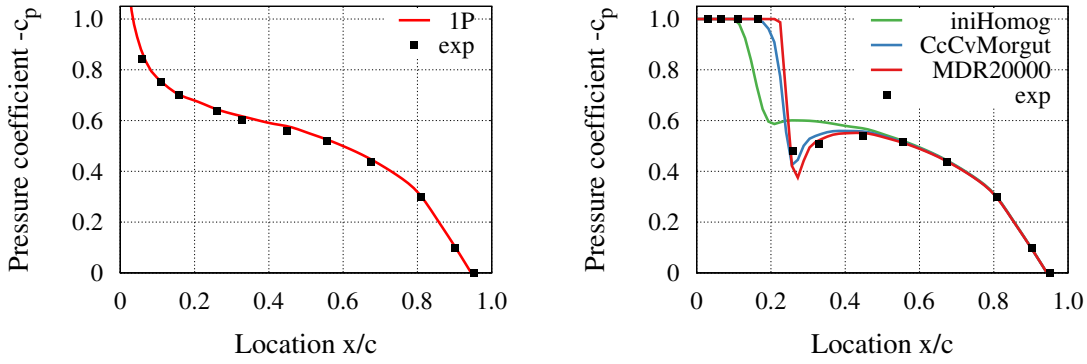

Figure 4.2: Pressure coefficient distribution at the suction side wall of the NACA66mod hydrofoil. Left: Non-cavitating conditions. Right: Cavitating conditions. For simulations the homogeneous model is used with different two-phase parameters.

A comparison of the wall pressure distribution at the suction side of the hydrofoil is displayed on the right side of figure 4.2. The cavity closure is located in the region where $-c_p$ drops from 1 to smaller values in the experimental data. It can be observed that the initial simulation underestimates the length of the cavitation region. On the other hand, the simulations with adjusted cavitation model constants and maximum density ratio are in better agreement with the measurement concerning the cavity closure region. This indicates that both parameters can have a relevant impact on simulation accuracy. The setup CcCvMorgut seems to still slightly underestimate the cavity length, which is contrary to the results from Morgut et al. [117]. This can be explained by the fact that in this study the test case is investigated 3D, which results in different losses in the cavitation tunnel and consequently differences in pressure level and cavitation volume. Nevertheless, the calibrated constants for the 2D simulations lead also to a significant improvement for the 3D results.

The visualization of the vapor volume fraction at the leading edge of the hydrofoil is shown in figure 4.3. It can be observed that for the setups CcCvMorgut and

MDR20000 a significantly more pronounced cavitation region is forming, which could already be expected from the c_p distribution. Both measures - changing the cavitation model constants and increasing the maximum density ratio - result in an increased cavity volume. Especially for setup CcCvMorgut, the development of a re-entrant jet in the cavity closure region can be observed that, however, is weak enough that the sheet cavity remains stable.

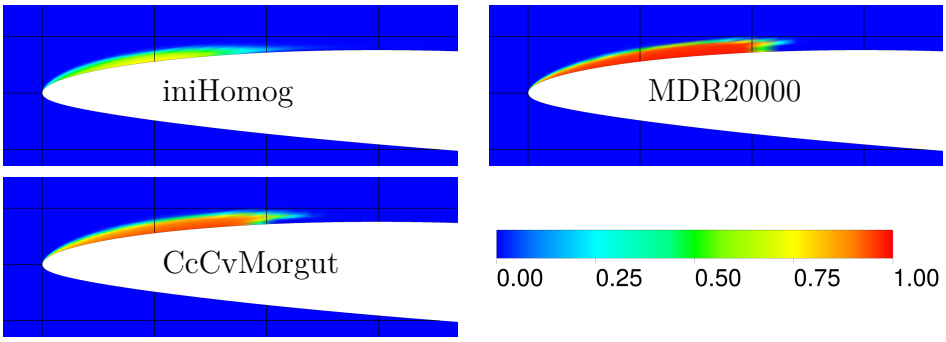

Figure 4.3: Visualization of the cavitation volume on the suction side of the NACA66mod hydrofoil. Shown is the vapor volume fraction for different simulation results with the homogeneous model.

Inhomogeneous Model

The reference setup for the simulations with the inhomogeneous model treats the vapor phase as dispersed fluid with a characteristic diameter of 1 mm for the dispersed phase. Furthermore, a constant drag coefficient $C_D = 0.44$ is set and all other interfacial forces are neglected. The impact of different two-phase parameters is investigated by changing one of the parameters per setup. For all simulations, the constants of the cavitation model and the maximum density ratio are set just like for setup iniHomog.

First, the impact of the diameter of the dispersed phase is investigated. Simulations are performed with four different diameters: 1 µm, 10 µm, 0.1 mm and 1 mm. The values are selected based on investigations by Maeda et al. [107] who showed that the bubble radius in a cavitation cloud ranges from some micro meters up to approximately 0.1 mm. Furthermore, the upper limit of 1 mm is chosen as on the one hand cavitation bubbles can reach this size and on the other hand a further increased bubble diameter led to divergence of the simulation. The differences between the different dispersed phase diameters for the distribution of $-c_p$ are presented in figure 4.4. With decreasing diameter the pressure rise in the cavity closure region moves closer to the leading edge. For the smallest diameter, the simulation results with the inhomogeneous model are

similar to the results with the homogeneous model (iniHomog). The reason is that with decreasing diameter of the dispersed phase the drag force is reduced (see equation 3.5), which results in negligible relative motion between liquid and vapor phase. Compared to the measurement the selection of dispersed phase diameter 1 mm gives the best agreement.

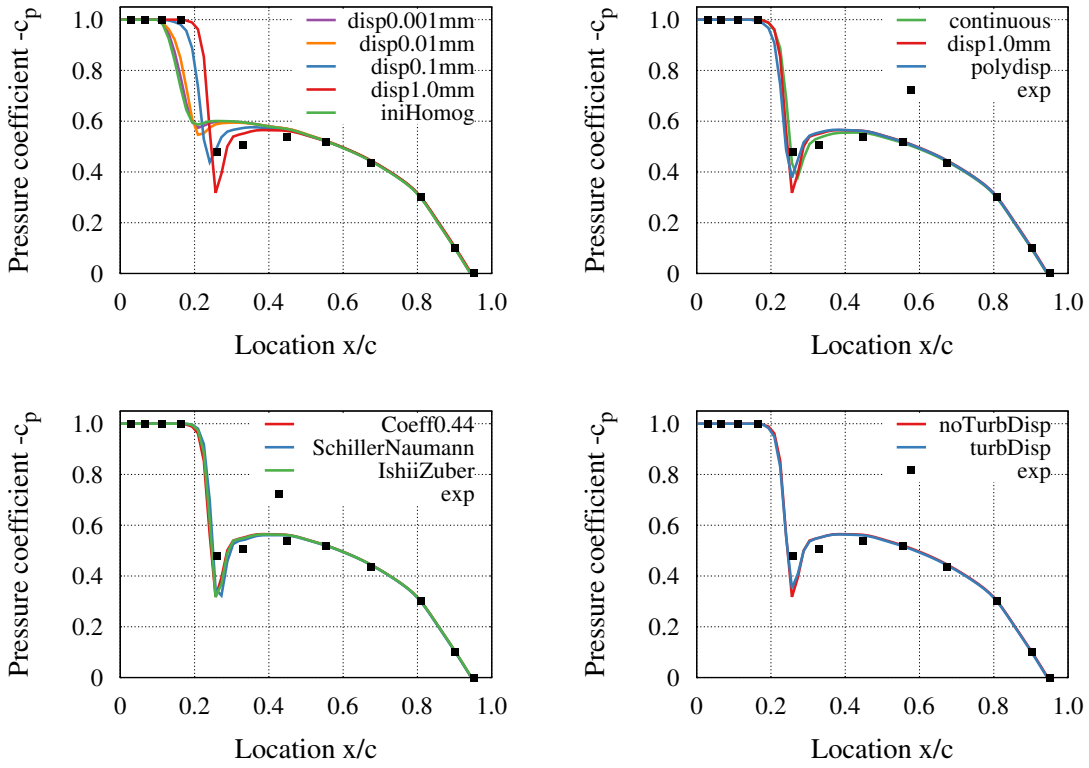

Figure 4.4: Pressure coefficient distribution at the suction side wall of the NACA66mod hydrofoil using the inhomogeneous model with different two-phase parameters.

In figure 4.5, the cavitation volume that is forming at the suction side of the leading edge is displayed. It can be observed that evaporation grows with increasing diameter. Analog to the findings for the pressure coefficient distribution, setup iniHomog and the smallest diameter (disp1µm) are similar. For diameter 0.1 mm a re-entrant jet is forming that is also present for diameter 1 mm.

In the next step, the impact of the treatment of the vapor phase is investigated. The three different treatments continuous, monodisperse and polydisperse are compared. For the polydispersed simulation ten size groups are used and minimum and maximum diameter are set to 1 µm and 1 mm, respectively. Regarding the distribution of the pressure coefficient (see figure 4.4), the three different setups show a similar behavior and are in good agreement with the experiment. The comparison of the

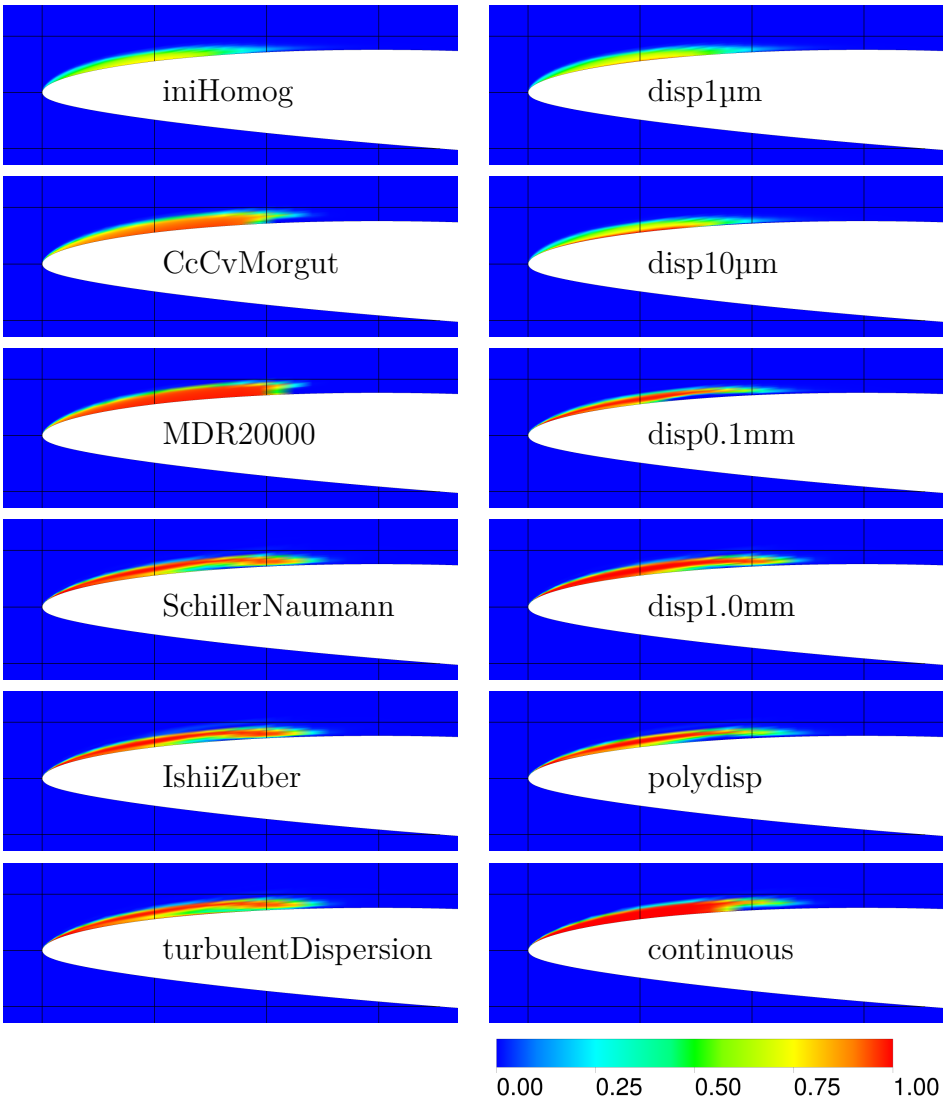

Figure 4.5: Visualization of the cavitation volume on the suction side of the NACA66mod hydrofoil. Shown is the vapor volume fraction. The abbreviation disp represents monodispersed results.

cavitation volume (see figure 4.5) indicates small differences. Monodispersed and polydispersed treatment show a similar formation of the re-entrant jet, but evaporation is slightly stronger for the monodispersed simulation. Contrary to that, the continuous treatment of the vapor phase results in a smaller re-entrant jet. Which of the three simulations is closest to the measurement cannot be answered as there is no experimental visualization available that would allow an assessment of the shape of cavitation volume.

Furthermore, the impact of the drag coefficient that is needed for the calculation of the drag force is evaluated. A comparison is made between setting the drag coefficient

to a constant value $C_D = 0.44$, using the Schiller Naumann drag model and the Ishii Zuber drag model (see also section 3.1.1). Both, distribution of pressure coefficient and shape of cavitation volume show only negligible differences. This leads to the conclusion that investigated flow fulfills the criteria for the application of a constant drag coefficient.

Last, it is investigated how turbulent dispersion force affects the simulation results. As displayed in figure 4.4 and 4.5 it has only minor effect and will consequently be neglected in further investigations. Furthermore, other interfacial forces like lift or virtual mass are neglected so that only drag force is taken into account.

All in all, it can be stated that for this test case a good agreement between simulation and measurement can be achieved for both, homogeneous and inhomogeneous two-phase modeling, when selecting appropriate parameters. As the NACA66mod test case is quite simple because it only contains a stable sheet cavity and no other forms like vortex induced cavitation, a second test case is investigated in the following.

4.2 NACA0009 with Tip Leakage Vortex

In this section different two-phase setups are investigated for the cavitating flow around a NACA0009 hydrofoil. Due to a gap between one side wall of the cavitation tunnel and the hydrofoil a tip leakage vortex forms. Besides the cavitating tip leakage vortex, cloud cavitation and a cavitating tip separation vortex occur (see figure 4.8). The occurrence of different forms of cavitation makes this test case more challenging compared to the NACA66mod investigations. At the cavitation tunnel of the EPFL a lot of experiments have been performed for the NACA0009 hydrofoil including variations of the gap width and incidence angle [52–54].

Different numerical studies were performed for this test case. In single-phase investigations the impact of gap width and incidence angle was analyzed [42]. The results of two-phase simulations using a mesh with around 2 million cells performed by Decaix et al. [43] indicate that the vorticity in the vortex core is underestimated. To obtain a cavitation volume similar to the one observed in the experiments, their simulations were thus carried out at significantly lower pressure level compared to measurement.

4.2.1 Setup

The NACA0009 foil has a chord length of $c = 0.1$ m and was truncated from initially 0.11 m. Furthermore, it is characterized by a maximum thickness $h_m = 9.9$ mm and a span of 0.15 m. To limit cavitation in the gap caused by the tip separation vortex, the foil tip is rounded on the pressure side with a radius of 1 mm [54]. The foil tip rounding is considered in the simulation model. However, to facilitate meshing, a small radius of 0.1 mm is put on the suction side of the blade that is not present in the experiments. That the foil tip rounding has a relevant impact on the numerical results was already observed by Guo et al. [71].

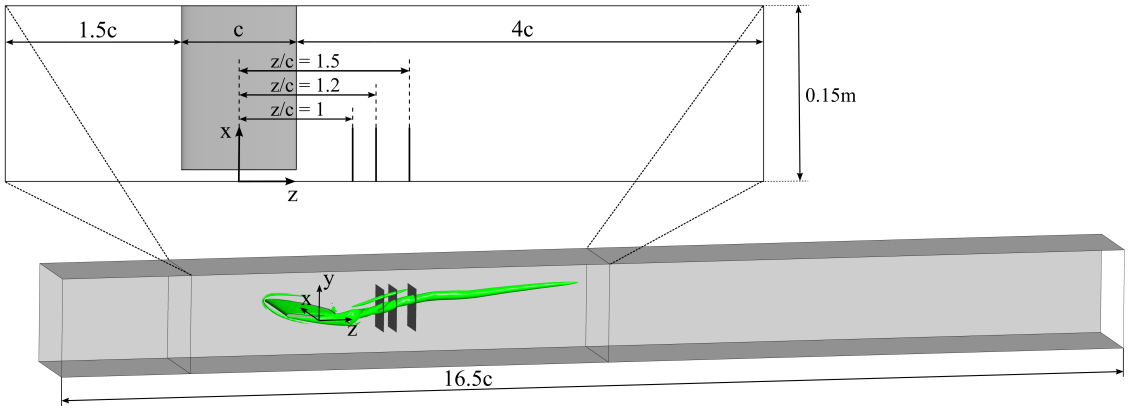

Figure 4.6: Simulation domain of the NACA0009 test case with the measurement planes. Top: Zoom on the top view of the main subdomain.

Within this study, all simulations are performed for 10° incidence angle and a normalized tip clearance $\tau = 1$, which is defined as the ratio of gap width and h_m. Analog to the NACA66mod case, a block profile is prescribed at the inlet boundary condition. There, a velocity $U_\infty = 9.78$ m/s is set, which corresponds to the equal discharge from the experiments with $w_{ref} = 10$ m/s. The small deviation results from the consideration of the boundary layer at the wall that is present in the measurements [54]. Furthermore, a turbulence intensity of 5% and an eddy length scale that corresponds to 5% of the chord length are set. The pressure level is prescribed by setting the average static pressure at the outlet boundary condition. For all simulations, the pressure level is characterized by the static pressure at the inlet $p_\infty = 1$ bar.

The total length of the simulation domain is 16.5 times c, with the inlet boundary condition located 3.5 chords upstream of the hydrofoil and the outlet boundary condition 12 chords downstream. The simulation domain consists of three subdomains (see figure 4.6) to reduce the total amount of cells. To accurately resolve the tip leakage

vortex, the region around the wing - extending from 1.5 chords upstream to 4 chords downstream of the hydrofoil - consists of a fine mesh. For the two subdomains away from the wing, a coarser mesh resolution is selected.

Spatial discretization is selected depending on the turbulence model. While for simulations with the SST model a high resolution scheme is applied, investigations with the SBES model are performed with a bounded central differencing scheme. All unsteady simulations use a second order backward Euler scheme for temporal discretization. The selected time step is 10^{-5} s, which corresponds to an RMS Courant number of 0.35.

Stereo PIV measurements of velocity components u, v and w at non-cavitating conditions are available for three measurement planes. These planes are located downstream of the wing at locations $z/c = 1$, 1.2 and 1.5 (see figure 4.6). The experimental results at non-cavitating conditions serve for selection of mesh resolution and turbulence model with a single-phase setup.

4.2.2 Single-Phase Investigations

For the selection of a suitable mesh resolution, a mesh study is performed with steady state single-phase simulations using the SST turbulence model. First, the global mesh refinement is investigated for a constant average y^+-value of 35. In figure 4.7, the representative cavitation volume of the tip leakage vortex is plotted over the number of cells. Therein, the representative cavitation volume of the tip leakage vortex is the volume of cells in the single-phase simulation where the static pressure falls below vapor pressure in the region of the tip leakage vortex. It can be observed that the coarsest meshes 4M and 11M cannot capture the low pressure region in appropriate manner. The results indicate that the issues of not correctly capturing the cavitation volume from Decaix et al. [43] can, at least in parts, be traced back to a too coarse mesh resolution.

In figure 4.7, the black dots represent meshes that are globally refined, while the blue dot (mesh 30M) uses the resolution of mesh 26M but with a local refinement in the region of the tip leakage vortex. It is obvious that mesh independent results are not fully achieved. However, a relevant low pressure region in the tip leakage vortex region exists for the finer meshes. Furthermore, the velocity profiles only show minor differences for the finer meshes [165] and the computational effort should remain in a feasible range. Based on this, the mesh with 30M is selected for further investigations.

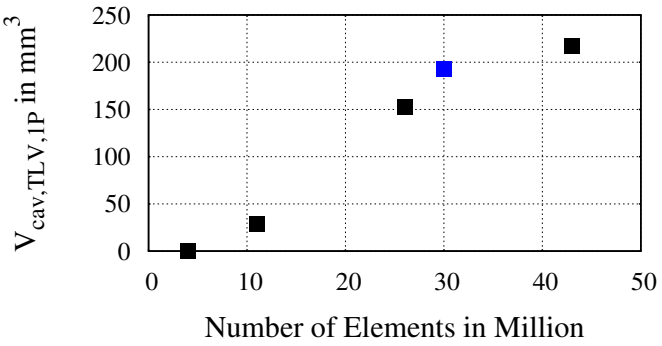

Figure 4.7: Representative cavitation volume of the tip leakage vortex from steady state single-phase simulations with different global mesh resolutions and an average y^+-value of 35.

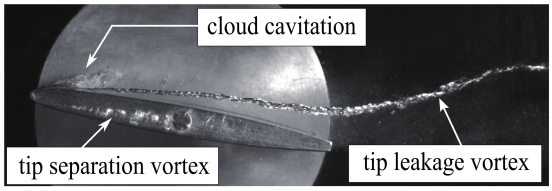

a) Experiment with cavitation [54]

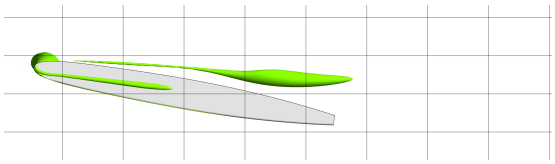

b) SST model without curvature correction

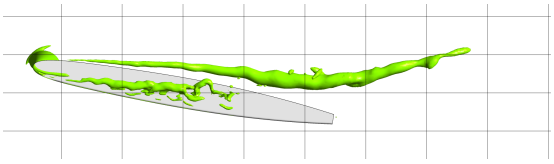

c) SBES model

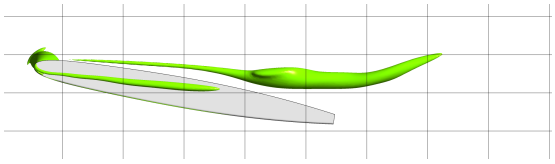

d) SST model with curvature correction

Figure 4.8: Visualization of regions in single-phase simulations with a high probability that cavitation occurs and comparison to measurement at cavitating conditions. Displayed is an instantaneous snapshot of the isosurface of the static pressure at vapor pressure.

In the next step of the mesh study, the boundary layer resolution was investigated. The results that are published more detailed in [165] show that the boundary layer resolution has a relevant impact on the developing velocity profile and a y^+-value of 1 should be used. Including a boundary layer resolution of $y^+ = 1$ results in the final mesh that has approximately 46M cells and is used in the following.

Finally, the impact of the turbulence model is analyzed with unsteady simulations. The investigated turbulence models are the SST model, the SST model with curvature correction (SSTwCC) and the SBES model. An isosurface of the static pressure at vapor pressure for an instantaneous snapshot is displayed in figure 4.8 and a high-speed picture of the experiments with cavitation is displayed for comparison. All

turbulence models can capture the tip leakage vortex and the tip separation vortex to some extent.

The SST model has the smallest region where static pressure is falling below vapor pressure. Concerning the length of the isosurface, SST model with curvature correction and SBES model are similar with a slightly longer extension for the SBES model. The fact that the low pressure region of a vortex is better captured by the SBES model compared to the SST model without curvature correction is in good agreement with simulations of the inter-blade vortices in a Francis turbine at deep part load conditions [167]. Furthermore, the results show that only the hybrid RANS-LES simulation can capture small scale turbulent structures that are especially present at the tip separation vortex in the gap but also at the tip leakage vortex. For all models it can be stated that cloud cavitation cannot be captured. This can be explained by the usage of single-phase simulations. As in the single-phase simulations no real cavity forms, a boundary layer separation does not occur (see also section 2.1).

To further quantify the accuracy of the simulations with different turbulence models, u-, v- and w-component of the velocity are compared to single-phase measurement results. In figure 4.9, the results for measurement plane $z/c = 1$ are shown along a line at $x/c = 0.12$ and a line at $y/c = 0.14$. These lines are selected to pass the regions of highest velocity gradients from the measurements. They are also displayed in figure 4.10.

For the u-component, the velocity minimum at $y/c = 0.05$ is best met by the SST model. On the other hand, the SBES model can better capture the steep velocity gradient around $y/c = 0.15$ and the velocity maximum at $y/c = 0.2$. Furthermore, the SBES model can resolve features from the experiment like change in slope around $y/c = 0.1$ and $y/c = 0.25$ that are not captured by the RANS simulations. Regarding the v-component, RANS models show a better agreement with the measurement compared to SBES model in the region close to the wall of the cavitation tunnel ($x/c < 0.1$). The steep gradient around $x/c < 0.12$, which results from the tip leakage vortex, is better captured by the simulations SSTwCC and SBES. For the w-component, the SST model with curvature correction shows the best agreement with the experiment as it is the only simulation that has also a distinct velocity maximum at $x/c \approx 0.12$.

A contour plot of all velocity components is displayed in figure 4.10. As already identified in the velocity distribution along the lines, the turbulence model has a relevant effect on the results. The SST model, for instance, fails to accurately predict the steep gradients caused by the tip leakage vortex that can be observed in u- and v-component

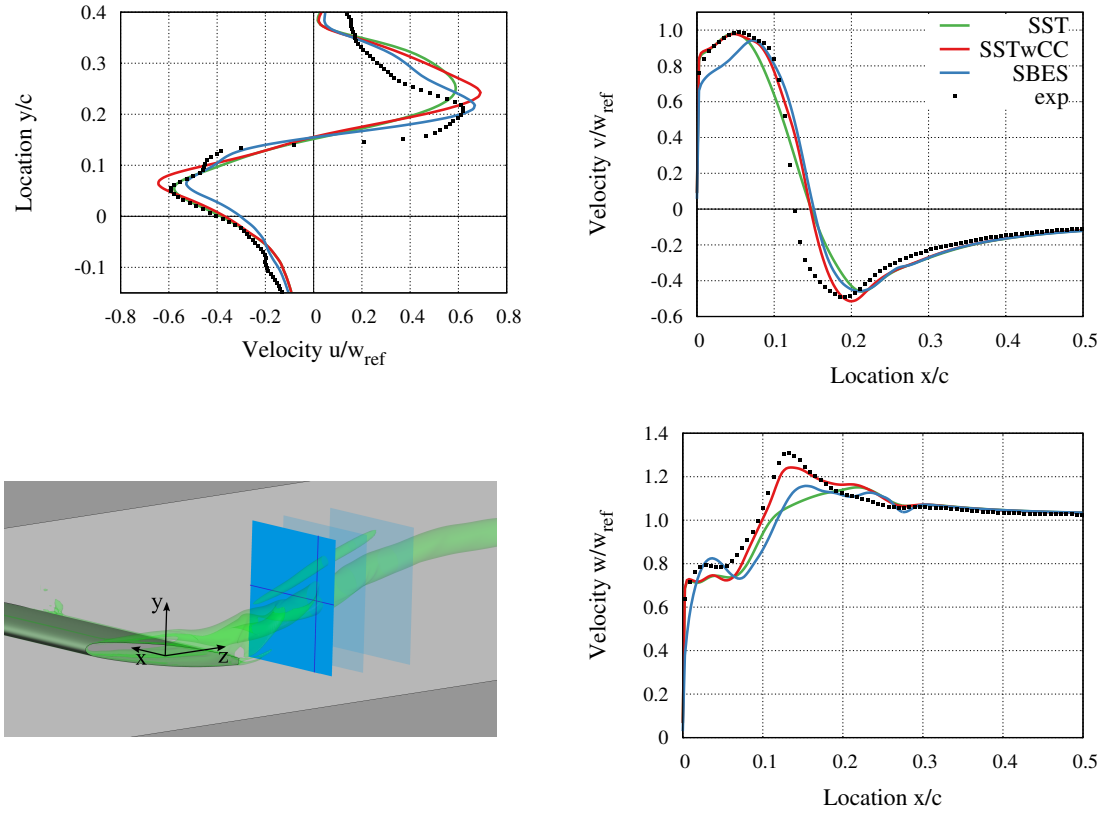

Figure 4.9: Distribution of averaged u-, v- and w-component of the velocity along line in x- or y-direction, respectively, at measurement plane $z/c = 1$. The lines are located at $x/c = 0.120$ and $y/c = 0.139$. Experiments were performed by Dreyer et al. [54]. Velocities are made dimensionless with $w_{ref} = U_\infty = 10\,\mathrm{m/s}$.

(compare range between maximum and minimum velocity around $x/c \approx 0.12$). This results in reduced vorticity and can explain the shorter extension of the low pressure region in figure 4.8 compared to the other models. Regarding the u-component, the SBES model shows the best qualitative agreement with the measurement in the region $y/c < 0$. For the w-component, the RANS simulations can better capture the region of velocity deficit around $y/c \approx -0.12$ and $x/c > 0.2$ that is caused by the wake of the hydrofoil. As already identified in the line plot, the best qualitative agreement with the experiment for the w-component can be achieved with the SST model with curvature correction.

The results for the measurement planes located at $z/c = 1.2$ and 1.5 are not discussed here as they show similar tendencies. For the interested reader the results are attached in appendix A.

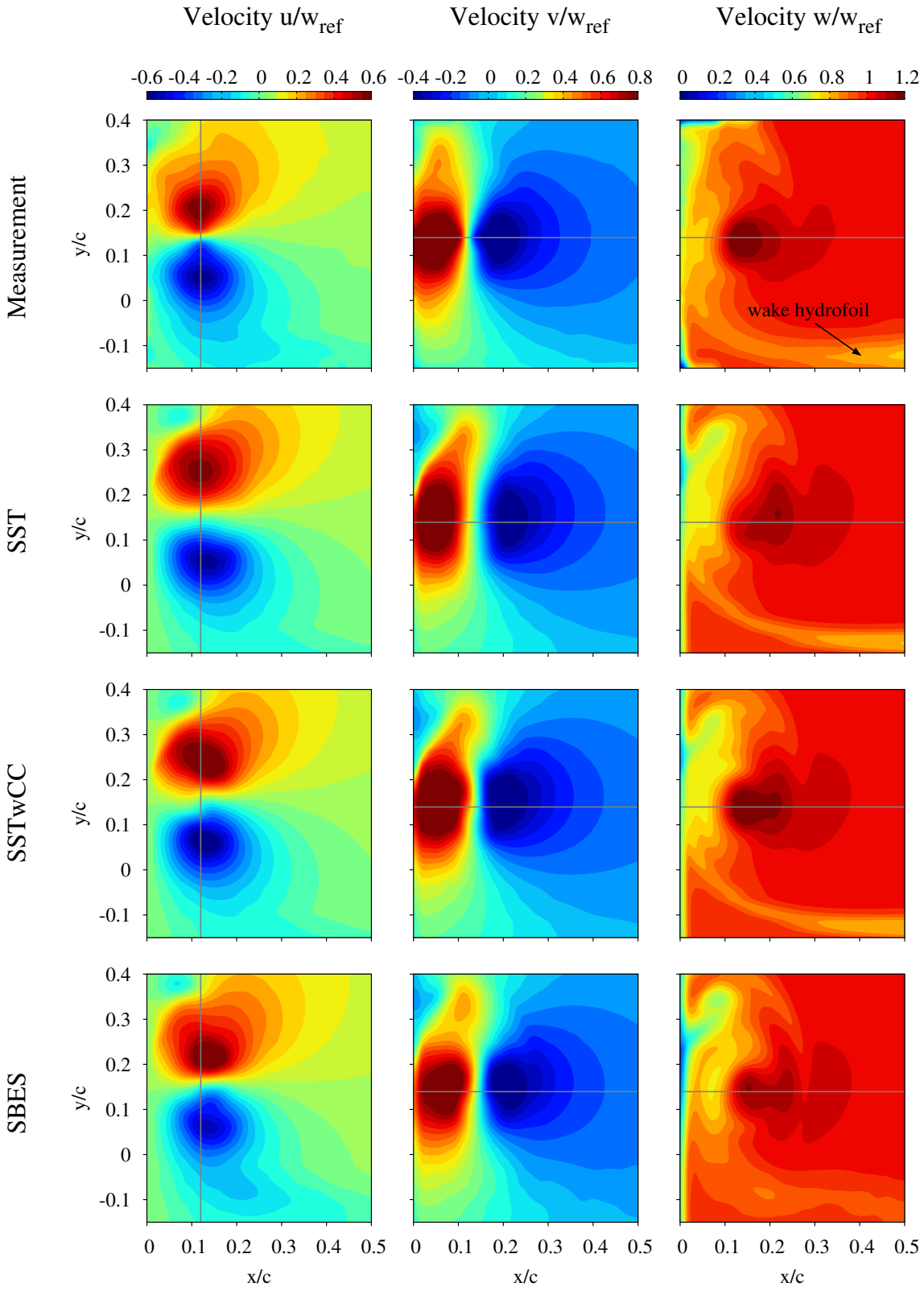

Figure 4.10: Contour plot of the dimensionless velocity components u, v and w in measurement plane $z/c = 1$ for measurement [54] and single-phase simulations with different turbulence models.

All in all, it can be summarized that the three turbulence models result in different velocity distribution. Every model has regions where significant deviations to the measurement can be observed. Nevertheless, it can be concluded that SSTwCC model and SBES model show a better agreement with the experiment compared to the SST model. They are thus used for further two-phase investigations.

4.2.3 Two-Phase Investigations

The investigations on the NACA66mod hydrofoil showed that variations of the two-phase modeling resulted in a different extension of the cavity length. Consequently, further two-phase analyses are performed for the NACA0009 case. For this test case, no velocity profiles were measured for cavitating conditions. The only available data from two-phase experiments are images that were recorded with a high speed camera. On the one hand, single images can be compared with instantaneous snapshots from the different simulation results. On the other hand, the superposition of hundreds of images allows making a comparison with time-averaged results.

In figure 4.11, the cavitation regions for various simulation setups are displayed and can be compared with the experiment. The cavitation regions are displayed by iso-surfaces of the vapor volume fraction at two different thresholds. At first glance, it can be stated that the turbulence model has a much more significant impact on the developing cavitation regions. While the result with the SST model with curvature correction is significantly different, the other simulation results resemble one another.

A comparison of the cloud cavitation at the leading edge shows that the setup that uses the SST model with curvature correction underestimates the cavitation occurrence in this region compared to the measurement. On the other hand, the SBES simulations overestimate cavitation at the leading edge. Concerning the tip separation vortex, again the SBES simulations overestimate the cavitation compared to the experiment. Nevertheless, in the instantaneous snapshots it can be observed that vortical structures can be observed. Contrary to that, these vortical structures are not present for the SST model with curvature correction. However, for that setup a better agreement with the measurement can be stated for the cavitation volume of the tip separation vortex.

For all simulation setups the occurrence of the cavitating tip leakage vortex shows a reasonable agreement with the experiment in the region up to two thirds of the chord length. After that the SBES simulations suffer from the fact that the overestimated tip

a) Experiment [54]

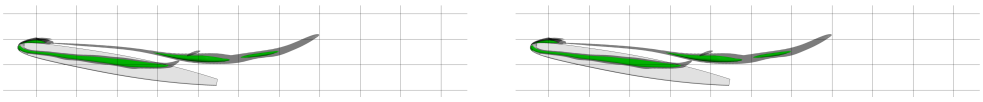

b) Homogeneous - SSTwCC - model constants Zwart

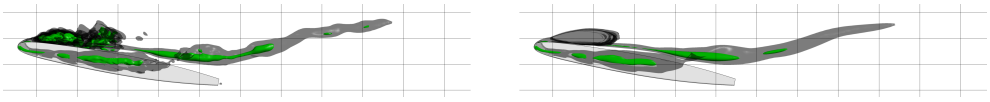

c) Homogeneous - SBES - model constants Zwart

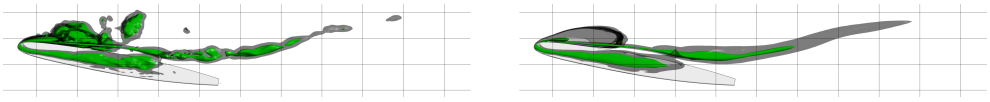

d) Homogeneous - SBES - model constants Morgut

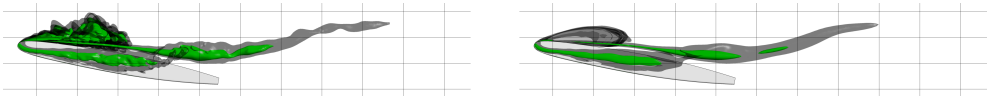

e) Inhomogeneous - SBES - dispersed 0.01 mm - drag $C_D = 0.44$

f) Inhomogeneous - SBES - dispersed 0.1 mm - drag $C_D = 0.44$

g) Inhomogeneous - SBES - polydispersed - drag $C_D = 0.44$

h) Inhomogeneous - SBES - dispersed 0.01 mm - drag Schiller Naumann

Figure 4.11: Visualization of the cavitation volume with two isosurfaces - $\alpha_v = 0.5$ and $\alpha_v = 0.05$ - of the vapor volume fraction. Left: Instantaneous snapshot. Right: Time-averaged result over 20,000 time steps.

separation vortex unites with the tip leakage vortex. This results in an overestimated cavitating vortex diameter further downstream. Only the RANS simulation does not show the massive increase of cavitation volume in that region. However, the RANS simulation underestimates the extension of cavitation occurrence of the tip leakage vortex.

To recognize differences between the different simulations with the SBES turbulence model a close look is necessary. For the homogeneous model the variation of the cavitation model constants from Zwart to Morgut results in a slightly bigger cavitation volume in all regions. This is in agreement to the observations made on the NACA66mod hydrofoil but less distinct. Comparing the inhomogeneous results with dispersed phase diameter 0.01 mm, 0.1 mm and polydispersed treatment also shows a slight increase in the cavitation volume, which matches the findings from the NACA66mod test case. It has to mentioned that the use of a dispersed phase diameter of 1 mm resulted in a diverging simulation. This can be explained by an increased relative velocity between liquid and vapor phase that has a negative impact on the robustness of the simulation. Finally, the simulation result using a constant drag coefficient is very similar to the results obtained with the Schiller Naumann model, which is also in agreement with the observations made on the NACA66mod test case.

All in all, it can be concluded that the turbulence model plays an important role while the use of the inhomogeneous model does not lead to a significantly increased simulation accuracy that would justify the higher computational effort. This can be explained with the dimensionless Stokes number (see section 3.1.4). Due to the small density of the vapor phase and relatively small bubble diameters, a velocity equilibrium can be assumed between cavitation bubbles and the surrounding water ($St \ll 1$), which is the assumption of the homogeneous model.

4.3 Summary and Discussion

The results from the test cases show that there are several factors that can significantly affect the accuracy of two-phase simulations. First, the two-phase modelling can have a relevant impact on the results. For the NACA66mod case a good agreement with the experiments could be achieved by using the homogeneous model with either adapted constants of the cavitation model or increased maximum density ratio. Similar results could be obtained with the inhomogeneous model with a dispersed phase diameter of 1 mm or polydispersed treatment. For the NACA0009 hydrofoil the same trends could

be observed as for the NACA66mod case, but the changes between different two-phase modelling setups were significantly smaller. All in all, it can be concluded that for both test cases a setup with the homogeneous model exists that has a similar level of accuracy to a setup with the inhomogeneous model. Consequently, the homogeneous model is used for further investigations on the Francis turbine as it has the lower computational effort and the simulations are more robust.

Furthermore, the turbulence model plays a major role for simulations with relevant vortical structures, like for the NACA0009 test case. There, the use of the SST model with curvature correction and the SBES model showed the best agreement with the experiment. Nevertheless, with both models deviations to the measurement could be observed.

Another important factor for vortex induced cavitation is the use of a suitable computational grid. In the vortex core a pressure minimum develops that needs to be resolved by a fine mesh resolution. This is crucial as otherwise cavitation occurrence is significantly underestimated.

5 Francis Turbine Full Load Instability

In this chapter, which consists of three parts, the physical mechanism behind the full load instability in a Francis turbine is analyzed. First, the setup is described and validation is performed. Thereafter, the results from simulations at several constant cavitation numbers in the range of the instability onset are used to identify significant characteristic changes in the flow field from stable to unstable conditions. Finally, different simulations are performed for the transition from stable to unstable to further investigate the cause of the instability.

5.1 Setup and Validation

In this section, the applied setup is described. First, geometry and investigated operating point are outlined. Thereafter, the concept for data analysis is presented, followed by the numerical setup. Finally, the results of the validation are presented.

5.1.1 Geometry and Operating Point

The investigated model Francis turbine has a specific speed $n_q \approx 43\,\mathrm{min}^{-1}$ and consists of 20 stay and guide vanes and 16 runner blades. For the simulations, the components spiral case (SC), stay and guide vanes (SVGV), runner (RU) and draft tube (DT) are considered (see figure 5.1).

In the scope of this thesis, a full load operating point is analyzed that has a discharge factor $Q_{ED} = 0.260$ and a speed factor $n_{ED} = 0.288$. Compared to best efficiency point (BEP) the discharge is increased by factor 1.3. The guide vane opening is 28°, which is around 8° wider opened compared to BEP. Based on IEC 60193 [76] the Reynolds number is $5.1 \cdot 10^6$. For the investigated operating point, the full load instability occurs when the cavitation number is decreased below a certain value. In figure 5.2, the measurement results for a transition from stable to unstable and back to stable conditions are displayed. It can be observed that the amplitude of pressure fluctuations is moderate down to a critical cavitation number, which is approximately 0.155

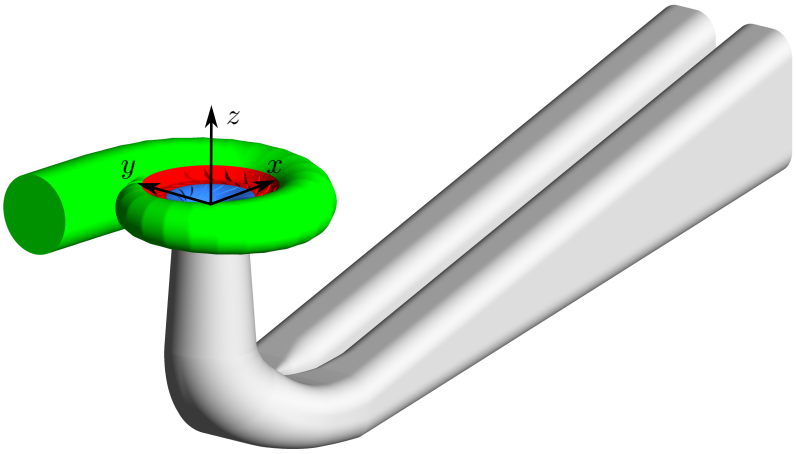

Figure 5.1: Simulation domain of the Francis turbine.

in the measurements. Below this σ-value, the pressure fluctuations increase dramatically, which characterizes the regime of the instability. When the cavitation number increases, around 0.155 the pressure fluctuations reduce significantly and a transition back to stable conditions takes place.

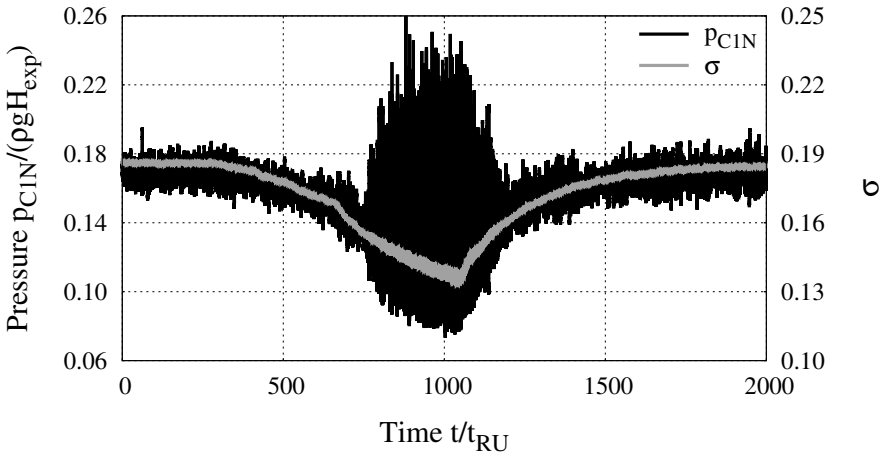

Figure 5.2: Transition from stable to unstable conditions. Experiments were performed by EPFL. The location C1N can be found in figure 5.3.

5.1.2 Concept for Data Analysis

In the scope of this thesis, simulation results are analyzed at different points, lines and planes. The focus is on runner outflow and the flow in the draft tube cone (see figure 5.3). In the draft tube cone, data analysis is performed in four planes that are located equally spaced in z-direction. The planes are located approximately 0.05,

0.39, 0.73 and 1.08 times $D_{\bar{1}}$ below the runner exit, where $D_{\bar{1}}$ denotes the outer runner outlet diameter. For comparison of velocity distributions, the results are investigated along lines in x-direction that are situated in the different planes. Furthermore, the locations C1N and C2N that are situated at the draft tube wall are used for the analysis of pressure fluctuations.

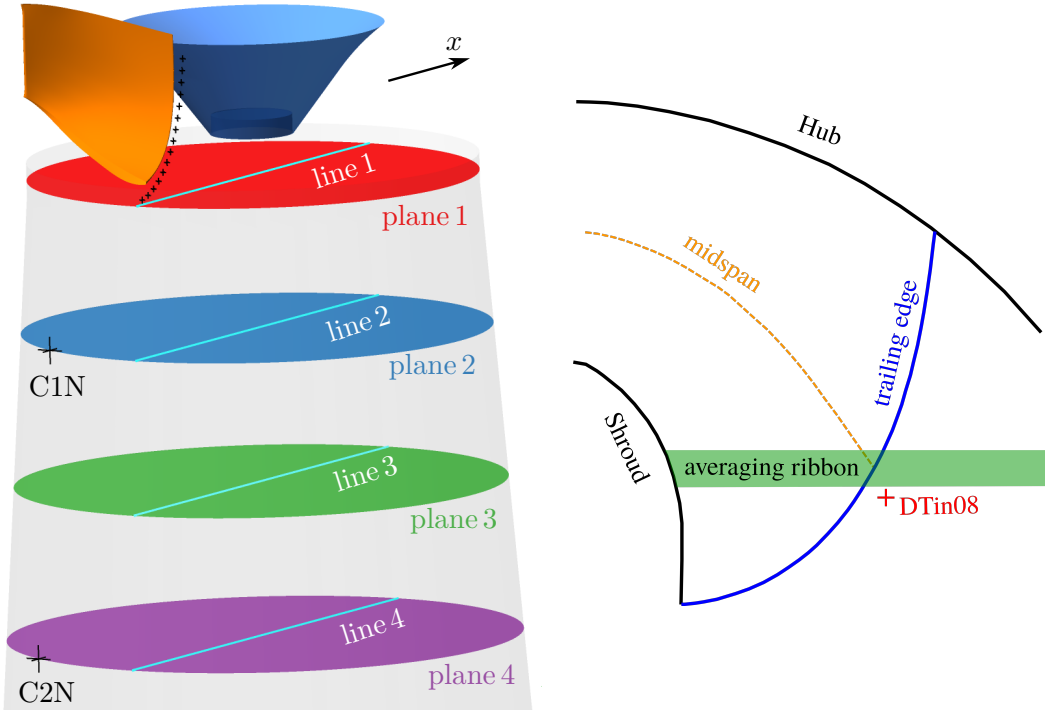

Figure 5.3: Location of points, lines and planes that are used for data analysis. On the right the averaging ribbon that corresponds to point DTin08 is displayed in green.

To investigate the role of variations of velocity components and relative flow angle β at the runner exit on the onset of the full load instability, monitor points are set downstream of the runner blades. As these monitor points have fixed locations, while the runner is rotating, the wake of the runner blades occurs periodically in the results. The monitor points are located along a line that follows the course of the runner trailing edge and are equally spaced. In the scope of this thesis, the focus of data analysis is on point DTin08, which corresponds to midspan and is consequently related to the mid of the runner blade. To be able to get a correlation between evaluated quantities at the monitor points and the occurrence of blade cavitation, averaging ribbons are defined. They are used to get one characteristic value of the blade cavitation volume for the corresponding ribbon. An averaging ribbon consists of the volume between two xy-planes that have a small offset in z-direction. Exemplarily, the averaging ribbon

that corresponds to monitor point DTin08 is displayed in green on the right side of figure 5.3. The reason why this averaging ribbon is located higher than point DTin08 is that the monitor points are situated slightly downstream of the runner trailing edge.

Mean Phase Averaging

For the full load instability a well-established periodicity is characteristic that can be found in quantities like pressure fluctuations or oscillation of the cavitation volume. However, small variations in frequency can be observed between different instability cycles. Consequently, it is useful to determine mean phase averaged results that facilitate to determine correlations that are valid for all cycles. To split the signal into its different cycles, the cavitation volume oscillation is used. As the simulation results show a clear minimum of cavitation volume it is used as trigger to detect the different cycles (see figure 5.4).

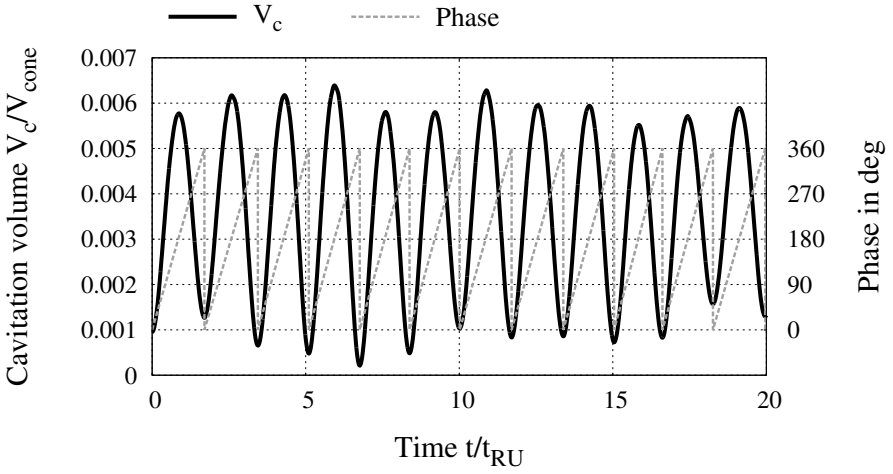

Figure 5.4: Cavitation volume oscillation and phase angle for $\sigma = 0.21$.

In figure 5.5, it is investigated how the number of instability cycles that are used for the averaging affects the solution. The plot shows the cavitation volume in the draft tube over swirl number at plane 2 for $\sigma = 0.21$. It shows that the use of more than ten instability cycles leads to only minor changes of the phase averaged results, while for six and eight cycles still relevant differences can be observed. The curve for eight cycles shows a small jump around minimum cavitation volume that looks at first glance like an evaluation error. However, this can be explained by the differences between the start of the first cycle and the end of the last cycle. In figure 5.4 it can be seen that in the case that eight cycles are used for the averaging, the first cycle ($t/t_{RU} \approx 6.33$)

starts at very small cavitation volume, while the last cycle ($t/t_{RU} \approx 20.0$) ends at significantly higher cavitation volume. With increasing number of cycles this effect diminishes with the disadvantage that the computational cost increases.

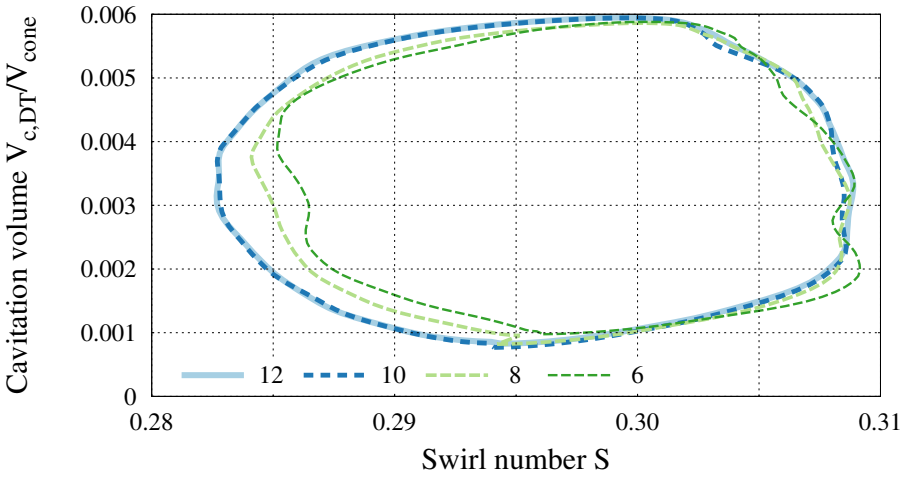

Figure 5.5: Evaluation of the necessary amount of cycles that are used for the phase averaging. The results originate from location plane 2 and the pressure level for the simulation is $\sigma = 0.21$.

For the other planes, other cavitation numbers and other quantities similar observations can be made. Consequently, it is concluded that the use of twelve instability cycles for the phase averaging is suitable for the following investigations. All phase averaged results that are presented in the following have an angular window size of 2.5°, which is selected similar to experimental studies [121].

5.1.3 Numerical Setup

The numerical setup of the Francis turbine is based on the findings of the test cases. Consequently, all two-phase simulations are carried out with the homogeneous multiphase modeling approach. Spatial discretization is just like for the NACA0009 test case, which means that for the RANS simulations a high resolution scheme is used and a bounded central differencing scheme is applied to simulations with the SBES model. Furthermore, all unsteady simulations are performed with a second order backward Euler scheme for temporal discretization.

The boundary conditions are set as follows: At the inlet of the spiral case, a constant mass flow is prescribed. This is contrary to the findings from a previous study [163], which stated that a constant mass flow boundary condition is not suitable to capture

the full load instability. A thorough discussion on this will be made later in this thesis. At the outlet, the static pressure is set. Thereby, six different constant values are prescribed for the simulation results that are presented in section 5.2 and the pressure is lowered for the results in section 5.3. Furthermore, interfaces are needed between the subdomains. While between neighboring stationary parts a general grid interface (GGI) is applied, a transient rotor stator approach is used between stationary and rotating parts.

In a previous study [166], it was observed that the shape of the runner nut has a significant impact on the shape of the cavitation volume in the draft tube. Consequently, the geometry of the runner nut that is used for the simulations is chosen to be as close as possible to the geometry that was used for the measurements. Furthermore, the study showed that the impact of cavitation model constants is negligible but curvature correction leads to a more accurate prediction of the length of the cavitating vortex rope for RANS. Thus, all following simulation results use the model constants proposed by Zwart and all simulations with the SST model include curvature correction.

Table 5.1: Mesh size of the subdomains for used grids in million elements.

	SC	SVGV	RU	DT	total
14M	0.7	2.2	5.9	4.9	13.7
48M	1.3	21.6	19.4	5.6	47.9

Additionally, a mesh study was performed with single-phase steady state simulations that concluded that the mesh resolution of the runner mesh has the biggest impact [166]. The proposed mesh has an average y^+-value of 1 and around 48 million cells (48M) in total. In table 5.1, the distribution for the different subdomains is listed that shows that the majority of cells are in the parts SVGV and RU. As the computational effort is significant for a fine mesh with 48M cells, a second mesh is used within this study to have a setup that is feasible to perform a variety of different simulations. This mesh has 14 million cells (14M) in total and is based on the findings from the mesh study. Consequently, the highest mesh resolution can be found in the runner, as this showed the highest sensitivity regarding the integral quantities head and torque as well as quantities that are important for two-phase investigations like minimum pressure in the draft tube cone. To save cells, the boundary layer is resolved with an average y^+-value of approximately 50, which means that wall functions are used. As only some of the following simulation results are performed with mesh 48M,

they are labeled accordingly, while unspecified simulation results are from simulations with mesh 14M.

The time step for the simulation with the SBES model is selected to fulfill the criterion that the RMS Courant number should be below 1. This results in a time step that corresponds to a runner rotation of 0.24°. For the simulations with the SST model the time step size is less restricted and for that reason a time step that corresponds to 0.96° of runner revolution is selected, which is based on findings of a two-phase investigation at stable conditions [166].

Finally, an appropriate number of coefficient loops needs to be set, which corresponds to the number of iterations that are performed within one time step before going on with the next time step. In literature, at least two examples can be found that state numerical issues at the moment of pressure peak for the simulation of a Francis turbine facing a full load instability (see [21, 44]). Furthermore, previous investigations identified that increasing the number of coefficient loops leads to a more robust simulation setup [163]. A suitable measure to analyze the number of necessary coefficient loops is how good the continuity equation 2.9 is fulfilled.

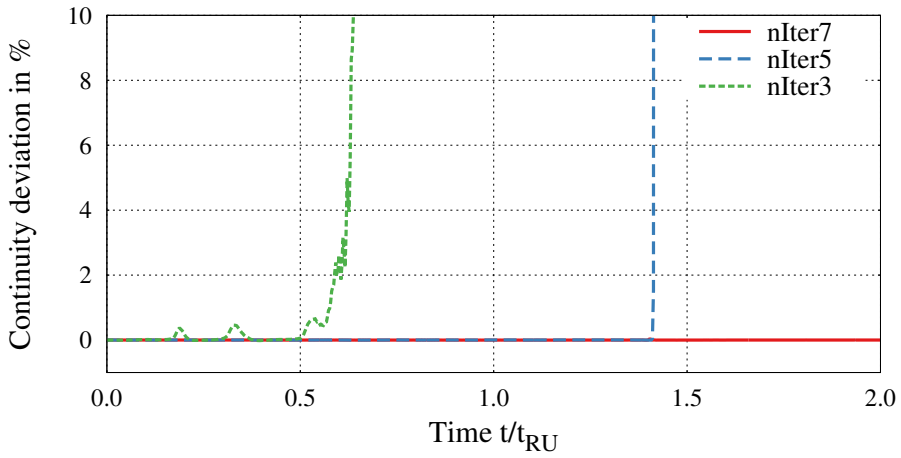

Figure 5.6: Deviation from continuity equation 2.9 for one instability cycle at $\sigma = 0.19$. Investigated is the impact of the number of coefficient loops.

This is investigated for $\sigma = 0.19$, which corresponds to unstable conditions in the simulation. In figure 5.6, the deviation from continuity equation within an instability cycle is displayed for three, five and seven coefficient loops. With only three coefficient loops, continuity equation is violated quite early. Shortly after half a runner revolution the deviations become too large and simulation diverges. With five coefficient loops, continuity equation is fulfilled over a longer period. However, after approximately

1.4 runner revolutions it comes to a sudden violation of continuity equation that results in a diverging simulation. This moment coincides with the occurrence of a huge pressure peak when the cavitation volume is minimal. Continuity equation is satisfied over the whole range only with seven coefficient loops.

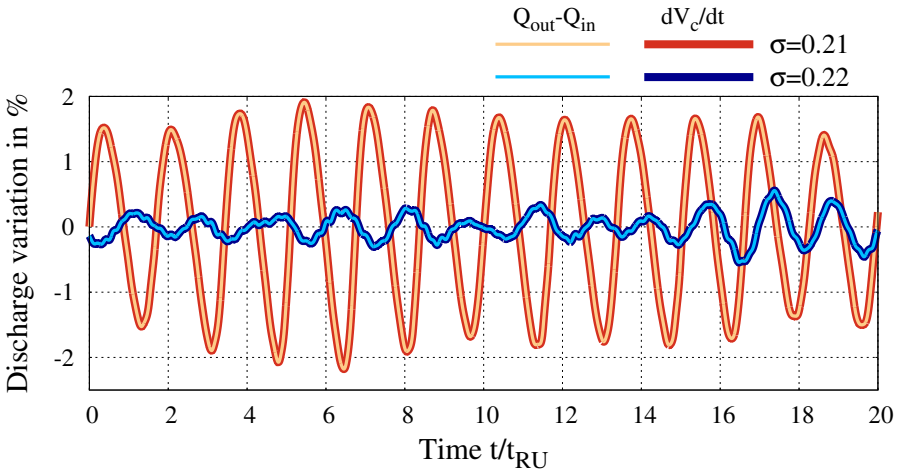

Figure 5.7: Discharge variations $Q_{out} - Q_{in}$ in the simulation domain caused by cavitation and first time derivative of the cavitation volume dV_c/dt for $\sigma = 0.21$ and 0.22. All results are made nondimensional by dividing by Q_{in}. When the curves for $Q_{out} - Q_{in}$ and dV_c/dt lie on top of each other continuity equation 2.9 is satisfied.

To show that this number of coefficient loops is also valid for other cavitation numbers and is appropriate for the following investigations, dV_c/dt and $Q_{out} - Q_{in}$ are plotted in figure 5.7 over 20 runner revolutions for $\sigma = 0.21$ and 0.22. For both conditions, it can be observed that the course of dV_c/dt and $Q_{out} - Q_{in}$ matches and consequently continuity equation is satisfied. The different amplitude for the two cavitation numbers results from the fact that $\sigma = 0.21$ corresponds to unstable conditions, while at $\sigma = 0.22$ stable conditions can be observed. All in all, it can be stated that seven coefficient loops are suitable for stable and unstable conditions.

5.1.4 Validation

For validation of the simulation setup, simulation results are compared with experimental results for $\sigma = 0.37$. This cavitation number corresponds to a quite high pressure level for which no cavitation occurs in the runner and only a thin and stable cavitating vortex rope can be observed in the draft tube cone. At the described conditions, PIV measurements are available that allows to validate the simulation setup

by a comparison of axial and circumferential velocity distribution that are displayed for line 2 in figure 5.8.

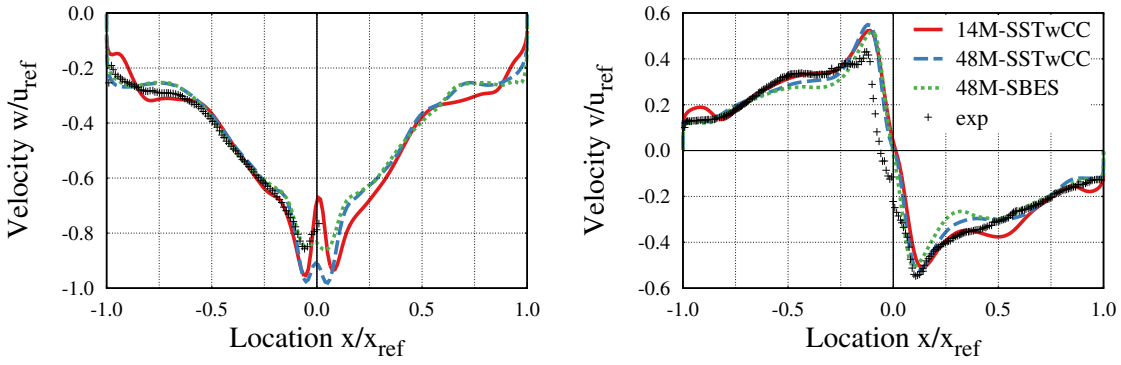

Figure 5.8: Averaged axial (left) and circumferential (right) velocity distribution along line 2 for $\sigma = 0.37$. Experiments performed by EPFL and published by Decaix et al. [44].

A comparison of the different simulations with mesh 48M shows that the RANS simulation and the simulation with the SBES model have a similar axial velocity distribution over a wide range. Significant differences can only be observed in the center of the draft tube cone that indicates that the cavitating vortex rope behaves different between these setups. The RANS simulation with mesh 14M shows differences for axial velocity in the outer region of the draft tube ($|x/x_{ref}| > 0.6$) and also in the center in the region of the cavitating vortex rope. A comparison with the experimental data shows that all setups can accurately predict the velocity distribution in the range $-0.6 < x/x_{ref} < -0.25$. The regions close to the draft tube wall and around the cavitating vortex rope in the center of the draft tube cone show deviations for all setups. In the center, the maximum deviation of the RANS simulations is around 10%. However, it has to be taken into account that in this region measurement accuracy may suffer from the occurrence of the vapor phase.

For circumferential velocity distribution, again, a comparison of RANS and SBES simulation show the highest difference in the inner part of the draft tube cone ($|x/x_{ref}| < 0.5$) for mesh 48M. The coarse mesh differs especially in the regions close to the draft tube wall and in the region $0.2 < x/x_{ref} < 0.6$. A comparison with the experimental data show that the simulations with the finer mesh are in better agreement with the measurement in the region close to the wall. Nevertheless, the simulation with mesh 14M has a better agreement with the experimental results in the regions $-0.6 < x/x_{ref} < -0.25$ and $0.2 < x/x_{ref} < 0.35$. All in all, it can be concluded that for axial and circumferential velocity the coarser mesh has a slightly

higher deviation to the experimental results. However, this deviation is still in a range that appears to be tolerable.

Another important analysis that needs to be performed for validation of the simulation setup is how well the cavitation volume can be predicted by the different simulation setups. High-speed recordings of the experiments are presented in figure 5.9 that allows carrying out a qualitative comparison. To facilitate the comparison between simulation and measurement, the simulation results are displayed in perspective view.

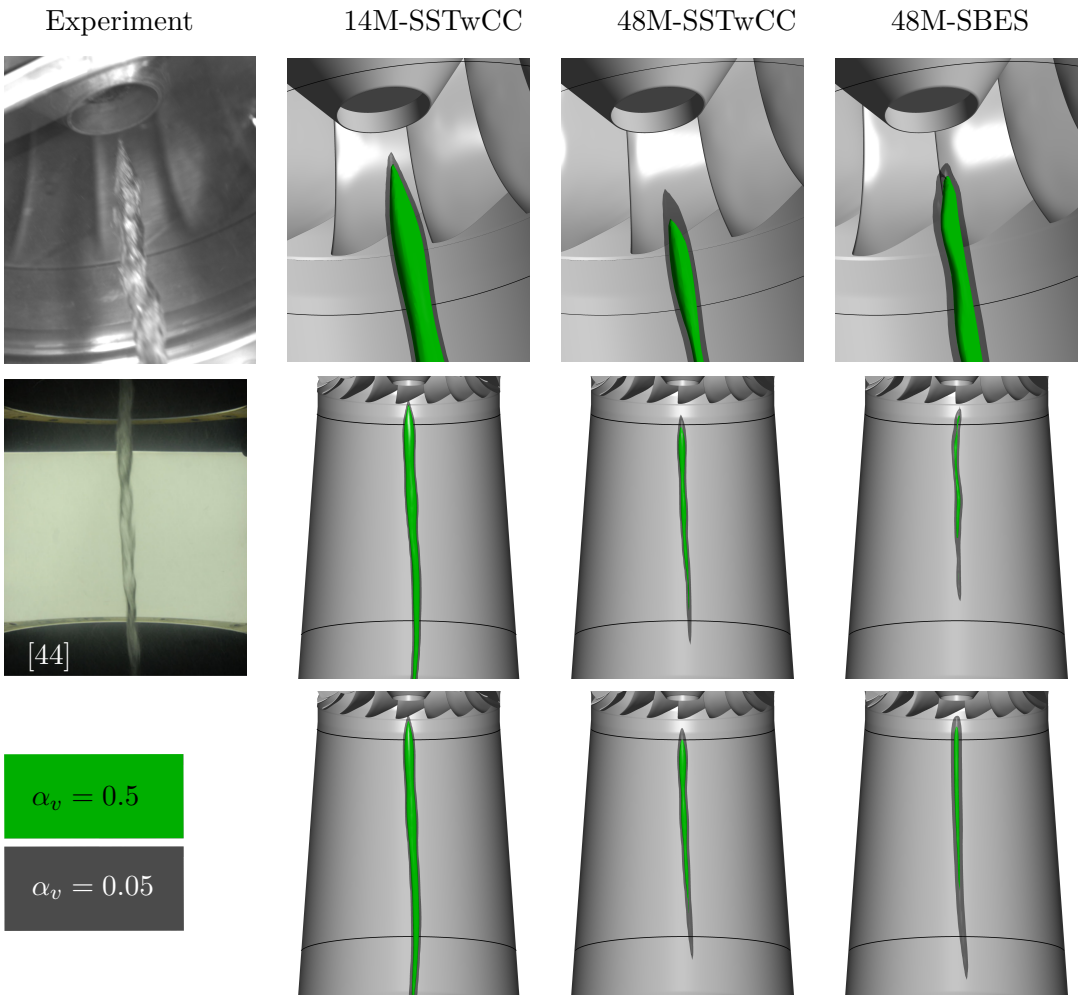

Figure 5.9: Visualization of the cavitation volume with two different isosurfaces of the vapor volume fraction for $\sigma = 0.37$. To facilitate the comparison between simulation and measurement, the simulation results are displayed in perspective view. Top: Instantaneous snapshot - Zoom to the runner nut. Middle: Instantaneous snapshot. Bottom: Time-averaged results.

In the upper part of figure 5.9, a comparison of the observed cavitation volume in the region of the runner nut can be performed. For all simulation setups as well as the

experiment the cavitation volume is not connected to the runner nut. Qualitatively, the RANS simulation with mesh 14M shows the best agreement with the measurement as on the one hand the distance of the cavitation volume to the runner nut is met best. On the other hand the thickness of the observed cavitation volume agrees well with the experimental observations.

In the middle row of figure 5.9, a snapshot is presented that shows a side view onto the draft tube cone and in the last row, additionally, the time-averaged simulation results are presented. Again, the RANS simulation setup with mesh 14M shows qualitatively the best agreement as it has a long extension and also the diameter of the cavitating vortex rope is met best. The instantaneous snapshot and averaged results show only negligible differences for both RANS simulations, which indicates that a stable cavitation volume develops. Contrary to this, a huge difference between instantaneous snapshot and averaged results can be observed for SBES simulation results. This is caused by an oscillation of the cavitation volume for this setup, which is not present in the experiments. The oscillation of cavitation volume comes across with significant pressure fluctuations that are displayed in figure 5.10 and are a result of equation 2.15.

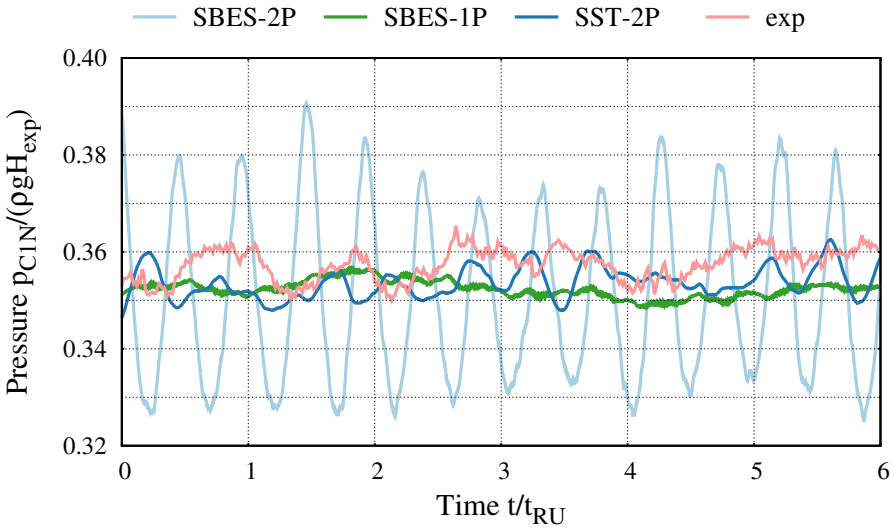

Figure 5.10: Pressure at location C1N for $\sigma = 0.37$. All presented simulation results are for mesh 48M. For the SST simulation curvature correction is applied.

Only minor pressure fluctuations can be observed in the measurement for pressure probe C1N. While the results for the RANS simulation (SSTwCC) show a similar amplitude of pressure oscillations, the two-phase simulation results with the SBES model differ substantially. Contrary to this, single-phase simulation results, with apart from that the same simulation setup, show a similar behavior as observed in the

experiments. Consequently, it can be concluded that the significant differences of the two-phase simulation with the SBES model are a result of an unphysical interaction of turbulence model and the multi-phase modeling. The unphysical results from the two-phase simulation with the SBES model show characteristics that are similar to those that can be observed when it comes to the full load instability. Thus, it is not suitable to use this setup for further investigations on the full load instability and all further analysis are performed with the SST model with curvature correction.

5.2 Simulations with Constant Cavitation Number

To get an insight into the physical mechanism behind the full load instability it is crucial to understand the changes in the flow field from stable to unstable conditions. For that purpose, unsteady simulations are performed for the following cavitation numbers: 0.15, 0.19, 0.21, 0.22, 0.23 and 0.25. In the first part of this section, time-averaged simulation results are presented for various quantities. After that, the unsteady behavior of the instability is analyzed. Finally, an explanation for the development of the full load instability is proposed.

5.2.1 Time-Averaged Quantities

Within this section, all quantities are time-averaged. While the results for stable conditions are averaged over 20 runner revolutions, for unstable conditions the averaging period consists of 12 instability cycles. For mesh 14M these 12 instability cycle correspond to 22.2 runner revolutions for $\sigma = 0.15$, 21.1 runner revolutions for $\sigma = 0.19$ and 20.0 runner revolutions for $\sigma = 0.21$.

Results for Mesh 14M

In figure 5.11, the average static pressure at measurement location C1N is displayed for different cavitation numbers. As expected, the average static pressure decreases with decreasing σ. More interesting is a comparison of the standard deviation, which can be seen as a measure for the amplitude of pressure fluctuations. Standard deviation is low for high cavitation numbers ($\sigma \geq 0.22$). However, a small reduction in the pressure level from $\sigma = 0.22$ to 0.21 results in a significant increase of standard deviation, which illustrates the transition from stable to unstable conditions. It has to be noted that

a high standard deviation can result in a high standard error of the mean. However, this error is negligible within this study as approximatly 8,000 time steps are taken into account for the averaging.

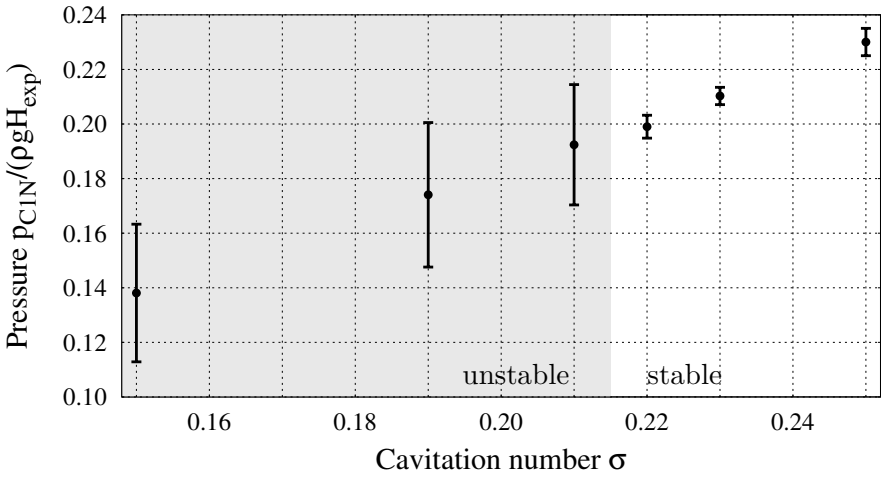

Figure 5.11: Time-averaged static pressure at measurement location C1N and standard deviation for different cavitation numbers.

In figure 5.12, the average cavitation volume in the draft tube and the standard deviation are plotted for different cavitation numbers. For stable conditions it behaves as expected: With decreasing cavitation number the cavitation volume increases. The reason for this, which is referred to as effect 1 in the following, is that for smaller pressure levels the size of regions that fall below vapor pressure increases. However, for unstable conditions the average cavitation volume in the draft tube does not further increase and even decreases for low cavitation numbers compared to the volume at $\sigma = 0.22$. This unexpected behavior indicates that some second effect, which acts contrary to the pressure reduction, is superimposed and gets relevant with the onset of instability. Similar to the observations for the static pressure, the standard deviation increases significantly from stable to unstable conditions.

Figure 5.13 shows the time-averaged cavitation volume in the draft tube cone for stable (top) and unstable conditions (bottom). For the visualization, isosurfaces of the vapor volume fraction at 0.05 and 0.5 are displayed. All results have in common that an axisymmetric vortex rope develops that shows a shape with standing waves. For stable conditions, it can be observed that length and diameter of the cavitation volume increase with decreasing cavitation number. Furthermore, over a wide extension of the vortex rope, the cavitation volume built with the isosurface at threshold 0.5 is only slightly smaller compared to threshold 0.05. This indicates that for the

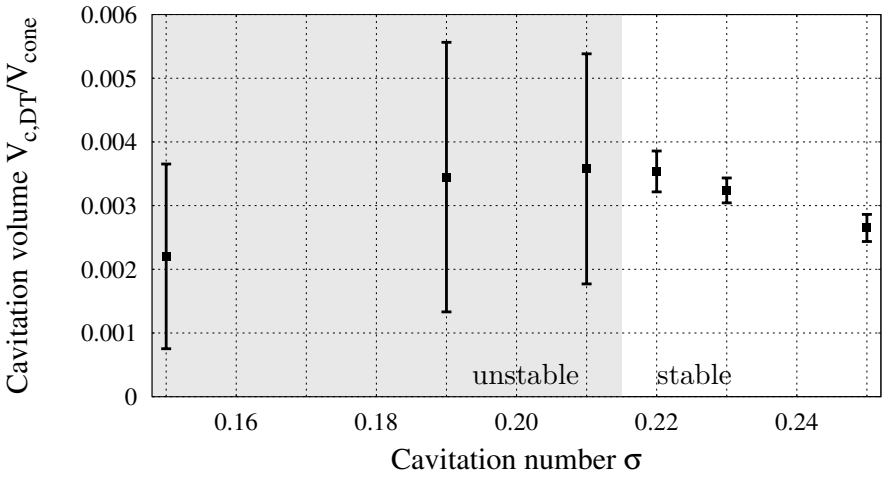

Figure 5.12: Time-averaged cavitation volume in the draft tube and standard deviation for different cavitation numbers.

investigated operating point a strong stable cavitating vortex forms with a distinct interface between liquid and vapor phase.

Contrary to this, the results for unstable conditions ($\sigma \leq 0.21$) show a different behavior. The cavitation volume built with the isosurface at threshold 0.5 reduces with decreasing cavitation number. Regarding threshold 0.05, the cavitation volume increases in length and diameter from $\sigma = 0.21$ to 0.19 but decreases significantly for $\sigma = 0.15$. Furthermore, the results for unstable conditions show that the difference between the cavitation volume built with the isosurface at threshold 0.5 is significantly smaller compared to threshold 0.05, which is different compared to stable conditions. This is a result of significantly bigger oscillations of the cavitation volume that are characteristic for the full load instability.

Next, the time-averaged cavitation volume in the runner is investigated. Figure 5.14 shows that only a small region of blade cavitation is forming in the runner for $\sigma = 0.23$ and 0.25. It is located near the trailing edge close to the shroud. Additionally, a small cavitation volume develops in the runner close to the trailing edge around midspan for $\sigma = 0.22$. When the cavitation number is further decreased, these two cavitation regions merge and form a cavity of relevant size. It is conspicuous that this occurs with the onset of the instability. This gives a first indication that the simulation results verify the findings from Müller [121] that cavitation in the runner plays a key role for the development of the full load instability. Furthermore, it can be observed that contrary to the observations for the vapor volume in the draft tube, the time-averaged

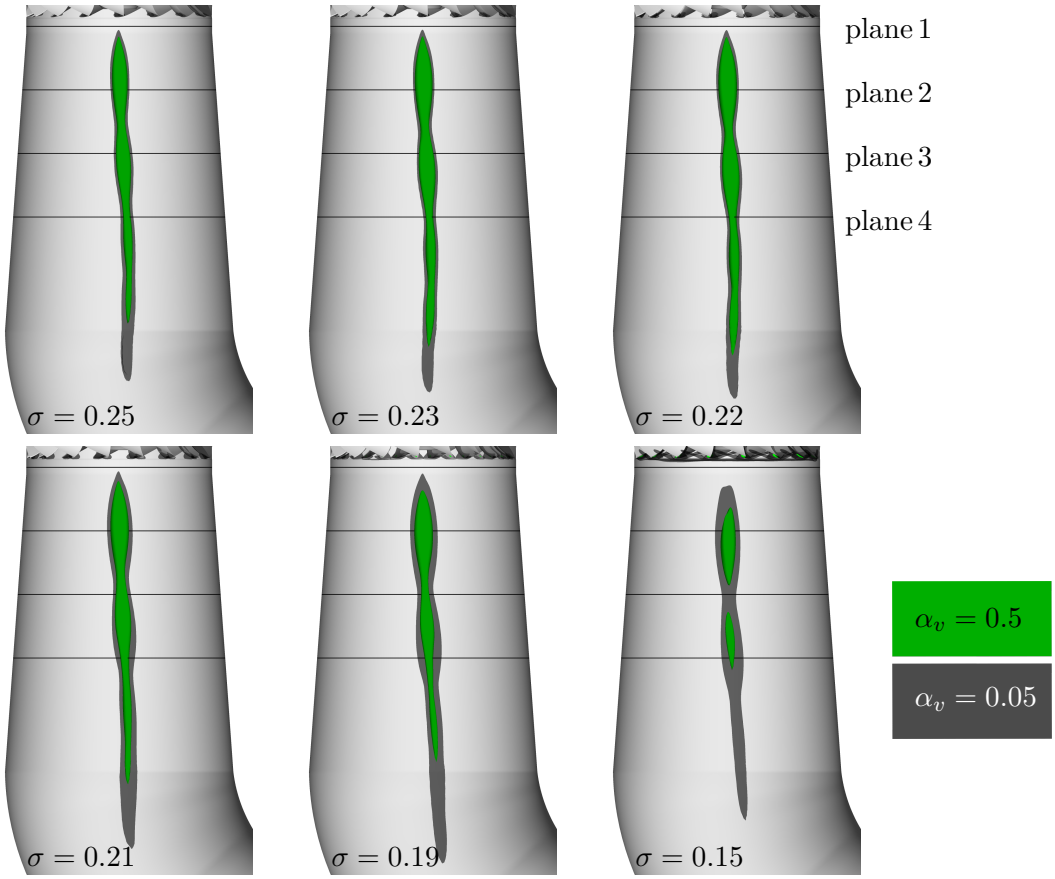

Figure 5.13: Visualization of the cavitation volume in the draft tube with two isosurfaces of the vapor volume fraction. Results are time-averaged. The lines represent the location of evaluation planes 1 to 4. Top: Stable conditions. Bottom: Unstable conditions.

cavitation volume in the runner increases with decreasing pressure level independent of the instability onset.

Müller stated a connection between the occurrence of blade cavitation and a modification of swirl number S and relative flow angle β, which is investigated in the following. In figure 5.15, the time-averaged swirl number for all evaluation planes and the cavitation volume in the runner are displayed for different cavitation numbers. The cavitation volume in the runner increases with decreasing σ and thereby follows roughly a parabolic shape regardless of instability onset. For stable conditions, the size of cavitation volume in the runner is small and the highest swirl number can be observed for all planes. While for plane 1 and 2, a slight decrease in swirl number can already be observed with decreasing σ, in plane 3 and 4 the swirl number remains constant for stable conditions. Nevertheless, it can be stated that with increasing blade cavitation the swirl number decreases. Consequently, a clear link between blade

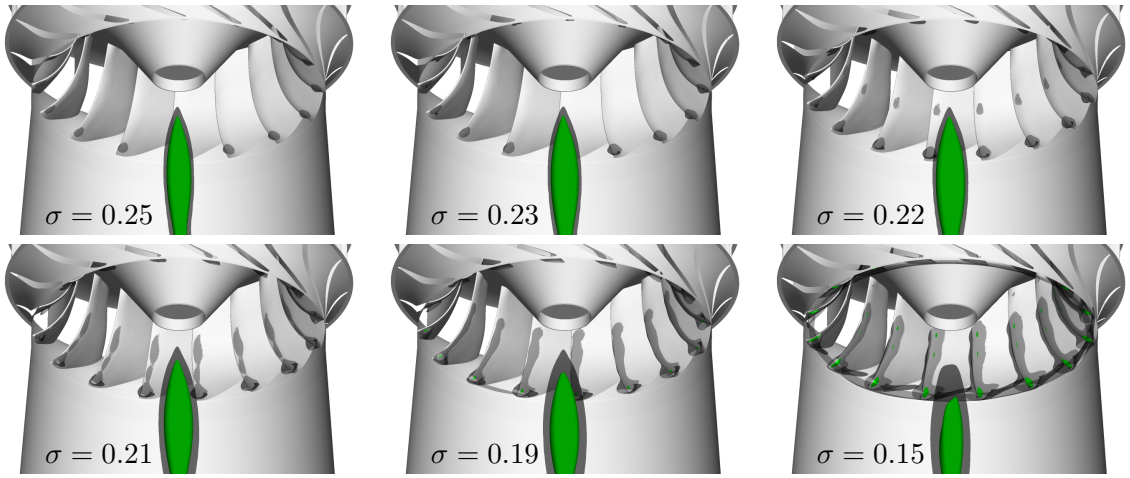

Figure 5.14: Visualization of the cavitation volume in the runner and upper draft tube with two isosurfaces of the vapor volume fraction (green: $\alpha_v = 0.5$ - dark grey: $\alpha_v = 0.05$). Results are time-averaged. Top: Stable conditions. Bottom: Unstable conditions.

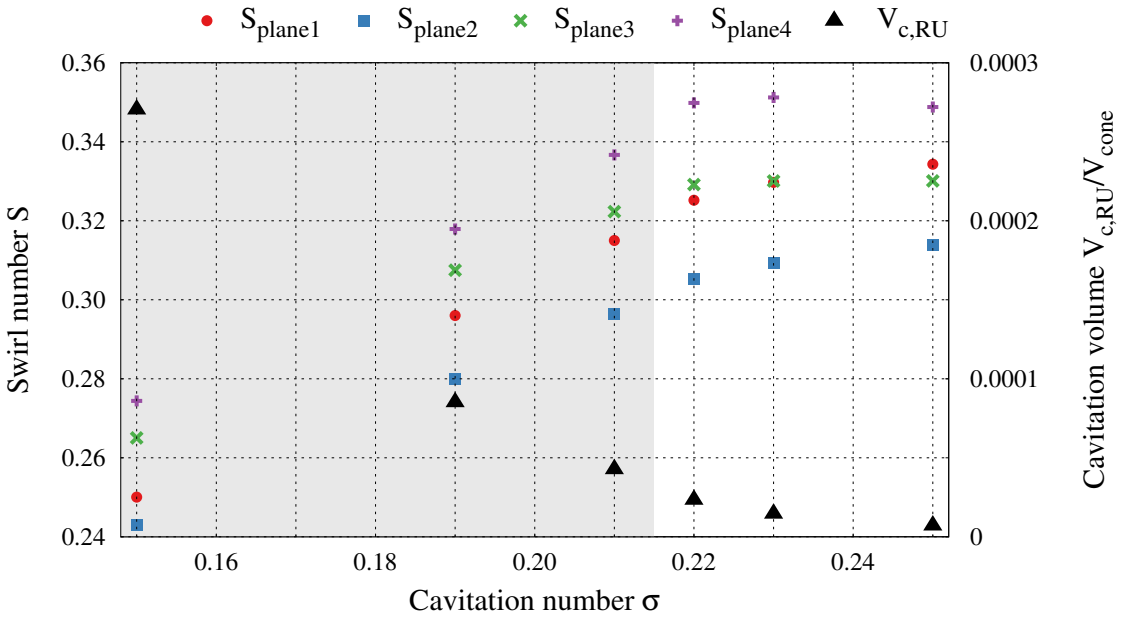

Figure 5.15: Time-averaged swirl number and cavitation volume in the runner for different cavitation numbers.

cavitation and the swirl number in all planes can be stated. At the onset of instability ($\sigma = 0.21$) the swirl number in plane 1 is approximately 6% below the value for the simulation with $\sigma = 0.25$.

The connection between the swirl number and the occurrence of blade cavitation can be explained by velocity triangles at the runner exit that are presented in figure 5.16.

For non-cavitating conditions, the relative flow angle β is equal to the blade angle at the runner outlet when effects due to a reduced deflection are neglected. At full load conditions, a typical velocity profile as presented on the left in figure 5.16 is present. The circumferential component of the absolute velocity c_u shows in the opposite direction than the peripheral speed u, which is the cause of the counter-rotating vortex rope at full load.

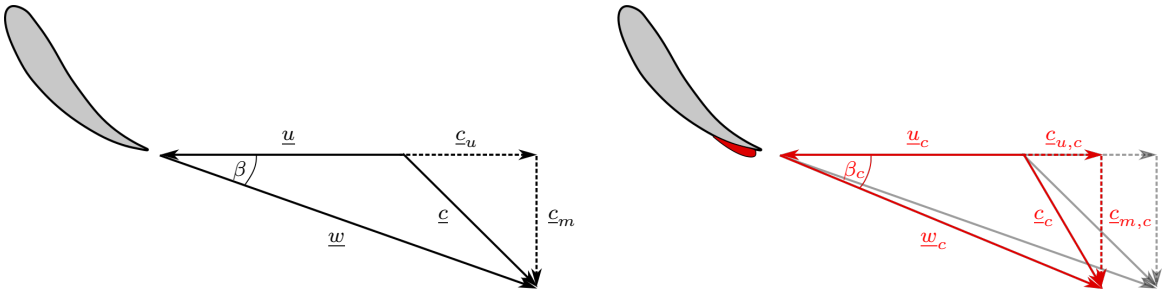

Figure 5.16: Velocity triangles for full load operating point. Left: Non-cavitating conditions. Right: Cavitating conditions.

Due to the occurrence of blade cavitation (see figure 5.16 right), the flow is slightly deflected at the runner exit, which results in an increased relative flow angle compared to non-cavitating conditions: $\beta_c > \beta$. If the blade cavitation is not oscillating, or the mass transfer is small compared to the discharge through the turbine, the meridional component of the absolute velocity remains constant: $c_{m,c} = c_m$. As a consequence c_u decreases: $c_{u,c} < c_u$. This results in the reduction of swirl number that has already been pointed out in figure 5.15:

$$S = \frac{G_{ang}}{G_{ax}} = \frac{\int_0^R r^2 c_u c_m \,\mathrm{d}r}{R_{\bar{1}} \int_0^R r c_m^2 \,\mathrm{d}r} > \frac{\int_0^R r^2 c_{u,c} c_{m,c} \,\mathrm{d}r}{R_{\bar{1}} \int_0^R r c_{m,c}^2 \,\mathrm{d}r} = S_c \tag{5.1}$$

A reduction of swirl results in a weaker vortex and consequently a smaller cavitation volume in the draft tube can be expected, which is called effect 2 in the following. This is the mechanism that acts opposite to the effect of cavitation volume increase caused by pressure reduction (effect 1) and explains why a decreased cavitation number does not necessarily lead to an increase of draft tube cavitation volume (see figure 5.12).

A closer look at figure 5.15 shows two correlations that are intuitively difficult to understand. First, from plane 1 to 2 the swirl decreases while otherwise the swirl is higher for the plane that is located further downstream. Secondly, the trend that the swirl increases from plane 2 to 4 creates the impression that conservation of angular

momentum is violated. To get a better understanding of these correlations, axial flux of angular momentum G_{ang} and axial flux of axial momentum G_{ax}, which correspond to numerator and denominator for the calculation of the swirl number, are presented in figure 5.17.

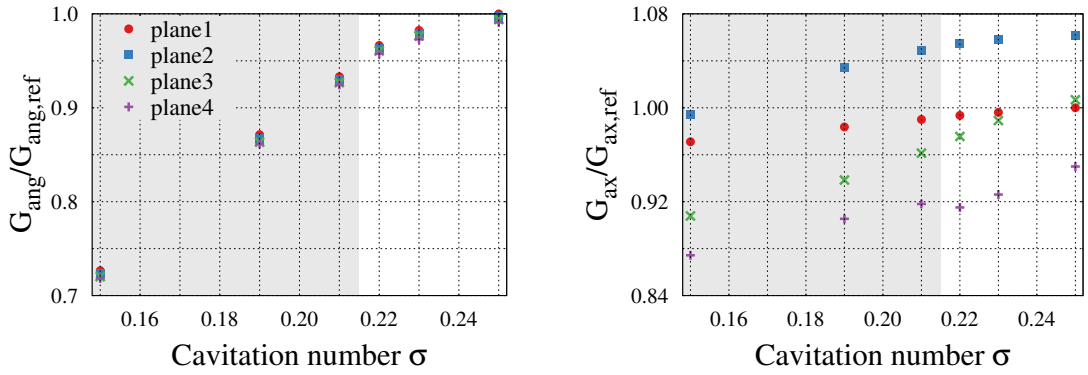

Figure 5.17: Time-averaged axial flux of the angular momentum G_{ang} (left) and axial flux of the axial momentum G_{ax} (right) for different cavitation numbers in the evaluation planes. The value of plane 1 at $\sigma = 0.25$ is used as reference for both diagrams.

It can be observed that G_{ang} decreases with decreasing cavitation number in a similar parabolic shape as it can be found for the swirl number. This indicates that the main shape of the swirl number over cavitation number results from the variation of G_{ang}. Furthermore, it can be found that for a specific cavitation number G_{ang} is almost equal for all planes with a slight trend that G_{ang} decreases from plane 1 to 4. This is probably caused by the slight decrease of axial velocity that is a result of the widening of the draft tube cone. Consequently, angular momentum is not violated.

The axial flux of axial momentum G_{ax} also slightly decreases with decreasing cavitation number. However, this trend is less pronounced compared to G_{ang}. A comparison of the different planes shows that the unexpected behavior of plane 1 is a result of G_{ax}. From plane 2 to 4 it decreases mainly caused by the widening of the draft tube cone, which finally results in the fact that swirl number increases (see figure 5.15 for comparison). Contrary to this, plane 1 has a lower G_{ax} compared to plane 2, which also explains the unexpected behavior in the swirl number. The reason for the different behavior of plane 1 can be found in the differences of the velocity profiles for the different planes that are displayed in the upper part of figure 5.18.

It can be clearly observed that the axial velocity for line 1 behaves different in the center of the draft tube compared to the other lines. This can be explained by the

fact that line 1 is located only a small distance below the runner nut, which effects the axial velocity distribution and consequently results in a different behavior of G_{ax} and swirl number. In the outer part of the draft tube, the trend can be found that axial velocity decreases from line 1 to 4, which is caused by the widening of the cone. For circumferential velocity distribution all lines show a similar behavior. Close to the draft tube wall it can be observed that an uneven velocity distribution evens out with increasing distance to the runner. Furthermore, for line 3 and even more for line 4 the zero crossing of circumferential velocity is not in the center anymore, which is a result of the elbow.

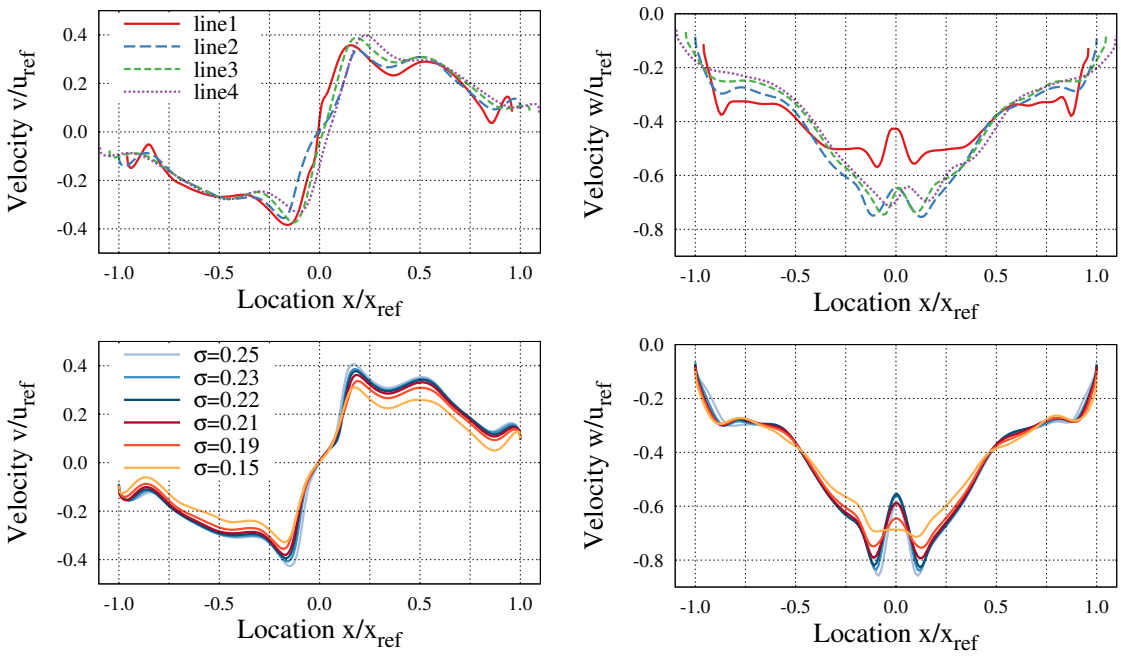

Figure 5.18: Time-averaged circumferential (left) and axial (right) velocity distribution in draft tube cone. The reference length x_{ref} corresponds to the radius of the draft tube cone at the location of line 2. Top: Along lines for $\sigma = 0.19$. Bottom: Along line 2 for different cavitation numbers.

The influence of cavitation number on axial and circumferential velocity distribution is presented in the lower part of figure 5.18 for line 2. It can be observed that the circumferential velocity decreases with a reduction of cavitation number. This is in good agreement to the findings from above that with increased cavitation volume c_u decreases. It has to be mentioned that the identified correlation is independent of the instability onset.

The biggest influence of cavitation number on the axial velocity distribution can be found in the center of the draft tube ($|x/x_{ref}| < 0.35$). There, axial velocity decreases

with decreasing σ, which highlights that the size of cavitation volume has a significant impact on this velocity component. In the outer part of the draft tube ($|x/x_{ref}| > 0.5$), minor differences in the axial velocity distribution can be found. For example, there can be observed that the gradient close to the wall increases with decreasing cavitation number. Again, the identified correlations are independent of the instability onset.

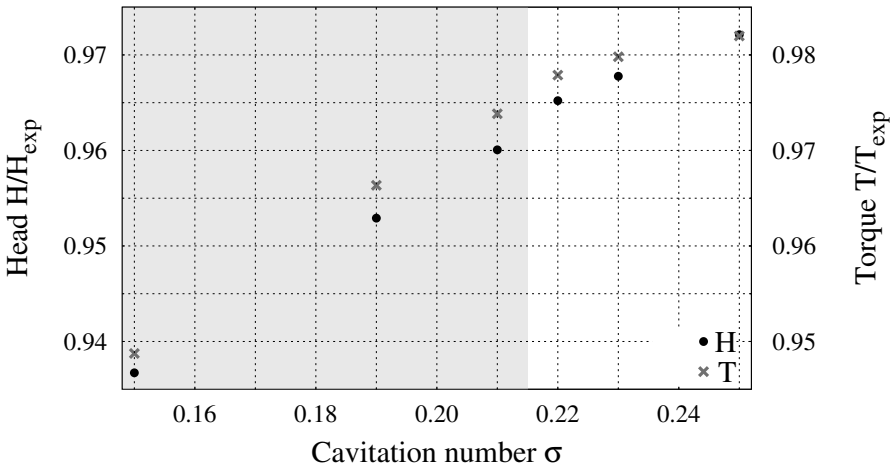

Figure 5.19: Time-averaged head and torque for different cavitation numbers.

Finally, the quantities head and torque are investigated (see figure 5.19). Both, head and torque, are made dimensionless with experimental results that are available for $\sigma = 0.20$. It has to be pointed out that at this cavitation number the measurement shows stable behavior, while the simulation would already be in the unstable regime. The simulation results show that head and torque decrease with a reduction of cavitation number. For torque this can be explained with the occurrence of blade cavitation on the suction side of the runner. The pressure reduction is limited by cavitation, which limits the pressure difference between pressure and suction side compared to non-cavitating conditions. Investigations of a part load operating point on a pump turbine at model scale that were performed by Kirschner [91] show the same behavior for head. For torque he did not observe a reduction for decreased cavitation number. This can be probably explained with non-existent blade cavitation in the runner.

The simulation results show that head is underestimated for all cavitation numbers. This comes across with a shifted operating point, which is displayed in figure 5.20. Due to the underestimation of head, the operating point is shifted to higher Q_{ED} and n_{ED}. Furthermore, this shift increases with decreasing cavitation number and results in an increased distance of the operating point to the rope free zone, which is located between the dashed lines. While the general underestimation of head is caused by

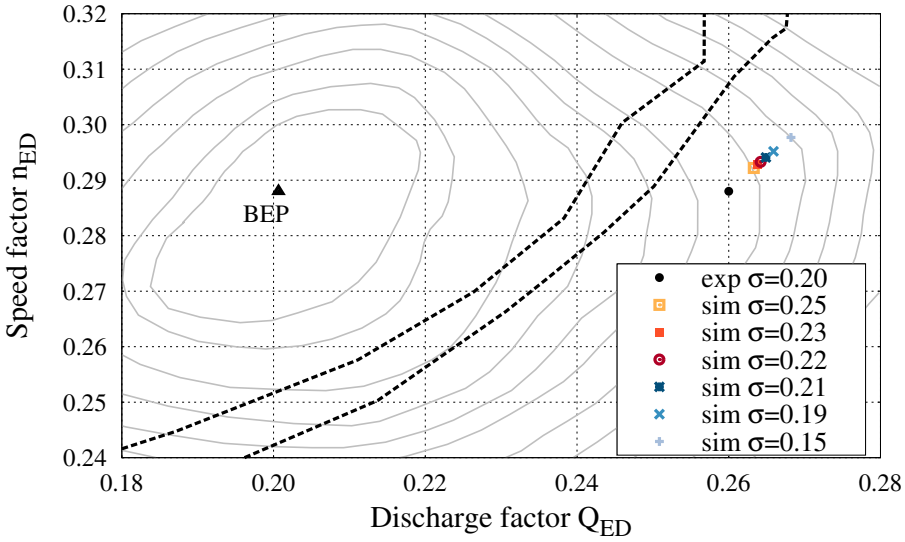

Figure 5.20: Detail from the hill chart with marked position of the simulated operating point. Rope free zone is marked by dashed lines.

simulation inaccuracies, the shift within the simulation results is of physical nature and can also be found in experiments (see e.g. [91]).

Comparison of Mesh 14M and 48M

So far, all presented results within this section originate from simulations with mesh 14M. In this subsection, comparisons are made to simulation results with mesh 48M to investigate the impact of mesh resolution. Simulation results with the fine mesh are available for the cavitation numbers 0.19, 0.22 and 0.25. The results for time-averaged cavitation volume in the draft tube for different cavitation numbers is displayed in figure 5.21. A general trend can be observed that the average cavitation volume in the draft tube is smaller for simulations with the finer mesh.

In the stable regime, the results from simulations with the fine mesh are in agreement with the findings from the coarse mesh that cavitation volume increases with decreasing cavitation number. Furthermore, the standard deviation is moderate and of comparable size for both meshes. At $\sigma = 0.19$, unstable conditions can be identified for both mesh sizes. Standard deviation is slightly smaller for mesh 48M, which is probably a result of the smaller averaged cavitation volume in the draft tube as this is a limiting factor for the amplitude of the oscillations.

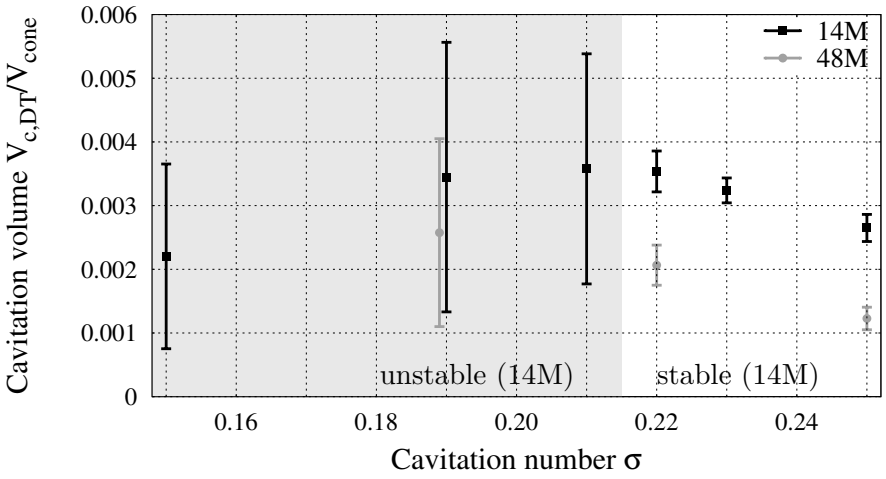

Figure 5.21: Time-averaged cavitation volume in the draft tube and standard deviation for different cavitation numbers. For better clarity the cavitation number for mesh 48M and $\sigma = 0.19$ is slighty shifted in the diagram.

Due to the smaller amount of simulated cavitation numbers for the finer mesh, the onset of the instability can be predicted less precise. While for the coarse mesh the onset can be identified to be in the range $0.21 < \sigma < 0.22$, for mesh 48M it is in the range $0.19 < \sigma < 0.22$. Consequently, the grey shaded region in figure 5.21 marks the unstable region for mesh 14M. For the coarse mesh it was identified that with the onset of the instability the average cavitation volume in the draft tube does not increase anymore. If these findings can be transferred to the fine mesh, it can be expected that the instability onset is at slightly lower cavitation number for mesh 48M. However, it is still higher compared to experimental observations that were already shown in section 5.1.

In figure 5.22, the cavitation volume that forms on the runner blades is visualized for both mesh sizes at three different cavitation numbers. Generally, the tendency can be noticed that a smaller cavitation volume in the runner is present for the finer mesh. For the coarse mesh it has been identified that the onset of the instability is linked to the occurrence of a cavitation region at the runner trailing edge that ranges approximately from midspan to the shroud. This correlation can also be found for the fine mesh, as the characteristic cavitation region at the runner trailing edge can only be found for $\sigma = 0.19$. Furthermore, the cavitation volume in the runner is also smaller for the finer mesh, which supports the presumption that with mesh 48M the instability onset is shifted to a slightly lower cavitation number.

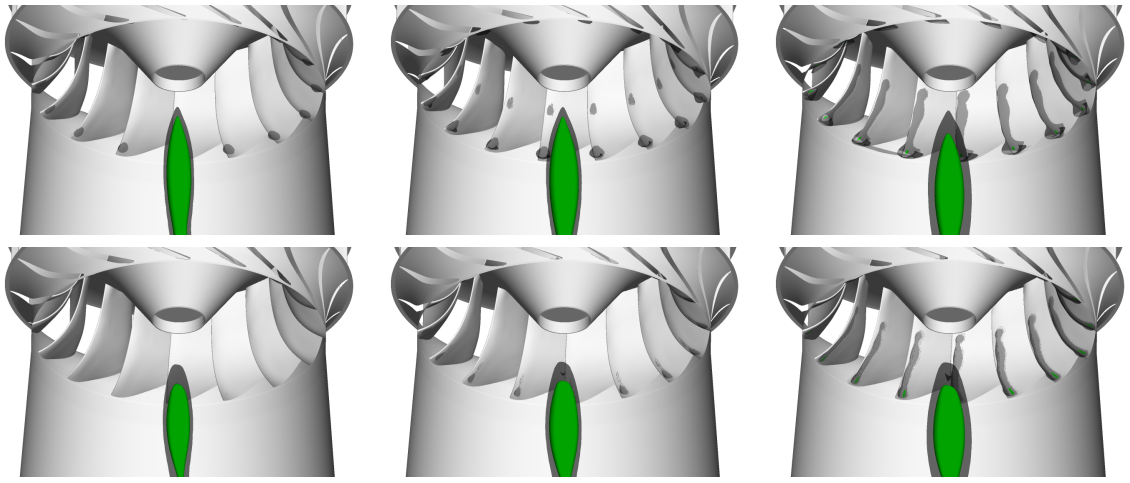

Figure 5.22: Visualization of the cavitation volume in the runner and upper draft tube with two isosurfaces of the vapor volume fraction (green: $\alpha_v = 0.5$ - dark grey: $\alpha_v = 0.05$). Results are time-averaged. Top: Mesh 14M. Bottom: Mesh 48M.

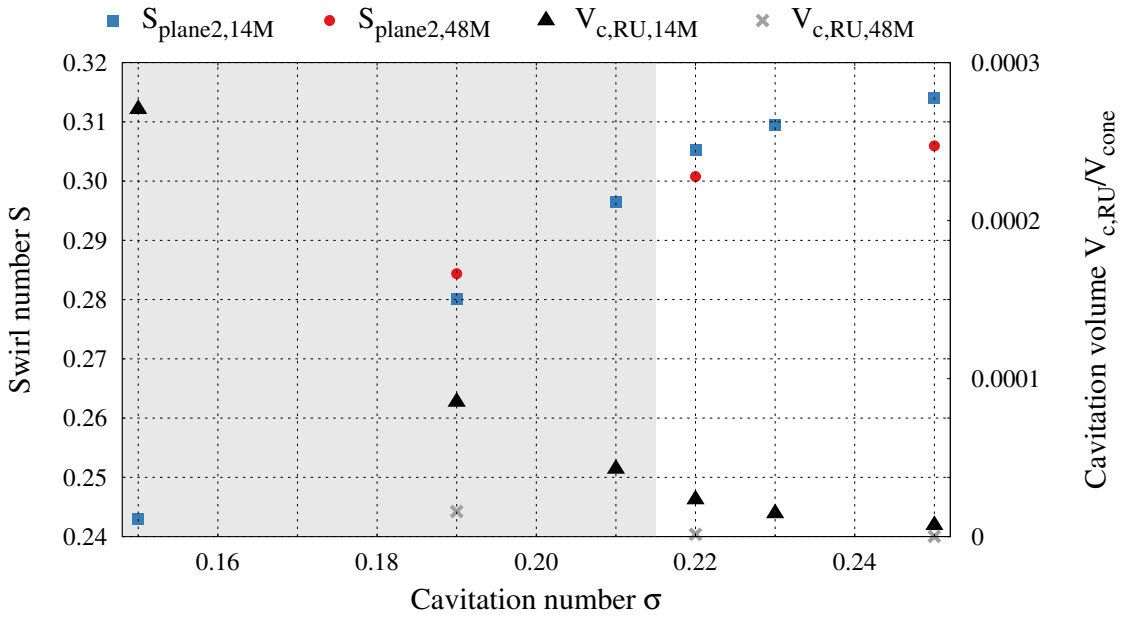

Figure 5.23: Time-averaged swirl number in plane 2 and cavitation volume in the runner for different cavitation numbers.

In figure 5.23, swirl number in plane 2 and cavitation volume in the runner are plotted for different cavitation numbers. As already identified in figure 5.22, the cavitation volume in the runner is smaller for the finer mesh. Furthermore, it is conspicuous that for mesh 48M the instability onset occurs at a size of cavitation volume in the runner where the coarse mesh is still stable. This can be explained by the formation

of a bigger cavitation volume close to the shroud for mesh 14M that, however, does not cause the instability. It is rather linked to the connected cavitation region from midspan to the shroud, as described above.

The link between swirl number and the occurrence of cavitation in the runner can also be found for the finer mesh. For $\sigma = 0.25$ the swirl number in plane 2 is slightly higher for the coarser mesh. Due to the negligible cavitation volume in the runner for this cavitation number, this difference is a result of differences in the velocity distribution that are caused by a different mesh resolution. With a reduction of cavitation number, both meshes show the trend of decreasing swirl number. Thereby, swirl number of the finer mesh decreases more slowly, which can be explained by the shifted instability onset that has been explained more detailed above.

All in all, it can be stated that the findings that were derived for the coarse mesh can also be transferred to the fine mesh. This indicates that the identified correlations are mesh independent. For the following, detailed investigations are carried out with the coarse mesh due to the lower computational effort.

5.2.2 Unsteady Behavior Caused by Full Load Instability

After analyzing time-averaged quantities in the previous part, this subsection investigates the unsteady behavior that is caused by the full load instability. While for some results the variations are presented over time, most results at unstable conditions are shown mean phase averaged according to the descriptions from section 5.1.2.

Plotting the pressure at location C1N as function of time (see figure 5.24) shows a significant increase of the amplitude of pressure oscillations from stable to unstable conditions. For stable conditions, all presented σ-levels show a similar behavior with the occurrence of only small pressure fluctuations. However, this changes when the pressure level is only slightly decreased from $\sigma = 0.22$ to 0.21. The result is that the amplitude of the pressure oscillation increases significantly. This highlights that the instability onset is somewhere between a cavitation number of 0.21 and 0.22 for the used simulation setup. A comparison to measurement results (see figure 5.2) shows that the onset of instability is at higher σ in the simulation. This is probably a result of simulation inaccuracies and might be traced back to the shifted operating point as shown in figure 5.20.

Within unstable conditions, differences for the investigated cavitation numbers can be observed. The occurring pressure peak strongly depends on σ. For the investigated

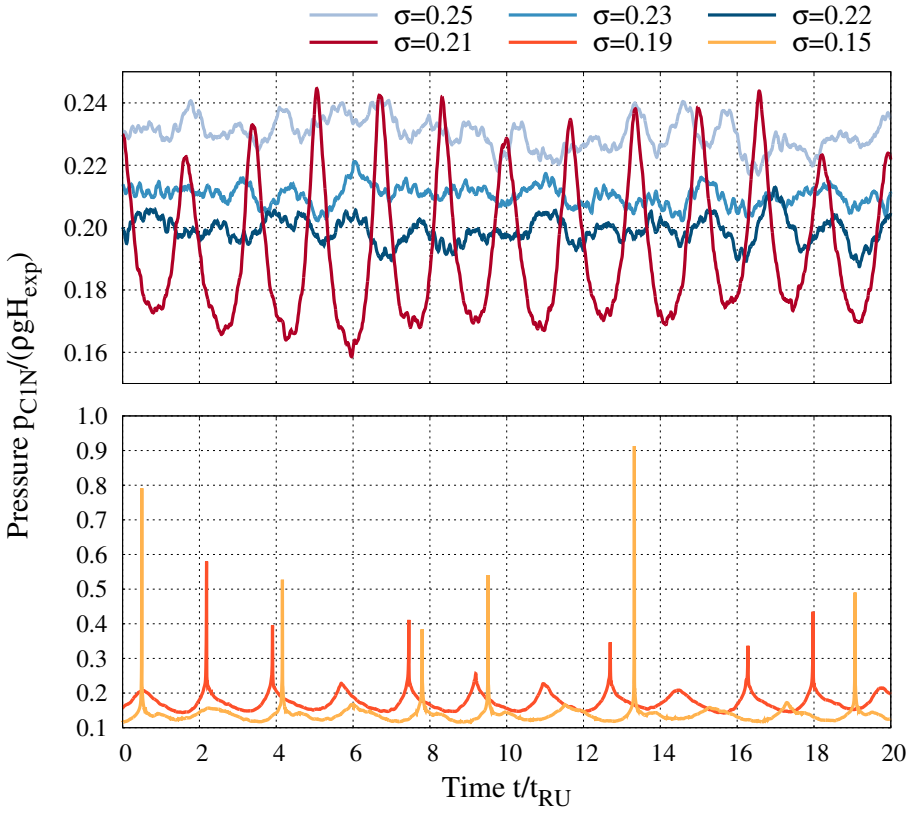

Figure 5.24: Static pressure at location C1N for different cavitation numbers as function of runner revolutions.

pressure levels the trend is that the pressure peak increases with decreasing cavitation number. Furthermore, a reduction of σ leads to a reduced frequency of the oscillation, which can also be seen in measurements.

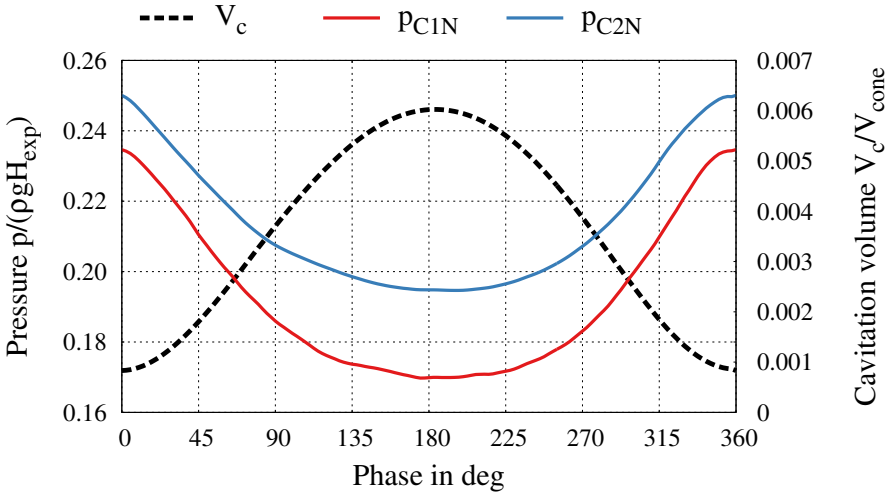

Figure 5.25: Mean phase averaged static pressure at locations C1N and C2N and cavitation volume in the simulation domain for $\sigma = 0.21$.

In figure 5.25, the mean phase averaged static pressure at measurement locations C1N and C2N is displayed for $\sigma = 0.21$. At location C2N the static pressure is higher, which can be explained by the position further downstream in the draft tube cone, where the cross-sectional area is bigger. A comparison of the two curves indicates that there is no phase shift between location C1N and C2N, which has also been observed in measurements [121, 124]. This is due to the fact that pressure propagates with speed of sound, which is infinite for incompressible simulations. Besides the severe pressure oscillation, the full load instability is accompanied by a strong oscillation of cavitation volume in runner and draft tube. A comparison between the total cavitation volume that occurs within the simulation domain and pressure shows that the pressure peak coincides with the minimum cavitation volume. Additionally, pressure minimum coincides with cavitation volume maximum.

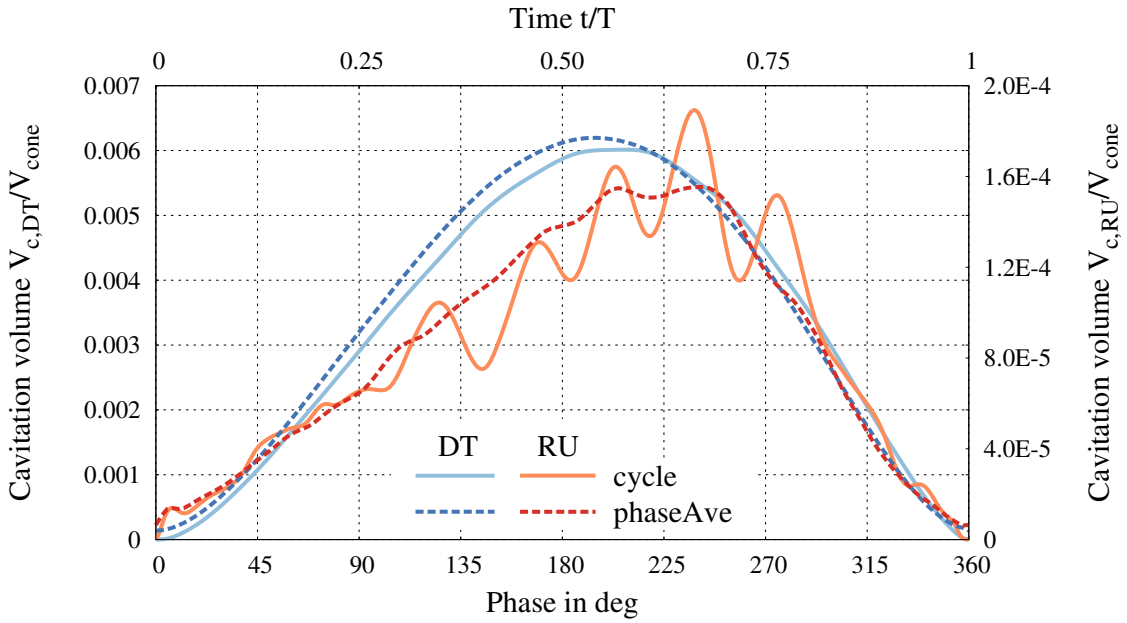

Figure 5.26: Cavitation volume in draft tube and runner as function of phase angle. For both quantities the mean phase averaged result and the result of one representative cycle are presented.

The course of phase averaged cavitation volume in runner and draft tube over phase are displayed in figure 5.26 exemplarily for $\sigma = 0.19$. Additionally, $V_{c,RU}$ and $V_{c,DT}$ are plotted over time for one representative cycle. While in the draft tube, the mean phase averaged results have approximately a sine shape, the runner behaves slightly different. In the draft tube, minimum cavitation volume occurs at phase 0° and maximum shortly after 180°. While the minimum cavitation volume in the runner also occurs

at phase 0°, the maximum appears around 45° delayed compared to the draft tube. This results in a slower increase of cavitation volume in the runner, while the re-condensation is faster compared to the draft tube.

The maximum cavitation volume in the draft tube from the reference cycle occurs slightly after the mean phase averaged result. This indicates that the occurrence of cavitation volume maximum can slightly vary between different instability cycles. Nevertheless, the shape of the cavitation volume oscillation in the draft tube is similar between the representative cycle and the mean phase averaged results. Contrary to this, the time course of $V_{c,RU}$ shows oscillations within the representative cycle that are cancelled out in the mean phase averaged results. In the following, snapshots at different times of the representative cycle are presented.

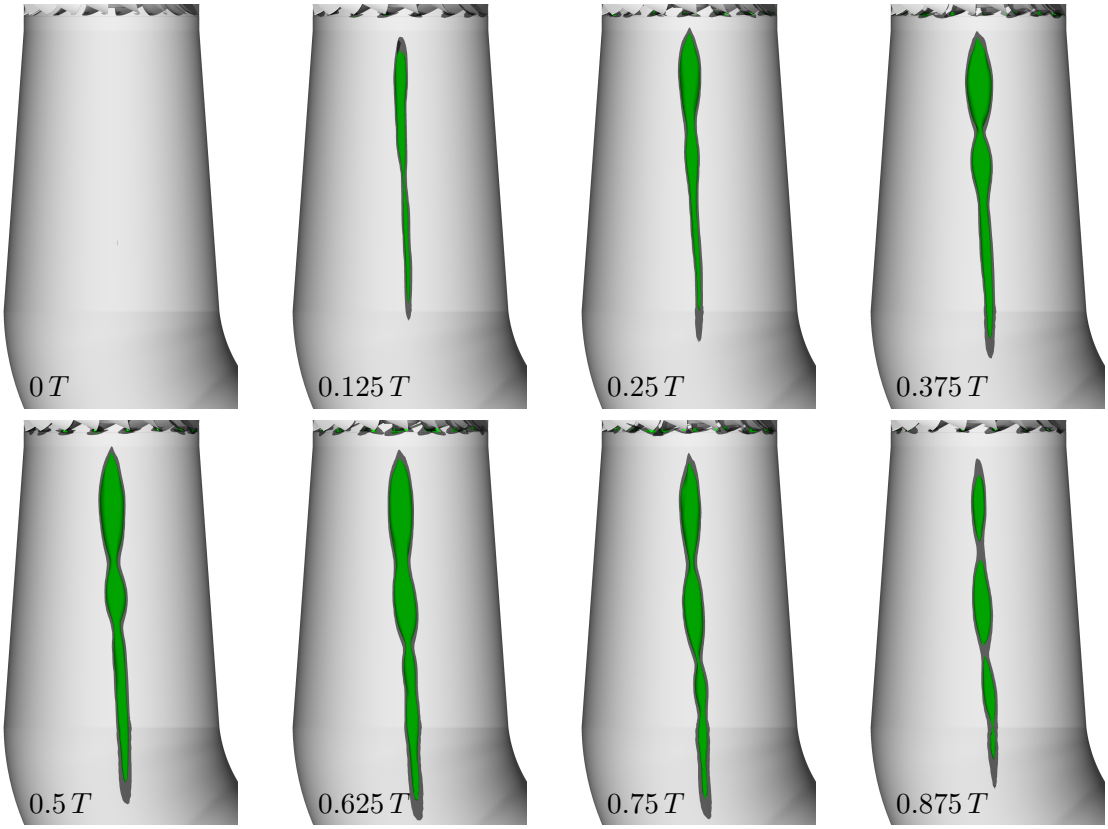

Figure 5.27: Visualization of the cavitation volume in the draft tube with two isosurfaces of the vapor volume fraction (green: $\alpha_v = 0.5$ - dark grey: $\alpha_v = 0.05$) at different times of one instability cycle at $\sigma = 0.19$.

The oscillation of the cavitating draft tube vortex rope is visualized in figure 5.27 for one instability cycle at $\sigma = 0.19$. At the beginning, the vortex rope is not cavitating. This phase coincides with the severe pressure peaks that can be seen in figure 5.24.

Thereafter, the cavitation volume increases and reaches its maximum shortly after half of the period duration T. After that, the cavitation volume decreases. It has to be highlighted that even though mean phase averaged results show approximately a sine shape, this is not necessarily the case for one instability cycle. For the presented cycle, it can be clearly observed that the oscillation is not symmetric as this would result for example in a similar cavitation volume for the times $0.125\,T$ and $0.875\,T$, which is obviously not the case.

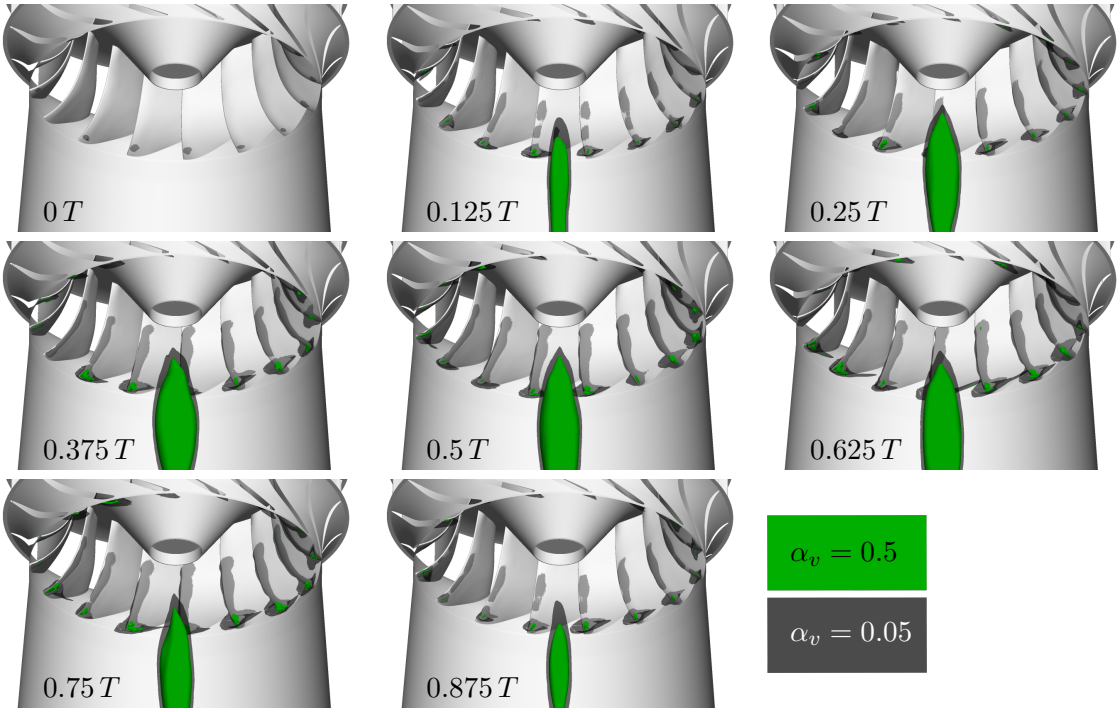

Figure 5.28: Visualization of the cavitation volume in the runner and upper draft tube with two isosurfaces of the vapor volume fraction at different times of one instability cycle at $\sigma = 0.19$.

In figure 5.28, the cavitation volume in the runner is shown at different instants of one instability cycle. At the beginning of the cycle, only a small vapor region is present near the shroud close to the trailing edge. Afterwards, the cavitation volume increases until, at maximum size, the cavity extends approximately from span 0.4 to 1. Qualitatively, this extension agrees well with experimental observations at $\sigma = 0.11$ from Müller [121].

As already pointed out in figure 5.16, the occurrence of blade cavitation has an impact on the relative flow angle β. In figure 5.29, the temporal progression of β and local cavitation volume within the related averaging ribbon is displayed exemplarily for $\sigma = 0.19$ and 0.25 at location DTin08. For a better clarity the moving average of β is

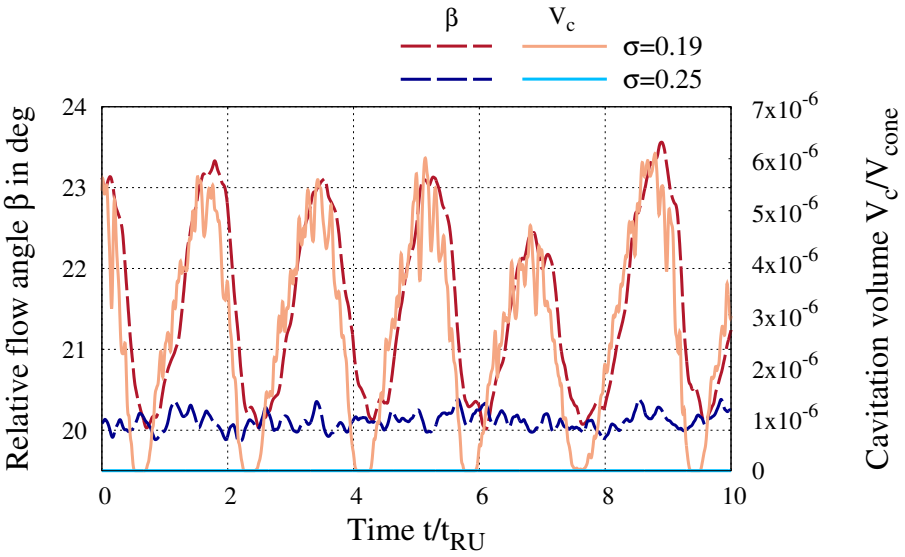

Figure 5.29: Moving average of relative flow angle at location DTin08 and related cavitation volume within the averaging ribbon.

displayed. For $\sigma = 0.25$, no blade cavitation occurs in the related averaging ribbon. The small scale variations of the relative flow angle are below 0.5° and are a result of velocity fluctuations that among other things result from rotor stator interaction. Contrary to this, the volume of blade cavitation is facing an oscillation for the unstable conditions at $\sigma = 0.19$. This oscillation is also present in the relative flow angle, which states a clear link between these quantities. A small time delay between the two oscillations is present. It can be traced back to the time that is needed for the velocity variations to travel from the region of blade cavitation to location DTin08, which is located slightly downstream of the runner trailing edge.

The link between the occurrence of blade cavitation and β that has been shown by means of velocity triangles at the runner exit (see figure 5.16) is clearly confirmed. At the moments when no blade cavitation occurs, for both cavitation numbers the relative flow angle is around 20°. For $\sigma = 0.19$ the increase of blade cavitation comes across with increased β.

For unstable conditions, the swirl number and cavitation volume in the runner show significant oscillations. In figure 5.30, this is exemplarily displayed for $\sigma = 0.19$. The mean phase averaged results show that the maximum cavitation volume in the runner occurs around the phase 225° and the minimum at 0°. Previous findings stated that for huge cavitation volumes in the runner, a small swirl number can be expected and vice versa. This correlation is well met for the swirl at evaluation plane 1. There, only

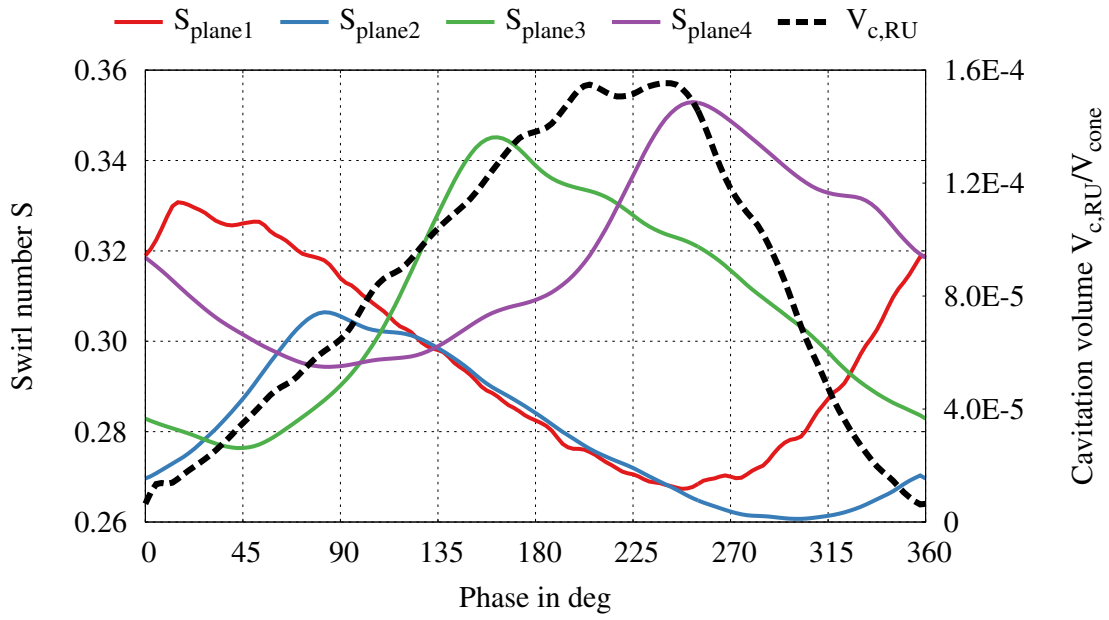

Figure 5.30: Mean phase averaged swirl number at different evaluation planes and cavitation volume in the runner for $\sigma = 0.19$.

a small phase shift of 15° is present that can be explained by the short distance that the swirl change has to travel from the runner exit to plane 1.

Table 5.2: Phase shift and swirl transport velocity in the draft tube for $\sigma = 0.19$. Phase shift is specified as the difference between minimum of cavitation volume in runner and maximum of swirl in the plane.

Plane	1	Δ_{1-2}	2	Δ_{2-3}	3	Δ_{3-4}	4
Phase shift in deg	15		82.5		162.5		252.5
Δ phase shift in deg		67.5		80		90	
Swirl transport velocity $v_S/\overline{w}$		0.94		0.86		0.85	

For the other planes, significantly higher phase shifts can be determined (see table 5.2). This strongly indicates that the swirl is transported with the flow, as the phase shift increases with the distance to the runner exit. For table 5.2, the phase shift is determined from the difference between minimum of cavitation volume in runner and maximum of swirl in the plane. It can be observed that the time needed for the swirl to travel from one evaluation plane to the next increases with the distance to the runner exit. This can be explained by the draft tube cone, which has the effect that the transport velocity decreases. While from plane 1 to 2 the swirl change travels 67.5° in terms of phase, it increases up to 90° from plane 3 to 4.

A comparison of the swirl transport velocity v_S, which can be determined from the phase shift between two planes, to the averaged axial velocity $\overline{w}$ is presented in table 5.2. Therein, $\overline{w}$ is calculated as follows:

$$\overline{w}_{1-2} = \frac{w_{areaAve,plane1} + w_{areaAve,plane2}}{2} \tag{5.2}$$

Equation 5.2 is exemplarily for the calculation of the swirl change from plane 1 to 2. It can be applied analog for the other planes. For all locations, the results show that the swirl transport velocity is slightly below related averaged axial velocity. The maximum difference can be found from plane 3 to 4 and is 15%. The difference between v_S and $\overline{w}$ can be explained by the reduction of axial velocity to one single averaged value. As already seen in figure 5.18, axial velocity strongly depends on the radial position within one evaluation plane. Therefore, it is not surprising that some deviation between v_S and $\overline{w}$ can be observed. However, the reasonable agreement supports the statement that in the draft tube swirl changes are transported with the axial velocity.

Due to the swirl variation during one instability cycle, it can be expected that the velocity distribution shows some unsteady behavior during one cycle. The mean phase averaged results for circumferential and axial velocity at line 2 are presented in figure 5.31. The grey colored band highlights the variation of velocity within the mean phase averaged instability cycle. Furthermore, the velocity profile at phase 90° and 337.5° are displayed as they represent the limits of the oscillations quite well.

For circumferential velocity it can be observed that the width of the band is approximately constant over a wide range from $|x/x_{ref}| \approx 0.2$ to 0.95. This indicates that the variation of relative swirl angle caused by cavitation affects a wide range of the distribution of circumferential velocity. In this outer range maximum velocity occurs around a phase of 90° and minimum velocity at approximately 337.5°, which is in good agreement with the behavior of swirl number in plane 2 (see figure 5.30). The highest variations of circumferential velocity can be observed close to the center in the region of the interface between cavitating draft tube vortex and the surrounding fluid.

Contrary to this, axial velocity distribution shows a different behavior. In the range $|x/x_{ref}| > 0.5$, axial velocity oscillates only slightly during one instability cycle. The main variations of axial velocity can be found in the center of the draft tube. This can be explained by the oscillation of the cavitation volume. Due to continuity equa-

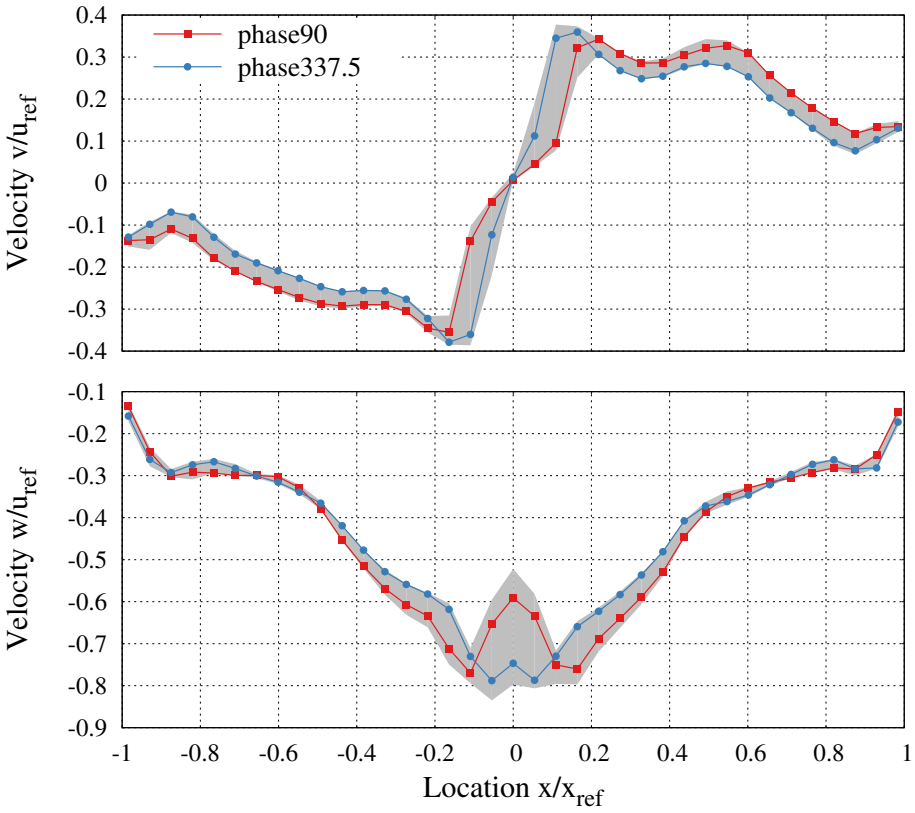

Figure 5.31: Mean phase averaged circumferential (top) and axial (bottom) velocity distribution along line 2 at $\sigma = 0.19$. The grey band highlights the velocity variation within the mean phase averaged instability cycle. The reference length x_{ref} corresponds to the radius of the draft tube cone at the location of line 2.

tion 2.9, axial velocity is directly affected by the mass transfer between liquid and vapor phase.

So far it has been shown that a reduction of the pressure level leads to two effects that work opposite to each other, which is shown schematically in figure 5.32. On the one hand, effect 1 represents that reducing the pressure level should lead to a bigger cavitation volume in the draft tube. This effect can be seen for stable conditions (see figure 5.12). On the other hand, a reduction of the cavitation number leads to an increased cavitation volume in the runner, which results in a decreased swirl number. A reduced swirl number comes along with a weaker vortex in the draft tube. For that reason a smaller cavitation volume of the vortex rope can be expected caused by effect 2.

In general, no statement can be made which of these two effects is dominant. Consequently, assuming stable conditions, a superposition of both effects can result in the

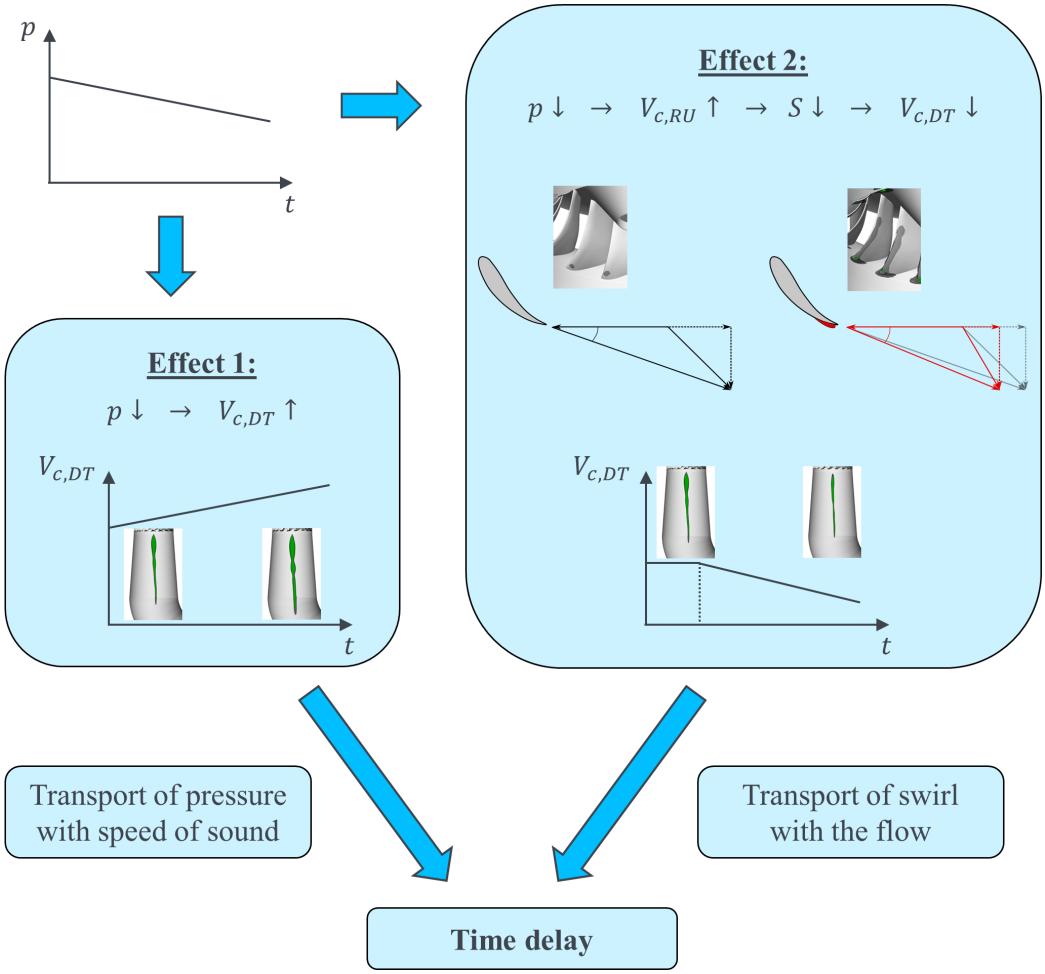

Figure 5.32: Schematic chart of the two counteracting effects that are caused by pressure reduction.

two different solutions. First, the cavitation volume of the vortex rope increases as the pressure reduction in the draft tube is dominant. Secondly, the cavitation volume of the vortex rope decreases as the swirl reduction dominates. A review of figures 5.12, 5.14 and 5.15 shows that effect 2 already dominates when a connected region of blade cavitation is forming close to the trailing edge. Even though at instability onset the cavitation volume in the runner is rather small, it is big enough that effect 2 becomes important.

All in all, the superposition of two counteracting effects does not inevitably result in the formation of an instability. It could also be possible that a new stable condition develops. A first indication what else is relevant for the development of the full load instability can be found in figure 5.30. The swirl reduction caused by the blade cavitation needs some time to travel into the draft tube, where it affects the cavita-

tion volume of the vortex rope. This is in agreement with the findings from Dörfler et al. [45] that are presented more detailed in section 2.5. On the other hand, the effect of increased cavitation volume of the vortex rope caused by pressure reduction acts instantaneously as the pressure propagates with speed of sound (see figure 5.25), which is infinite for incompressible simulations. Consequently, there is a time delay between these counteracting effects, which fits also to the theory on auto-oscillation from Jenkins [85] (see section 2.5).

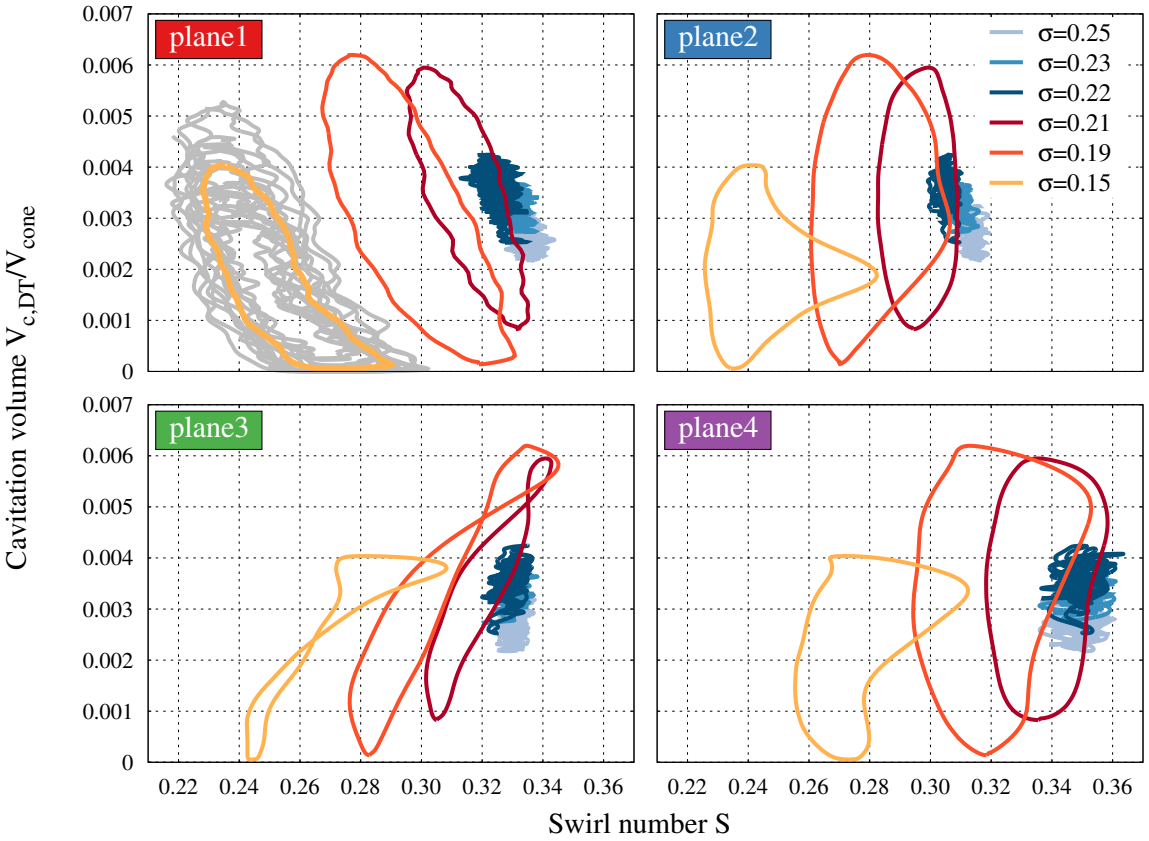

Figure 5.33: Cavitation volume in the draft tube as function of swirl number in the four evaluation planes for different cavitation numbers. The results for unstable conditions are presented mean phase averaged. Exemplarily, the full results of 12 instability cycles are displayed in plane 1 for $\sigma = 0.15$ (grey line).

In figure 5.33, the cavitation volume in the draft tube is displayed as function of swirl number for the different evaluation planes. The simulation results for stable conditions (shades of blue), show that within 20 runner revolutions the swirl number fluctuates only little and also the cavitation volume oscillates significantly less compared to unstable conditions (shades of red). For unstable conditions, swirl number and $V_{c,DT}$ vary a lot more. All simulation results for unstable conditions are presented mean phase averaged. Furthermore, the full results of 12 instability cycles are displayed

exemplarily in plane 1 for $\sigma = 0.15$ (grey line), which shows that there is a variation between individual cycles but in general all cycles show a similar behavior.

The above stated time delay can be determined by finding the representative location in the draft tube cone where the correlation is satisfied that the cavitation volume of the vortex rope increases with increasing swirl number. As shown in figure 5.33, this location can be found to coincide with reasonable agreement with plane 3 for all three unstable conditions. For all the other planes, the correlation is not fulfilled. Without applying any phase shift to the results, in plane 1 the results even show that $V_{c,DT}$ increases for decreasing swirl number. This would be contrary to the expectations but is a result of the time needed by the swirl to travel from the runner exit to the representative location in the draft tube cone. For plane 2 and 4, it is even not possible to find a correlation between $V_{c,DT}$ and S. Exemplarily, this can be seen in plane 4 for $\sigma = 0.15$: Around $S \approx 0.26$, $V_{c,DT}$ changes significantly, while S remains almost constant. However, there exists also a period within this instability cycle where there is a change in swirl number ($0.265 < S < 0.305$) but the cavitation volume in the draft tube remains almost constant ($V_{c,DT}/V_{cone} \approx 0.004$).

A more thorough look into the results of plane 3 indicates that the location of the representative plane - where the correlation between $V_{c,DT}$ and S is satisfied - also depends on the cavitation number. While the results for $\sigma = 0.19$ and 0.21 can be approximated by a line with reasonable agreement, for $\sigma = 0.15$ this is partly violated as there is a period where a change of swirl number ($0.27 < S < 0.305$) does not lead to a variation of cavitation volume ($V_{c,DT}/V_{cone} \approx 0.004$). This can be explained by the average cavitation volume of the vortex rope that is displayed in figure 5.13. As the volume is similar for $\sigma = 0.19$ and 0.21 this explains that the same representative location is identified. The volume for $\sigma = 0.15$ is significantly shorter compared to the other two pressure levels, which justifies the change in the representative location.

The phase shift between the swirl oscillations in the different evaluation planes has already been presented in table 5.2. In figure 5.34, the cavitation volume in the draft tube is presented as function of swirl number for $\sigma = 0.19$ when the determined values of phase shift are applied. As pointed out above, for plane 3 the phase shift is 0° as it is the representative location in the draft tube cone. The phase shift for the other planes is applied in relation to plane 3. It can be observed that with the phase shift in all planes the expected behavior is present that $V_{c,DT}$ increases with increasing swirl number.

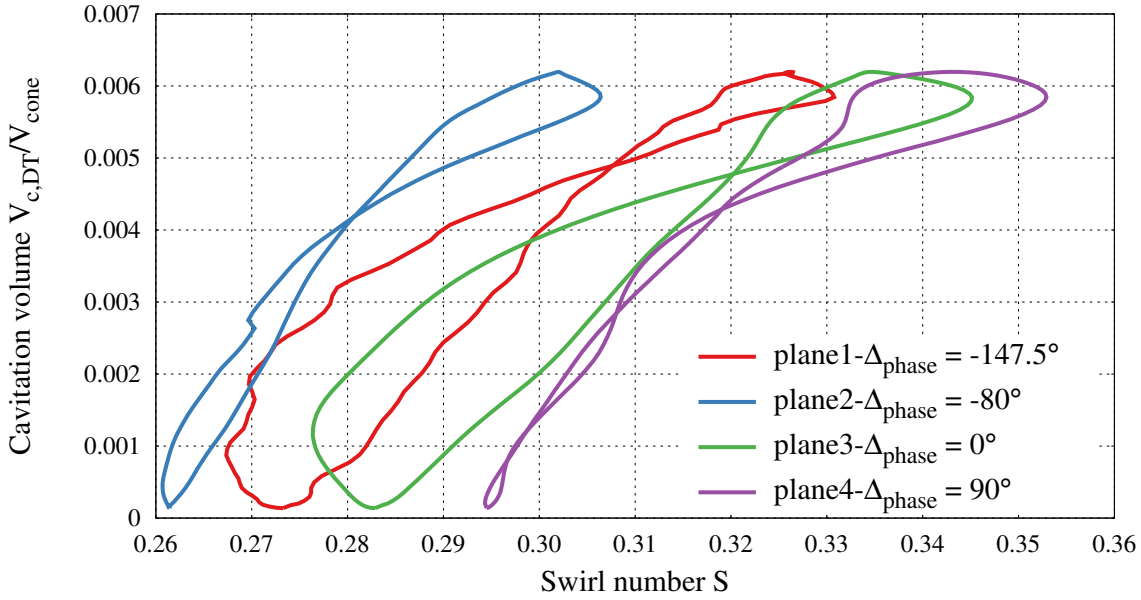

Figure 5.34: Cavitation volume in the draft tube as function of swirl number in the four evaluation planes for $\sigma = 0.19$. The results are mean phase averaged and for plane 1, 2 and 4 a phase shift is applied that corresponds to table 5.2.

All findings that have been presented so far, still cannot completely explain the physical mechanism behind the full load instability. A small pressure reduction from stable to unstable conditions could still act the following way: The pressure reduction leads to increased cavitation volume in runner and draft tube. After the reduced swirl - caused from increased $V_{c,RU}$ - reaches the draft tube, the current explanations would allow that a reduced $V_{c,DT}$ results in some new equilibrium if no significant pressure oscillations would occur. However, this is not the case for unstable conditions as a review of figures 5.11 and 5.24 shows. To close the gap in the physical mechanism of the full load instability, it is thus necessary to investigate the correlation between pressure and cavitation volume oscillations.

In section 2.6, it has been presented that the change of cavitation volume results in the emission of radiated acoustic pressure. Equation 2.15 states a proportionality of second time derivative of cavitation volume with the radiated acoustic pressure. The second time derivative of cavitation volume d^2V_c/dt^2 in the simulation domain is displayed in figure 5.35 as function of pressure at location C1N for different cavitation numbers. For $\sigma \geq 0.21$, the simulation results reproduce well the proportionality between d^2V_c/dt^2 and p. It is conspicuous that the linear trend cannot be reduced to one single line but is represented by a band. This can be explained by the superposition

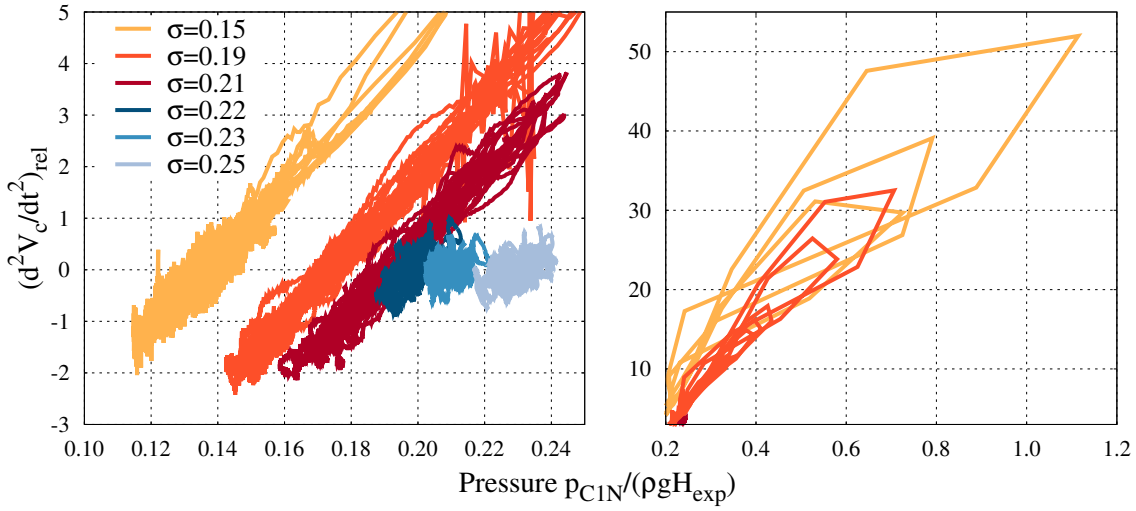

Figure 5.35: Second time derivative of cavitation volume in the simulation domain as function of pressure at location C1N for different cavitation numbers. Results display 20 runner revolutions for stable conditions and 12 instability cycles for unstable conditions. The results are made dimensionless with the maximum value that occurs at stable conditions.

of pressure oscillations that are caused by the change in cavitation volume (correlation from equation 2.15) with other pressure oscillations that could also be observed at non-cavitating conditions.

To be more precise: It is the acceleration of cavitation volume that leads to pressure radiation (see also section 2.6). This acceleration is equivalent to the curvature of temporal course of cavitation volume. Therein, a positive value of d^2V_c/dt^2 represents that V_c is curved convex, which corresponds to regions close to cavitation volume minimum. Negative values of d^2V_c/dt^2 stand for the case that V_c is curved concave, which corresponds to regions close to cavitation volume maximum.

The proportionality between d^2V_c/dt^2 and p can also be found with reasonable agreement for $\sigma = 0.15$ and 0.19 in the range $d^2V_c/dt^2 \leq 5$ (see figure 5.35 left). However, for $d^2V_c/dt^2 > 5$ (see figure 5.35 right), which corresponds to the period of cavitation volume collapse, simulation results partly deviate from the linear relation. This period, which is very limited in time, is characterized by huge pressure gradients that are caused by the cavitation volume oscillation. As cavitation volume cannot become negative, curvature of cavitation volume oscillation is very high in this period, which is the cause of the huge pressure peak. The deviations from the linear relation are caused by simulation inaccuracies that can be explained by steep gradients within this period

that cannot be accurately captured. However, as this period is only limited in time it can be expected that these inaccuracies are negligible.

All in all, with the correlation between d^2V_c/dt^2 and p all effects have been identified that are relevant for the explanation of the physical mechanism of the full load instability. As the interaction of the different effects that cause the full load instability is the main finding of this thesis, a detailed summary will be given separately in the next subchapter.

For the analysis of instabilities in hydraulic machinery, cavitation compliance and mass flow gain factor are often investigated (see section 2.5). They describe the change of cavitation volume caused by pressure and mass flow variations. In the following, the correlation between cavitation volume in the draft tube and pressure as well as discharge is analyzed, which draws upon the definitions of cavitation compliance and mass flow gain factor. However, it has to be highlighted that for the presented simulation results it is neither possible to determine cavitation compliance nor mass flow gain factor. For cavitation compliance, the reason is that pressure level at the outlet is kept constant and as explained above the pressure oscillation is a result of cavitation volume oscillation and not vice versa. The mass flow gain factor cannot be determined as the discharge at the inlet is kept constant and consequently the discharge oscillations are also caused by the cavitation volume oscillation.

In figure 5.36, the cavitation volume in the draft tube is plotted over pressure p_{ref}. Therein, p_{ref} is the area averaged pressure in evaluation plane 2. The figure shows that for stable conditions the relation between $V_{c,DT}$ and p_{ref} can be approximated by a linear relationship. For unstable conditions, the range of high cavitation volume shows also roughly a linear relation. However, for low $V_{c,DT}$ a small reduction in cavitation volume results in a significant change in pressure that has already been identified to result from the correlation between d^2V_c/dt^2 and p (see equation 2.15). Qualitatively, the shape of the curves for unstable conditions agrees well with experimental results on a micro-turbine with conical diffusor that is facing the full load instability (see Müller [121]). Therefore, it can be expected that the results from figure 5.36 are typical for the full load instability.

Finally, the correlation between the cavitation volume in the draft tube and the discharge is investigated. In figure 5.37, this is shown on the left when the discharge at the draft tube inlet $Q_{DT,in}$ and on the right when the discharge at the draft tube outlet $Q_{DT,out}$ is used. For $Q_{DT,in}$, all simulation results can be approximated by a vertical line. The highest fluctuations that are caused by variations of the blade cavitation

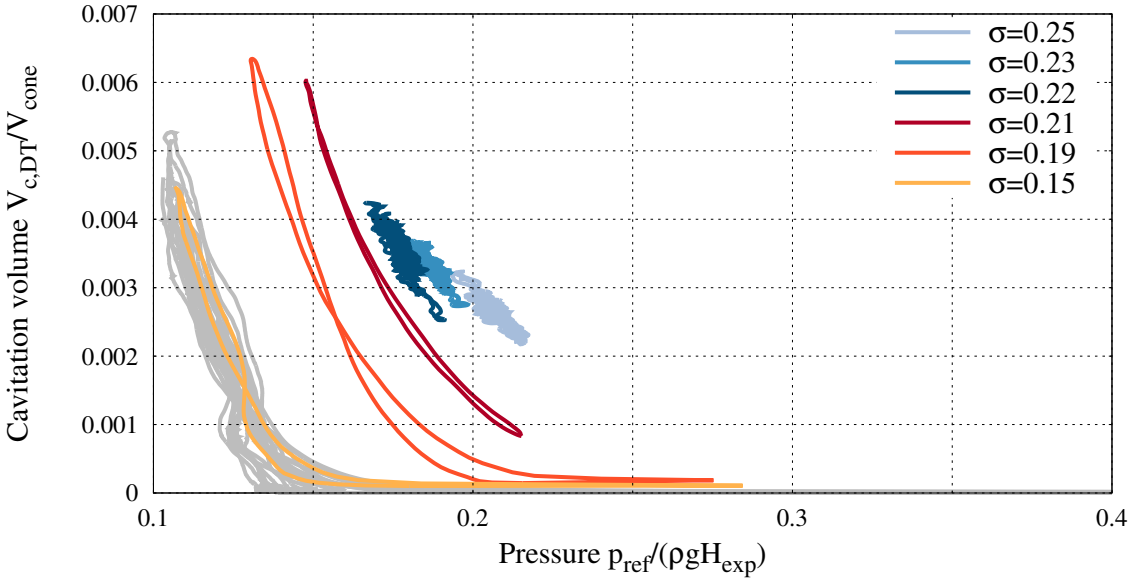

Figure 5.36: Cavitation volume in the draft tube as function of pressure for different cavitation numbers. The used pressure p_{ref} is the area averaged pressure in plane 2. The results for unstable conditions are presented mean phase averaged. Exemplarily, the full results of 12 instability cycles are displayed in plane 1 for $\sigma = 0.15$ (grey line).

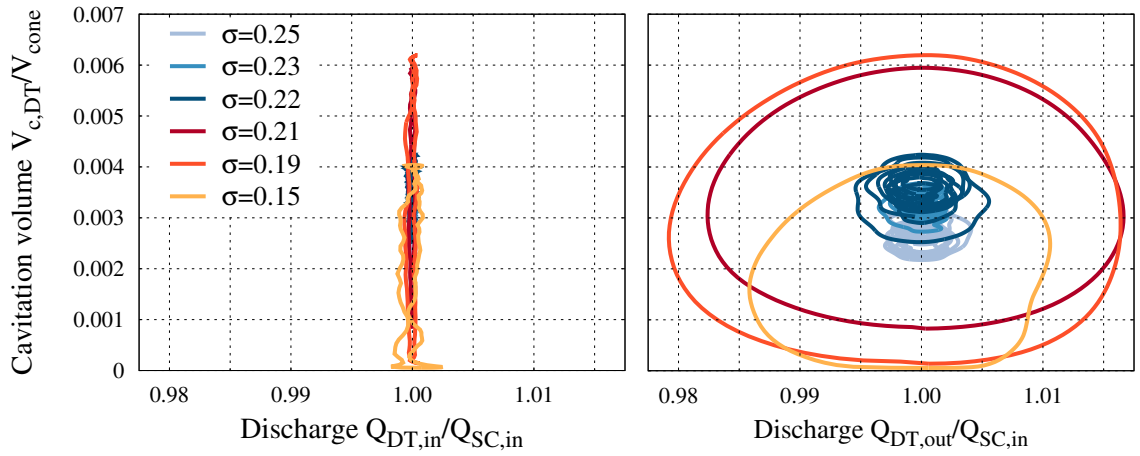

Figure 5.37: Cavitation volume in the draft tube as function of discharge at the draft tube inlet (left) and as function of discharge at the draft tube outlet (right) for different cavitation numbers. The results for unstable conditions are presented mean phase averaged.

volume in the runner are below 0.25% and occur for $\sigma = 0.15$. Consequently, the dis-

charge variations at the draft tube inlet are negligible for the investigated cavitation numbers, which is in agreement to the assumption made in figure 5.16 that $c_{m,c} = c_m$.

The discharge at the draft tube outlet varies only little for stable conditions. However, this changes significantly under unstable conditions. Then, variations of up to ± 2% can be observed. Without any phase shift the results give a roughly circular shape that qualitatively agrees well with the experimental results on a micro-turbine (see Müller [121]).

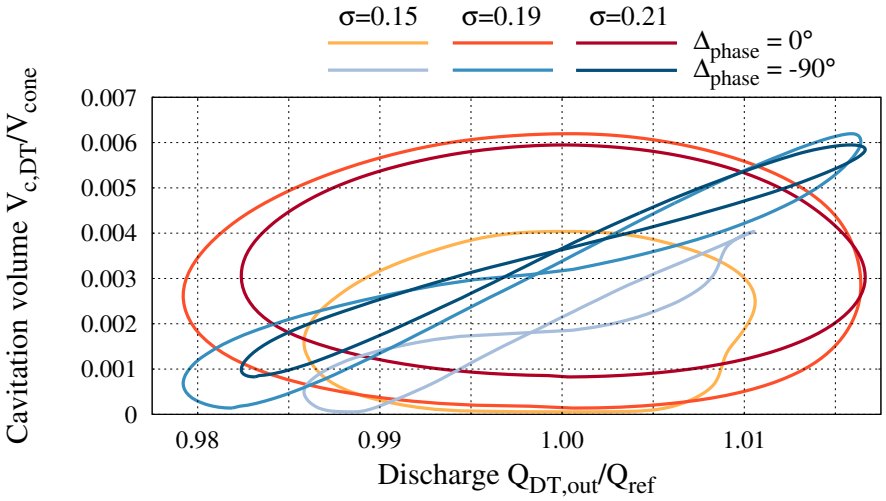

Figure 5.38: Cavitation volume in the draft tube as function of discharge at the draft tube outlet for three cavitation numbers at unstable conditions. The results are presented mean phase averaged.

A review of equation 2.9 shows that $V_{c,DT}$ is a function of $Q_{DT,in}$ and $Q_{DT,out}$:

$$\frac{dV_{c,DT}}{dt} = Q_{DT,out} - Q_{DT,in} \tag{5.3}$$

As $Q_{DT,in}$ can be approximated to be constant for the simulation results, $V_{c,DT}$ is directly linked to the discharge at the draft tube outlet. For the oscillation of the cavitation volume in the draft tube, it has been shown that it can roughly be approximated by a sine wave. Due to the fact that for sine oscillations the first derivative has a phase shift of -90° this phase shift is applied to the simulation results. The outcome is presented in figure 5.38.

For an ideal sine wave it could be expected that due to equation 5.3 the phase shifted results show a linear correlation between cavitation volume in the draft tube and the discharge at the outlet. The results show a slight deviation from this. For all

investigated cavitation numbers the results with a phase shift of -90° show a propeller shape. The reason for that is that the cavitation volume does not follow an ideal sine wave, which among other things is caused by the fact that cavitation volume cannot become negative. A more detailed discussion on that issue can be found in appendix B.

5.2.3 Physical Mechanism Behind Full Load Instability

In the previous subsection, all effects that are relevant for the development of the full load instability have been described. All the findings are summarized in this subsection. A schematic overview of the mechanism behind the full load instability is presented in figure 5.39.

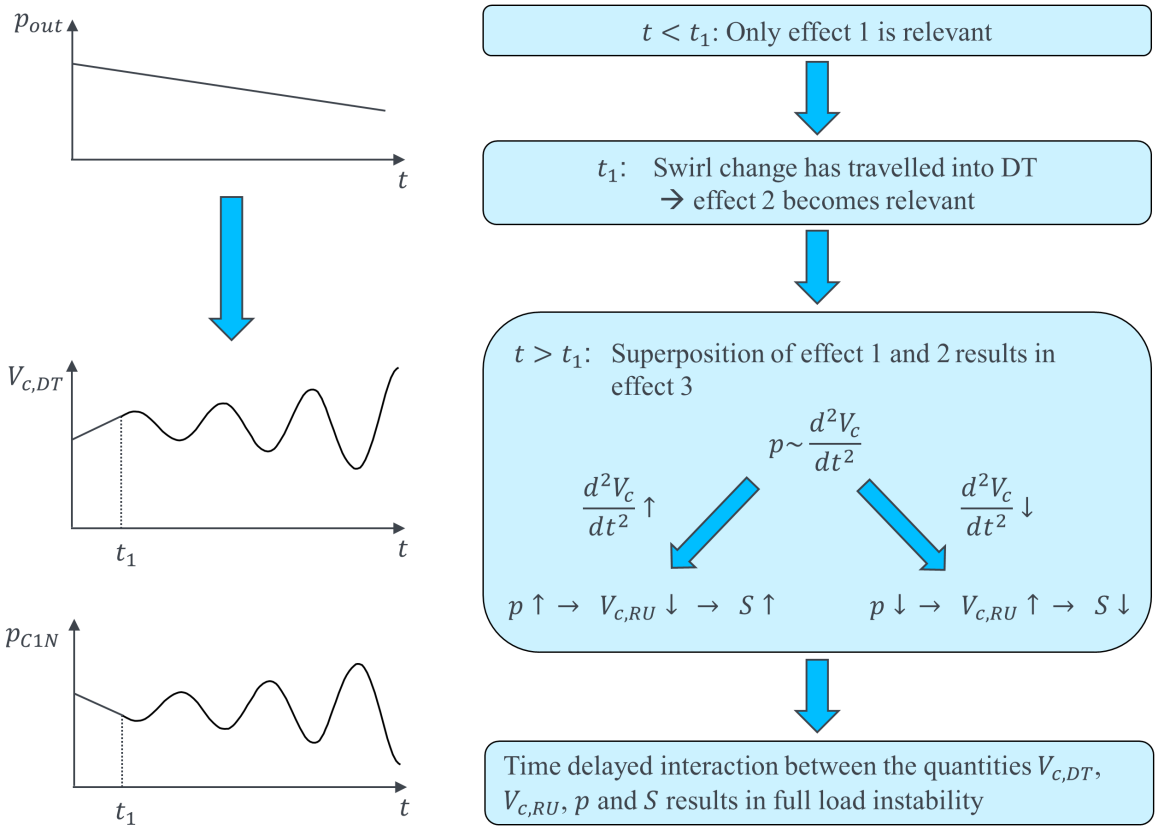

Figure 5.39: Schematic chart for the development of the full load instability.

Considered is the case that the pressure at the outlet p_{out} is slowly decreased. At time zero, p_{out} is at the pressure level that corresponds to the onset of the full load instability. Due to effect 1, the cavitation volume in the draft tube increases for $t < t_1$. Even though the occurrence of a cavitation volume in the runner leads to a reduced

swirl, effect 2 does not affect the cavitation volume in the draft tube for $t < t_1$, as the changed swirl needs some time to travel into the draft tube. At instant $t = t_1$ the swirl change has reached the draft tube and consequently effect 2 becomes relevant.

For $t > t_1$ it comes to a superposition of effect 1 and 2. This interaction is characterized by a time delay between the effects that results from the fact that pressure travels at the speed of sound, while swirl is transported with the flow. Effect 3 represents the correlation between p and d^2V_c/dt^2. Because of the superposition of effect 1 and 2, the cavitation volume decreases shortly after $t = t_1$. As a result d^2V_c/dt^2 increases, which causes the pressure to increase. This instantaneously results in a decreasing cavitation volume in the runner that is accompanied by increased swirl. Due to the interaction of the quantities $V_{c,DT}$, $V_{c,RU}$, p and S it comes to a negatively damped oscillation of the cavitation volume. This self-oscillation shows all the features that represent the full load instability.

5.3 Transition from Stable to Unstable

In the previous section, the physical mechanism of the full load instability has been identified with simulations at different cavitation numbers around the instability onset. To verify the findings, simulation results of the transition from stable to unstable are analyzed in this section. For that, two different durations of the transition are investigated. For the fast transition the pressure at the outlet is linearly decreased according to $\Delta\sigma/\Delta t = 0.08s^{-1}$ and for the slow transition according to $\Delta\sigma/\Delta t = 0.02s^{-1}$. The reduction of the outlet pressure for fast and slow transition is presented in figure 5.40. The transition is starting from $\sigma = 0.25$ and to have a continuously differentiable function for the outlet pressure, a cubic function is used that bridges from constant pressure level to the desired speed of pressure reduction. This procedure is applied to avoid effects that would result from the sudden jump from constant pressure level to linear pressure reduction.

To be able to easily compare the results between fast and slow transition a dimensionless transformed time scale τ_T is introduced that is defined as follows:

$$\tau_T = \frac{t - t_s}{\Delta t_T} \tag{5.4}$$

Therein, t_s denotes the time at the start of the transition and Δt_T stands for the time from the start of the transition until the moment when the outlet pressure reaches

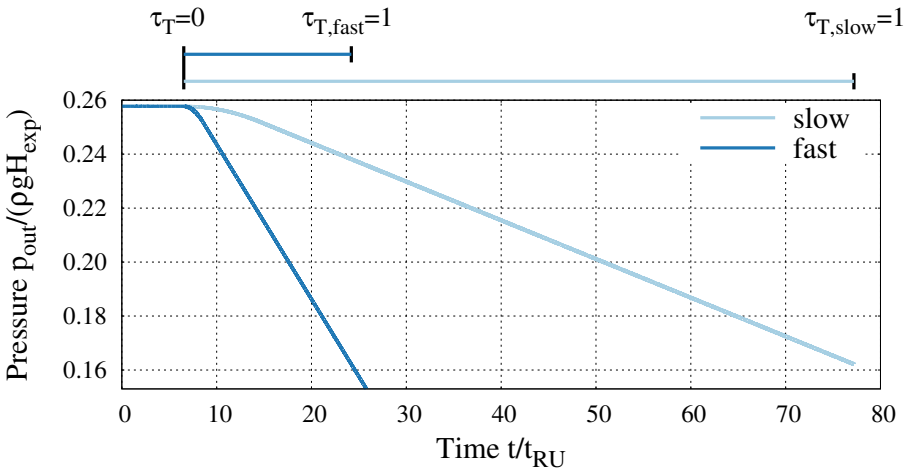

Figure 5.40: Pressure reduction at the outlet for fast and slow transition.

the value that corresponds to $\sigma = 0.15$. Consequently, this time scale is defined to be zero at the moment the transition starts and to be one at the moment the outlet pressure is reduced to the value that corresponds to $\sigma = 0.15$. The blend in with the cubic function is finished at $\tau_T = 0.113$. It has to be pointed out that the definition that $\tau_T = 1$ for $\sigma = 0.15$ is rather random.

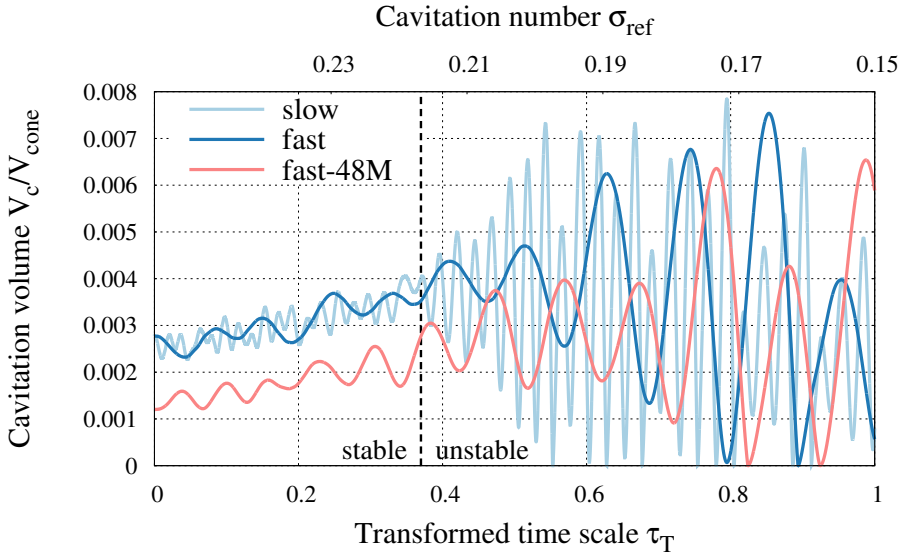

Figure 5.41: Cavitation volume in the whole simulation domain during fast and slow transition for mesh 14M. Additionally, the results with mesh 48M are presented for fast transition. All results are shown as function of τ_T. Cavitation number is directly linked to τ_T and is shown in addition.

The behavior of the cavitation volume of the whole simulation domain during the transition as function of τ_T is displayed in figure 5.41. Additionally, the cavitation number is shown on the second x-axis as a point of reference. It has to be noticed that this does not give any additional information as it is directly linked to τ_T, but it facilitates to get an impression of the particular pressure level. A comparison between fast and slow transition is made and additionally the result of the fast transition with the fine mesh (48M) is presented. For both simulations with mesh 14M a comparison of fast and slow transition shows that only minor cavitation volume oscillations occur until $\tau_T \approx 0.37$, which corresponds to a cavitation number that is slightly below 0.22. After that, for both transitions the amplitude of cavitation volume oscillations increases, which indicates the onset of the full load instability. As this starts slightly below $\sigma = 0.22$ this is in good agreement to the results presented in section 5.2.

However, a significant difference between fast and slow transition can be observed. While amplitude increases quite fast in terms of transformed time scale for slow transition - the first time that $V_c \approx 0$ occurs at $\tau_T \approx 0.55$, which corresponds to $\sigma \approx 0.20$ - for fast transition this takes place at significantly lower pressure level ($\tau_T \approx 0.8$ and $\sigma \approx 0.17$). This highlights that a certain amount of cycles is necessary until the severe oscillations have built up to maximum amplitude. It has to be pointed out that plotting the results over τ_T gives the impression that the building up of the instability is faster for the slow transition, which, however, is not the case. For a plot over time t, the results of the slow transition would be stretched by factor four compared to fast transition. This can be observed in the fact that in figure 5.41 the oscillation frequency of slow transition is four times the frequency of fast transition.

The results with mesh 48M show a smaller cavitation volume compared to the results with mesh 14M. As a consequence, the frequency of the cavitation volume oscillations is higher for mesh 48M as a smaller cavitation volume has a smaller inertia.

As described in section 2.5 self-oscillations may be described by a negatively damped linear oscillation. The solution of differential equation 2.13 is shown in appendix C. In figure 5.42, the results for representing the full load instability as a negatively damped linear oscillation are presented for fast and slow transition with mesh 14M. For slow transition the building up of cavitation volume oscillation can be represented by a negative damping with good agreement in the period $0.475 < \tau_T < 0.55$. This gives a further verification that the full load instability is of self-excited nature. The growth of the amplitude of the cavitation volume oscillation is limited to the range when

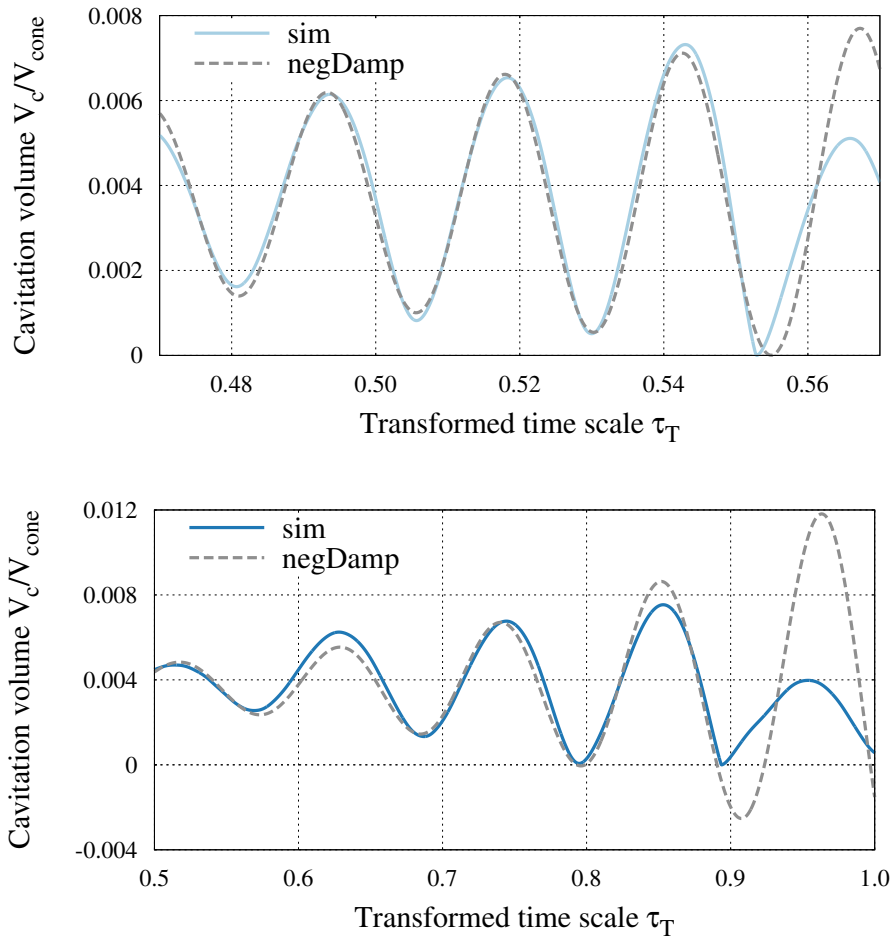

Figure 5.42: Representation of cavitation volume oscillation by a negatively damped linear oscillation. Top: Slow transition. Parameters for negative damping: $C_1 = C_2 = 7.5 \cdot 10^{-5}$, $\gamma = 12.8\,\mathrm{s}^{-1}$, $\omega^2 = 65000\,\mathrm{s}^{-2}$, $\phi_0 = 0.75$ and $\Delta y = 0.0037$. Bottom: Fast transition. Parameters for negative damping: $C_1 = C_2 = 7.5 \cdot 10^{-5}$, $\gamma = 9\,\mathrm{s}^{-1}$, $\omega^2 = 3200\,\mathrm{s}^{-2}$, $\phi_0 = 3.1$ and $\Delta y = 0.00375$.

cavitation volume becomes zero ($\tau_T > 0.55$). Then, the full load instability cannot be expressed by a negatively damped oscillation anymore.

For fast transition the simulation results can also be represented by a negative damping. Even though the agreement is not as good as for slow transition, the characteristics of a negatively damped oscillation can be found in the range $0.5 < \tau_T < 0.875$. Differences from ideal negative damping can be explained by the complex flow in a Francis turbine at off-design conditions. Other effects like pressure fluctuations that are not caused by the full load instability are superimposed and also have an effect on the cavitation volume oscillation.

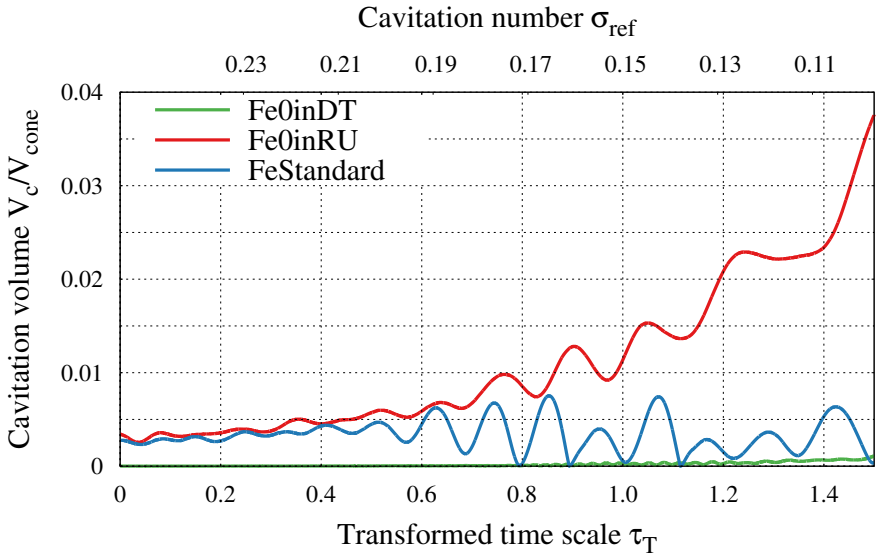

Figure 5.43: Cavitation volume in the whole simulation domain during fast transition for mesh 14M. Fe0inDT: Suppressed cavitation in DT. Fe0inRU: Suppressed cavitation in RU. FeStandard: No suppression of cavitation.

In figure 5.43, the impact of cavitation in the runner and draft tube is investigated for the fast transition. To be able to determine the impact of the different locations where cavitation occurs, the cavitation model constant for evaporation F_e is locally set to zero. Even though this methodology is unphysical, it is a great opportunity to distinguish between the effects that result from cavitation on the runner blades and from the cavitating vortex rope in the simulations, which would not be possible in experiments. The simulation results that suppress cavitation in the draft tube are denoted Fe0inDT, while those that suppress cavitation in the runner are labeled with Fe0inRU. Furthermore, the results of the fast transition with standard cavitation model constants are presented (FeStandard).

The results for the three different configurations differ significantly. As for the investigated operating point the cavitation volume in the draft tube is noticeable bigger compared to the runner, for suppressed cavitation in the draft tube a significantly smaller cavitation volume in the simulation can be observed compared to the other configurations. For suppressed cavitation in the runner, the cavitation volume increases with the pressure reduction. Even though the amplitude of cavitation volume oscillation increases for a lower outlet pressure, this is smaller compared to the amplitude that can be observed for configuration FeStandard, which is the only setup that shows the instability characteristics. Consequently, this verifies the mechanism

described in section 5.2, which states that the instability is caused by an interaction between cavitation in runner and draft tube.

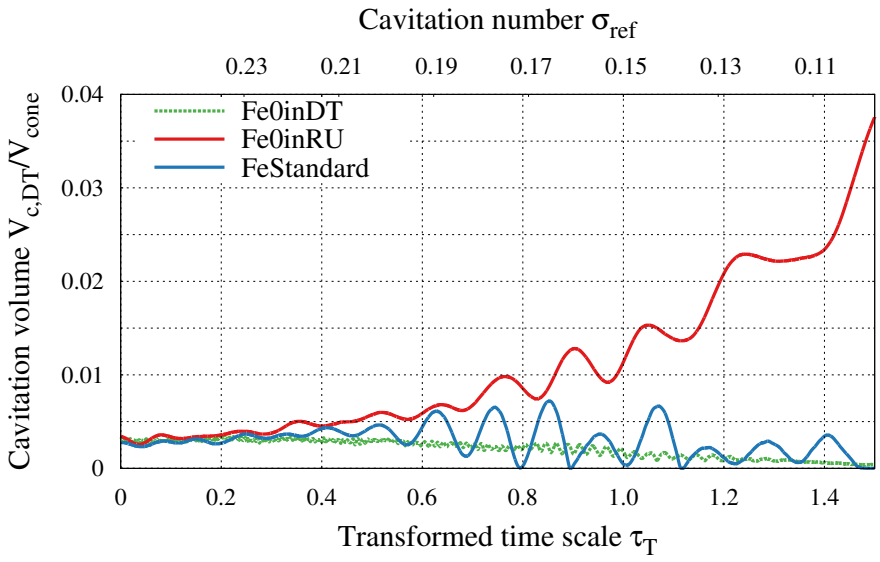

Figure 5.44: Cavitation volume in the draft tube during fast transition for mesh 14M. For Fe0inDT a pseudo cavitation volume is shown, which is determined from cells where pressure falls below vapor pressure. Pseudo cavitation volume is multiplied by a factor to have the same magnitude of cavitation volume at $\tau_T = 0$.

A closer look into the results of the cavitation volume oscillation in the draft tube (see figure 5.44) enables to differentiate between the cause of pressure reduction (effect 1) and the occurrence of cavitation on the runner blades that reduces the swirl (effect 2). It has to be pointed out that by setting $F_e = 0$ in the draft tube of course leads to $V_{c,DT} = 0$. Nevertheless, a pseudo cavitation volume can be determined by summing up the cell volume of all cells where pressure falls below vapor pressure. Normally, this pseudo cavitation volume is larger than the equivalent cavitation volume from a two-phase simulation as the pseudo cavitation volume counts all cells below vapor pressure with 100% to the cavitation volume, while in the two-phase simulations the volume fraction is decisive. For easier comparison the pseudo cavitation volume is multiplied by a factor to have the same magnitude of cavitation volume at $\tau_T = 0$.

While from the pressure reduction itself the cavitation volume in the draft tube increases (Fe0inRU), the increased cavitation volume in the runner for reduced cavitation numbers results in a reduced cavitation volume in the draft tube (Fe0inDT). It is conspicuous that a superimposition of these two effects does not result in the results

from configuration FeStandard. Consequently, both effects are important and only the interaction of them results in the typical characteristic of the full load instability.

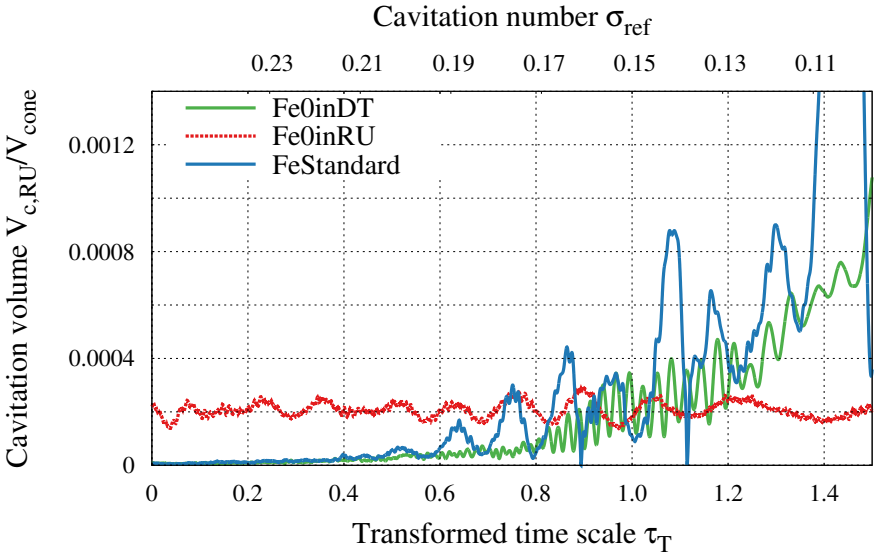

Figure 5.45: Cavitation volume in the runner during fast transition for mesh 14M. For Fe0inRU a pseudo cavitation volume is shown, which is determined from cells where pressure falls below vapor pressure. Pseudo cavitation volume is multiplied by the same factor that is used for figure 5.44.

Analog to the draft tube, the cavitation volume in the runner is analyzed (see figure 5.45). For suppressed cavitation in the draft tube it can be seen that, as expected, the cavitation volume increases during the transition. Up to $\tau_T = 0.8$ the amplitude of the cavitation volume oscillation is small and becomes higher for $0.8 < \tau_T < 1.2$. After that the amplitude decreases again. The pseudo cavitation that can be determined for suppressed cavitation in the runner is quite constant. Nevertheless, oscillations are present that can be explained by the pressure oscillation that is caused from the changing cavitation volume in the draft tube (equation 2.15). Consequently, the findings from section 5.2 are verified that there is a feedback from draft tube cavitation volume oscillations to the cavitation on the runner blades.

The behavior of the pressure during the transition at location C1N is displayed in figure 5.46. In the upper part of the figure the results for fast and slow transition and additionally the results of the fast transition with mesh 48M is presented. Analog to the findings for the cavitation volume it can be observed that for fast and slow transition only minor pressure fluctuations occur until $\tau_T \approx 0.4$, while amplitude increases afterwards. For slow transition the first dramatic pressure peak can be found at $\tau_T \approx 0.55$, which coincides with the moment when $V_c \approx 0$ for the first time. This can

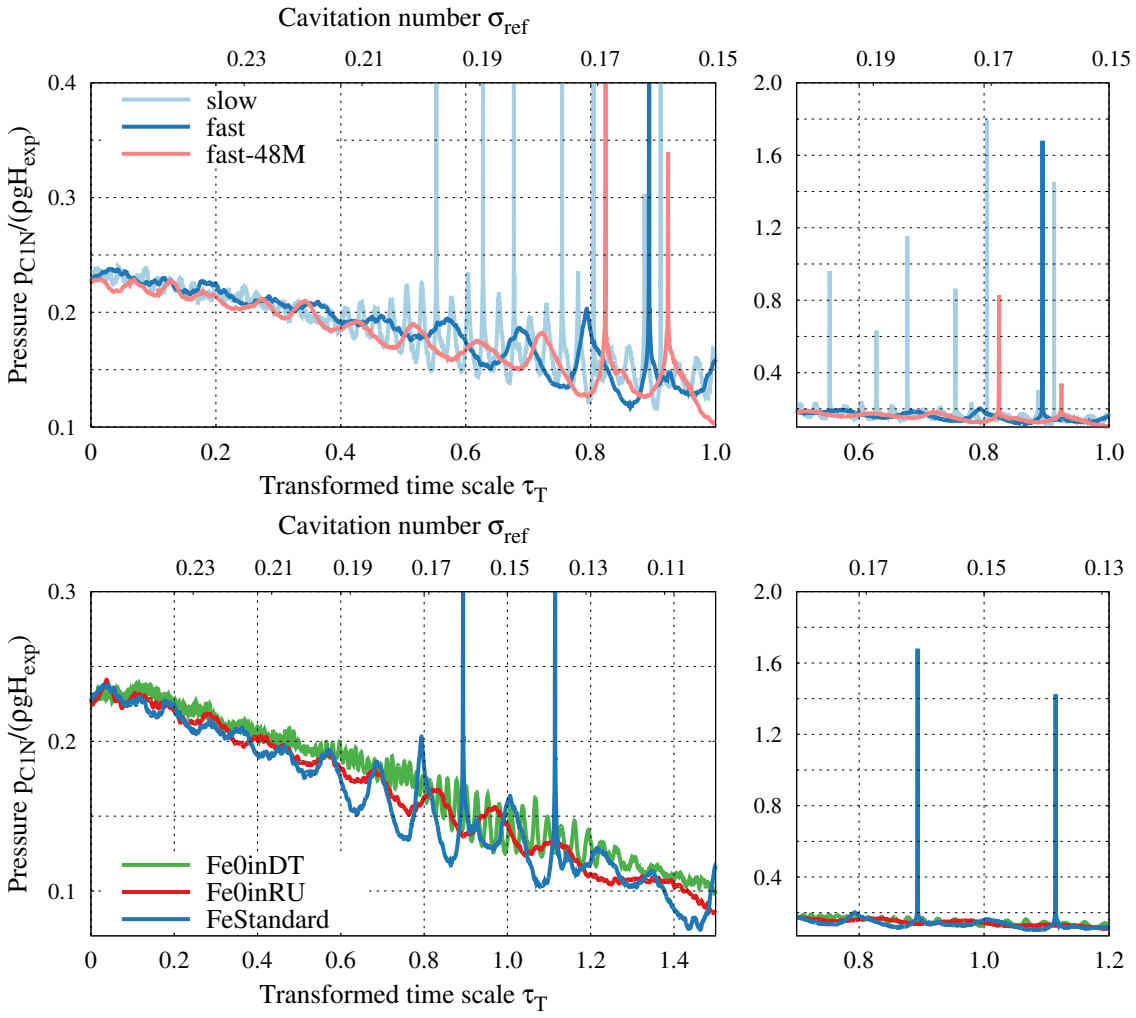

Figure 5.46: Pressure at location C1N during transition from stable to unstable. Top: Fast versus slow transition. Bottom: Local suppression of evaporation.

be explained with equation 2.15. As the cavitation volume cannot become negative, a cavitation volume minimum has to occur and the curve has a strong curvature, which is the cause of the severe pressure peak. Peaks that are of similar magnitude can be observed for the fast transition for both meshes. For mesh 48M a slightly higher frequency of the pressure oscillations can be observed that can be explained by the smaller cavitation volume.

In the lower part of figure 5.46, the results are presented for suppression of cavitation at different locations. Analog to the results for the cavitation volume it can be found that the three different configurations differ significantly. For suppressed cavitation in the draft tube, high frequency pressure oscillations occur that have only small amplitude

up to $\tau_T = 0.8$. Even though amplitude is higher in the range $0.8 < \tau_T < 1.2$ it is by factor 40 smaller compared to the most severe pressure peaks that are present for the full load instability (FeStandard). For $\tau_T > 1.2$, amplitude is low again, which is in agreement with the findings from the cavitation volume.

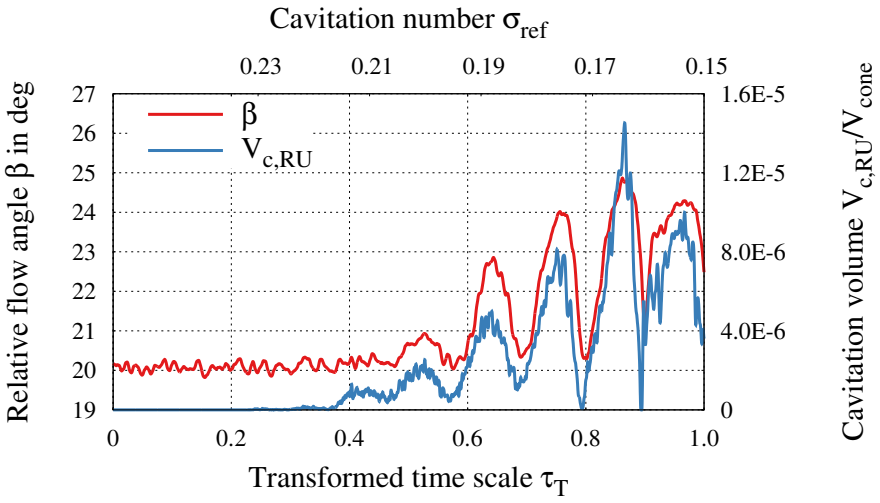

Figure 5.47: Moving average of relative flow angle at location DTin08 and related cavitation volume within the averaging ribbon for fast transition.

In the following, the correlation between the occurrence of cavitation on the runner blades and a modification of relative flow angle β as well as the swirl number is analyzed. The results for the moving average of β at location DTin08 and the associated cavitation volume in the averaging ribbon are presented in figure 5.47 for fast transition. Similar to the observations from simulations at constant cavitation number, a clear link between the occurrence of cavitation on the runner blades and an increased relative flow angle can be stated. It is clearly noticeable that the modification of β increases with increasing blade cavitation.

The link between blade cavitation and β can be further verified with the results with suppressed cavitation in runner or draft tube (see figure 5.48). For suppressed cavitation in the runner, β remains constant around 20° with only minor fluctuations that are a result of velocity fluctuations. On the other hand, with suppressed cavitation in the draft tube, the modification of relative flow angle can be observed. The behavior of β in terms of the oscillations is different compared to the simulation without suppression of cavitation, but this can be explained by the instability that only occurs for configuration FeStandard. Nevertheless, the general trend of β is in good agreement for configuration Fe0inDT compared to FeStandard.

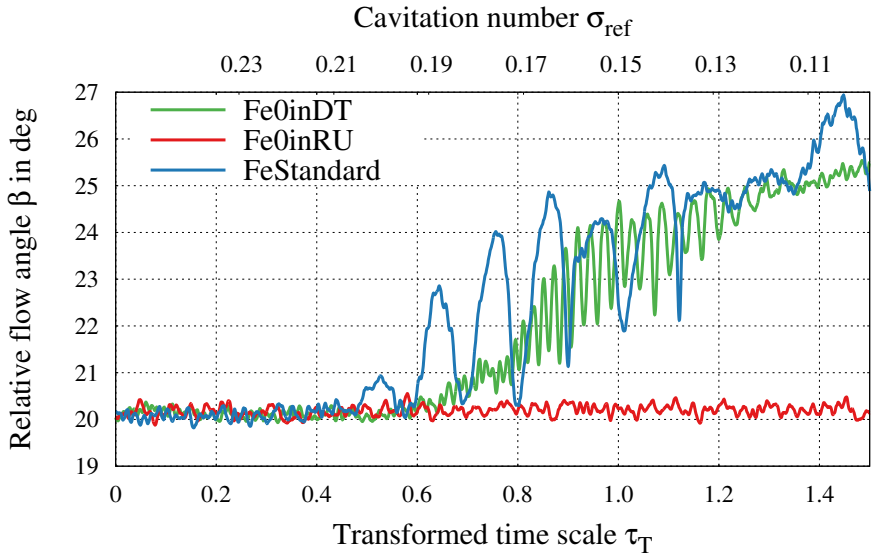

Figure 5.48: Moving average of relative flow angle at location DTin08 for fast transition.

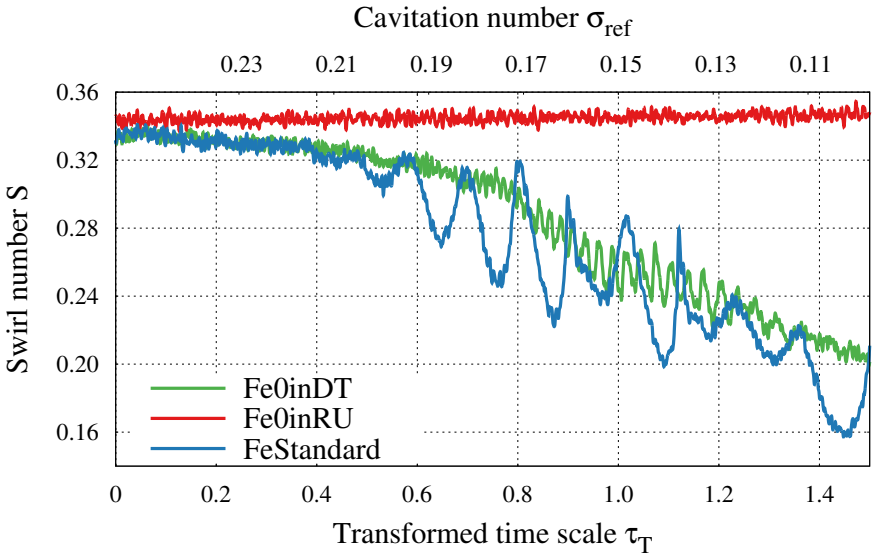

Figure 5.49: Swirl number in plane 1 during fast transition for mesh 14M.

Analog observations can be made for the swirl number. The results for plane 1 are displayed in figure 5.49. Again, swirl number remains almost constant for suppressed cavitation in the runner, while the other two simulation results show a strong dependency on cavitation number. In the range of stable conditions ($\tau_T < 0.4$), the results for configuration Fe0inDT and FeStandard match well and swirl number reduces only slightly as the cavitation volume in the runner is quite small. A further reduction of

pressure level results in a faster reduction of swirl number for both configurations. However, the results do not match anymore due to the onset of instability.

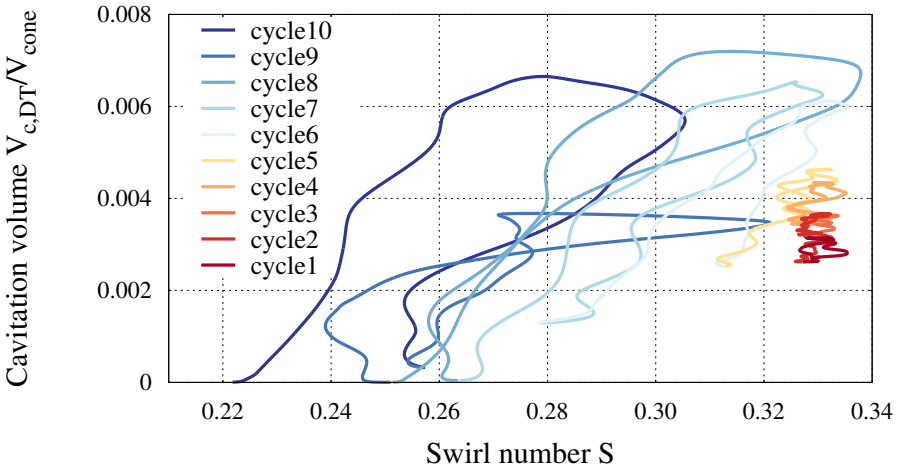

Figure 5.50: Cavitation volume in the draft tube as function of swirl number in plane 3 for fast transition with mesh 14M. Cycles range from one cavitation volume minimum to the next. Cycle 1 starts at $\tau_T \approx 0.1$.

In figure 5.50, the cavitation volume of the vortex rope is plotted as function of swirl number in plane 3 for the simulation of the fast transition to investigate the link between swirl number and cavitation volume in the draft tube. Therein, one cycle extends from one cavitation volume minimum to the next. Cycle 1 starts around $\tau_T \approx 0.1$ and cycle10 ends around $\tau_T \approx 1.1$. It has to be mentioned that even though the instability onset is around $\tau_T \approx 0.4$ it is possible to define cycles for $\tau_T < 0.4$ as cavitation volume oscillations of small amplitude can also be observed for stable conditions. Plane 3 is selected as the results from section 5.2 showed that for this plane the phase shift between the oscillations of cavitation volume and swirl number tends to zero.

It can be observed that from cycle 1 to 4 the swirl number remains almost constant while the cavitation volume increases. This can be explained by the small size of cavitation volume in the runner that, until then, has only a negligible effect on the swirl. On the other hand, the pressure reduction leads to an increased cavitation volume in the draft tube. With cycle 5 the instability starts to build up. Due to the fact that the cavitation volume in the runner becomes relevant, this results in a reduced swirl number. The time delay between the effect of pressure reduction and the counteracting effect of swirl reduction leads to the formation of the self-oscillation as described in section 5.2.

From cycle5 to cycle 8 the amplitude of the cavitation volume oscillation in the draft tube increases. Simultaneously, the trend of decreasing swirl number can be observed that is a result of increased cavitation volume in the runner. After cycle 8 cavitation volume oscillation in the draft tube does not increase anymore. It is even possible that single cycles have a significantly smaller amplitude like it is the case for cycle 9. Apart from this cycle, all cycles in the instability regime show the correlation between $V_{c,DT}$ and S that decreasing swirl number results in a smaller cavitation volume.

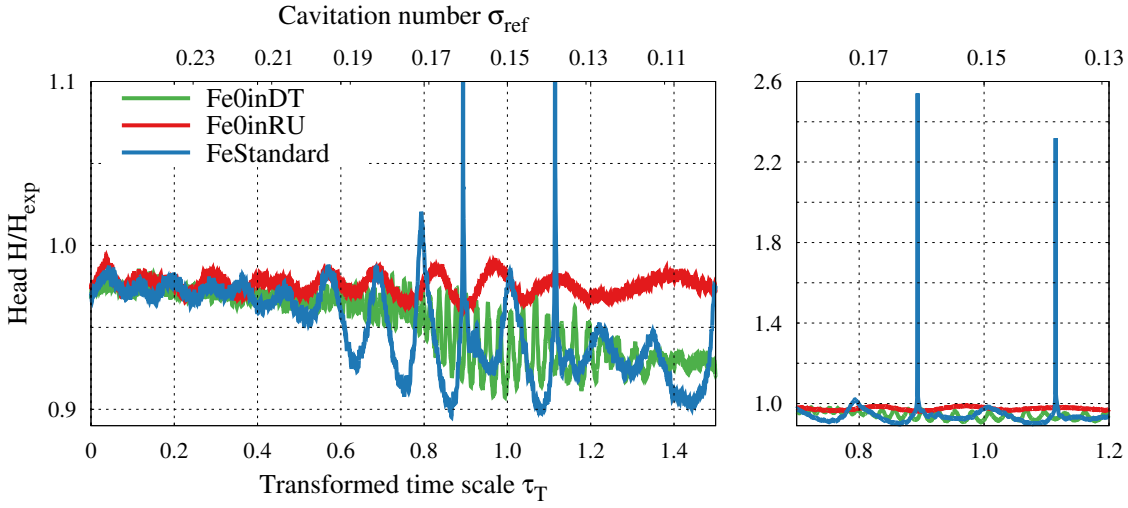

Figure 5.51: Head as function of transformed time scale for fast transition with mesh 14M.

In figure 5.51, the impact of cavitation in runner and draft tube on head is investigated. For the investigated operating point, cavitation in the draft tube has only a minor effect on head. Some oscillations can be detected, which, however, can be traced back to the pressure fluctuations caused by the cavitation volume oscillation. Consequently, the reduction in head that can be observed for the other two configurations can be fully attributed to the occurrence of cavitation in the runner. Two huge peaks can be found for configuration FeStandard around $\tau_T \approx 0.88$ and 1.12. These peaks have the values $H/H_{ref} = 2.55$ and 2.32 and are caused by the severe pressure peaks that occur when the cavitation volume collapses (see figure 5.43 for comparison).

The results for torque are presented in figure 5.52. Analog to the findings from head, it can be found that torque is not affected by cavitation in the draft tube. Consequently, the reduction in torque with decreasing pressure is a result of cavitation on the runner blades. This can be explained by the occurrence of cavitation on the suction side of the runner blades. First, this limits the pressure difference between pressure and suction side. Secondly, the changed relative flow angle at the runner outlet plays also

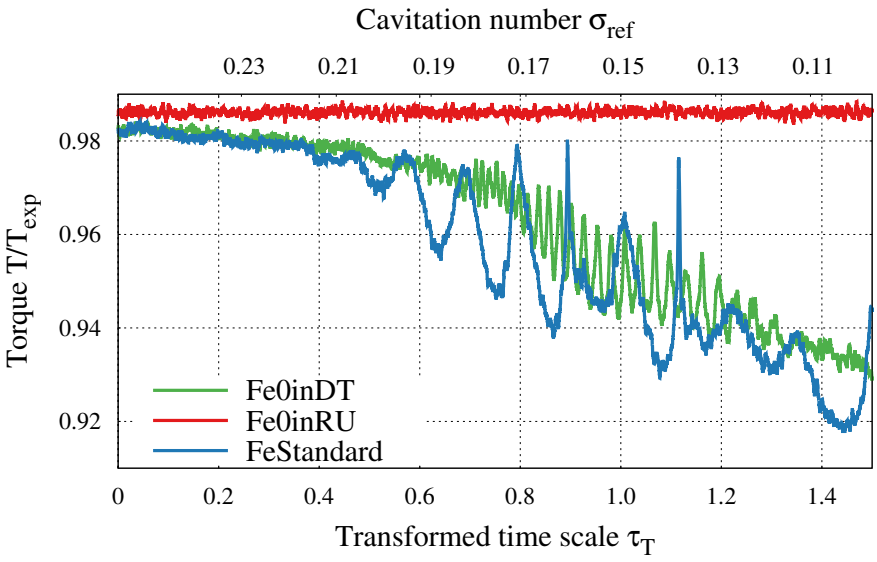

Figure 5.52: Torque as function of transformed time scale for fast transition with mesh 14M.

an important role, as c_u changes and this affects the torque due to Euler's turbine equation. The maximum amplitude of torque fluctuation is around 5%, which agrees well with experimental results from Müller [121], who monitored fluctuations with an amplitude in the range of 4-6%. These strong fluctuations indicate that the full load instability is accompanied by severe power swings that are not desirable for a safe hydropower plant operation.

6 Discussion

The numerical investigations on the Francis turbine have revealed an explanation for the physical mechanism behind the full load instability. Nevertheless, different aspects need to be further discussed. First, the transferability of the findings to other operating points has to be verified. Secondly, the use of a constant mass flow boundary condition at the inlet needs to be discussed. Furthermore, similarities and deviations to experimental observations have to be analyzed. Additionally, the variation of discharge or rotational speed can lead to similar variations of the velocity triangle at the runner outlet and consequently needs further explanation. Finally, an adapted 1D model is proposed that takes into account the new findings.

6.1 Transferability to other Operating Points

All findings from chapter 5 have been acquired for one specific operating point. If the identified physical mechanism is universal, it should be transferable to other full load operating points. To verify this general validity, two further simulations of the fast transition (see section 5.3) are performed for a guide vane opening of 27° and 29°. For both simulations the rotational speed remains constant and the discharge is set to have the same n_{ED} as for the simulations from the previous chapter. This results in a decrease of discharge factor of 0.005 for a guide vane opening of 27° and an increase of 0.005 for a guide vane opening of 29°. The location of the operating points in the hill chart is displayed in figure 6.1.

Due to the fact that cavitation on the runner blades already occurs for higher cavitation numbers, the transition for a guide vane opening of 29° (see figure 6.2) starts at $\sigma = 0.29$. It can be observed that the operating point is stable for high cavitation numbers, when the cavitation volume in the runner is close to zero. In these cases, a huge cavitation volume in the draft tube is present that is bigger compared to 28° guide vane opening, which corresponds to the expectations. With decreasing cavitation number, the cavitation volume in the runner slightly increases and instability develops. Even though a different operating point was investigated, the size of cavita-

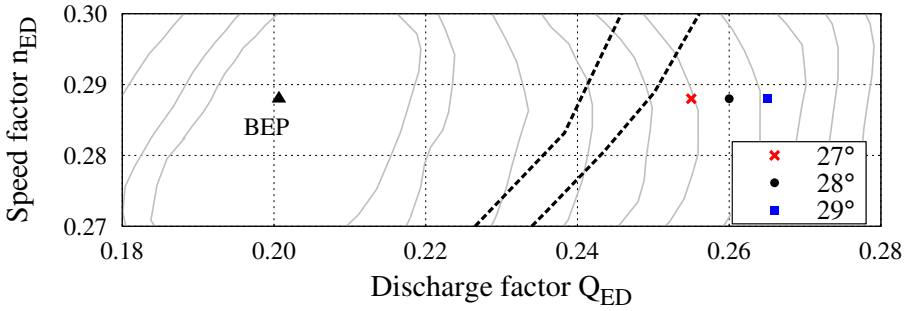

Figure 6.1: Detail from the hill chart with marked position of the investigated operating points. Rope free zone is marked by dashed lines.

tion volume in the runner at the onset of instability is similar to the observations for a guide vane opening of 28° (see figure 5.45 for comparison). Consequently, a transferability of the findings from the previous chapter to the operating point with guide vane opening 29° can be stated.

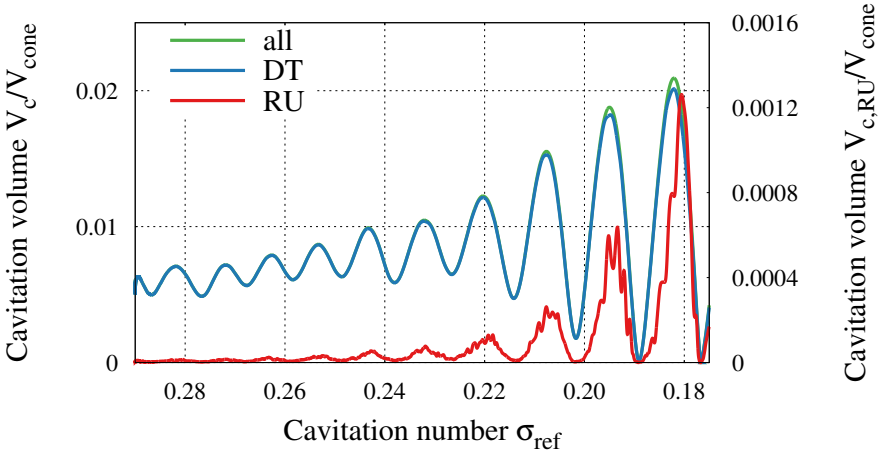

Figure 6.2: Cavitation volume in runner, draft tube and the whole simulation domain during fast transition for a guide vane opening of 29°. Mesh 14M has been used for the simulation.

In figure 6.3, the results for the transition with 27° guide vane opening are presented. At $\sigma = 0.25$, neither cavitation occurs in the draft tube nor in the runner. Down to $\sigma \approx 0.21$, the cavitation volume in the draft tube increases. However, it is still significantly smaller compared to the other two operating points with larger guide vane opening. Due to the occurrence of cavitation in the runner, a further reduction of the pressure level results in a reduced swirl, which provokes a decreasing cavitation volume in the draft tube until it becomes zero around $\sigma = 0.19$. For this investigated

operating point, no full load instability can be observed. This can also be explained by the findings from the previous chapter. The development of the full load instability results from an interaction of the cavitation volume in the runner and draft tube. However, for 27° guide vane opening the vortex rope is too weak, thus the cavitation volume in the draft tube is too small at the pressure level when blade cavitation becomes relevant. Consequently, the self-oscillation cannot develop.

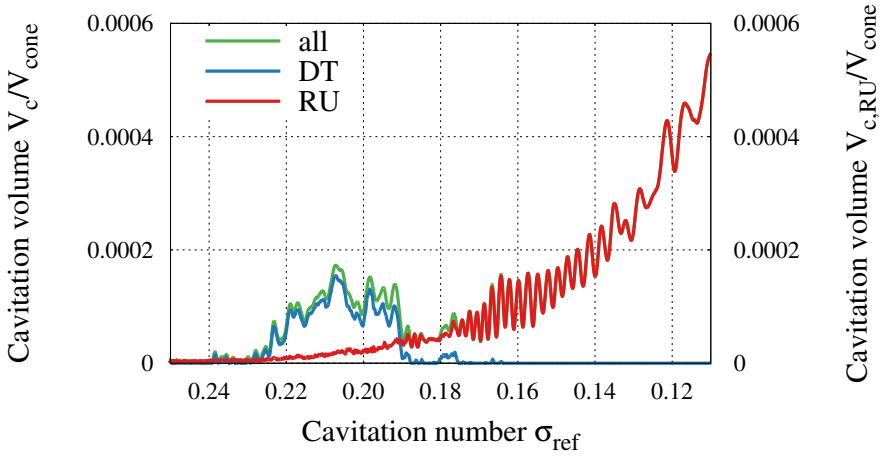

Figure 6.3: Cavitation volume in runner, draft tube and the whole simulation domain during fast transition for a guide vane opening of 27°. Mesh 14M has been used for the simulation.

The results from this section clearly verify the universality of the identified physical mechanism behind the full load instability. They highlight that the presence of cavitation in the runner as well as in the draft tube is essential for the development of the instability. This also explains that for full load operating points that are close to best efficiency point, no instability is to be expected.

6.2 Inlet Boundary Condition

In a previous publication [163], it has been stated that setting a constant mass flow at the inlet boundary condition is not appropriate to capture the full load instability. Based on the findings from this thesis, this statement is disproved. Nevertheless, the use of a constant mass flow at the inlet boundary condition needs further discussion. For stable conditions it can be expected that this boundary condition is a good approximation and for that reason it is common practice for simulations of hydraulic turbines. Contrary to that, for the occurrence of the full load instability highly un-

steady flow phenomena can be observed. Due to the severe pressure surge that is caused by the collapse of cavitation volume it can be expected that the discharge experiences variations that are not in agreement with a constant mass flow boundary condition. To take into account the discharge variations in the simulation it is necessary to perform simulations with 1D-3D coupling.

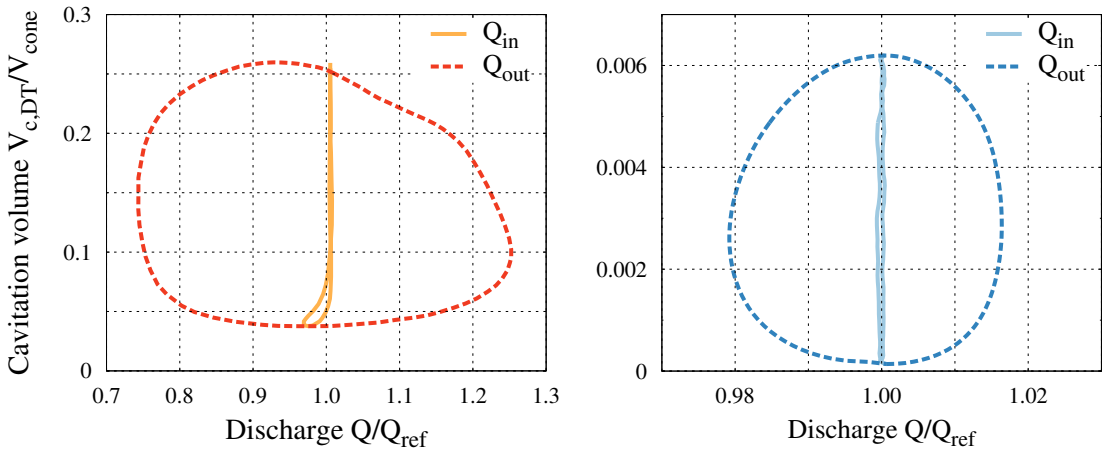

Figure 6.4: Cavitation volume in the draft tube as function of discharge at the draft tube inlet or outlet, respectively. All results are presented mean phase averaged. Left: Experimental results from Müller [121] on a simplified test case. The presented results are for $\sigma = 0.13$. Right: Simulation results for the Francis turbine at 28° guide vane opening and $\sigma = 0.19$.

To quantify the relevance of a variable inlet discharge, experimental results from Müller [121] on a simplified test case are analyzed. This test case consists of a micro-turbine with a horizontal conical diffuser that is operated in a small scale hydraulic circuit. The results show that the discharge at the draft tube inlet is constant over a wide range of cavitation volume oscillation and only around cavitation volume minimum the experiments indicate a discharge reduction up to 4% (see figure 6.4 left). This is qualitatively in good agreement to simulation results for the Francis turbine that are presented on the right side of figure 6.4. For the Francis turbine the discharge at the draft tube inlet is almost constant, while the experimental results show a period of varying discharge at the inlet when the cavitation volume is small. However, as the discharge variation is only present around minimum cavitation volume it can be expected that the use of a constant mass flow boundary condition is reasonable. Furthermore, taking into account that for the simplified test case the discharge variations at the draft tube outlet are significantly higher compared to the investigated Francis turbine, it can be expected that for the Francis turbine the discharge variations at

the inlet are also smaller. However, the effect of the inlet boundary condition should be studied more detailed in the future. At least for resonance conditions with the pipe system that are not expected within this thesis, a constant mass flow boundary condition at the inlet would not be suitable.

6.3 Comparison with Experimental Observations

The results from chapter 5 show that many characteristics of the full load instability, which can be found in the experiments, are also present in the simulations. For example a swirl variation can be observed as well as a link of the instability onset with the occurrence of cavitation on the runner blades. However, also differences between simulation results and the measurement can be identified. While the experiments indicate that the instability onset is around $\sigma \approx 0.155$ the simulations with mesh 14M predict an instability onset around $\sigma \approx 0.215$. Due to this deviation no direct comparison between experimental and simulation results could be presented in the previous chapter. It can be expected that the difference in instability onset comes from a deviation of the onset of cavitation on the runner blades. As the simulation results predict blade cavitation at too high cavitation numbers, the instability develops too early.

There is a variety of possibilities for the deviation between simulation and experiment. First, the mesh has an impact as already identified in sections 5.2 and 5.3. With mesh 48M onset of instability can be expected at slightly lower cavitation number, which is in better agreement to the measurements. However, a better agreement in terms of cavitation volume in the draft tube is present for the coarser mesh.

As identified in section 4.2, the turbulence model can have a significant impact on the simulation accuracy. This indicates that the turbulence model may also have a relevant effect on the instability onset. However, as explained in section 5.1, for the SBES model an unphysical interaction between two-phase modeling and turbulence model could be observed. This highlights the high complexity of two-phase simulations for turbulent flows. In future, the development of new turbulence models that have a better interaction with two-phase models might overcome this issue. However, the unphysical interactions with the hybrid RANS-LES turbulence model restrict to analyze the impact of turbulence model on the instability onset for present setups. Nevertheless, it has to be highlighted that with the applied RANS approach the physical mechanism behind the full load instability could be identified.

One important aspect for the development of the full load instability is the time delay between effect 1 and 2. For incompressible simulations this time delay is big as the speed of sound becomes infinite, whereas the transport velocity of the flow is in the order of 10 m/s. While for pure water the speed of sound in the experiments can be expected to be around 1200 m/s, it may reduce due to the occurrence of cavitation to the order of 100 m/s. This is still one order of magnitude above the transport velocity of the flow, however, compressible effects might already have an impact on simulation results. As these compressible effects result in a decreased time delay between effect 1 and 2, they might also partly explain that the instability onset is at smaller cavitation number in the experiments.

Last, simulation inaccuracies resulted in a shifted operating point (see figure 5.20). The deviation in operating point is a further cause for deviations of the onset of instability between simulation and experiment. Compared to single-phase simulations the accurate prediction of cavitation phenomena is much more challenging as already small deviations in the flow field might result in differences in the pressure field. This directly affects the mass transfer between liquid and vapor phase. All in all, it can be stated that the accurate prediction of instability onset is very challenging.

6.4 Cause of Full Load Instability

The identified mechanism of the full load instability differs to the explanations of the cause that can be found in state of the art literature. By means of 1D simulations, variations of the discharge at the draft tube inlet (mass flow gain factor) are commonly used as cause of the instability. Indeed, different effects that are presented in figure 6.5 can result in a swirl reduction and might consequently be the cause of the instability.

First, the occurrence of cavitation on the suction side of the runner blade can result in an increased flow angle ($\beta_c > \beta$), which results in a reduction of c_u. Secondly, a reduction of discharge ($c_{m,Q\downarrow} < c_m$) also leads to reduced c_u. Finally, the same effect can be found for increased rotational speed ($u_{n\uparrow} > u$). All effects have in common that they change the velocity triangle at the runner outlet. The resulting swirl change needs some time to travel into the draft tube, which is one requirement for the development of self-oscillation. However, only for the case of cavitation on the runner blades the time delay for the relevant location in the draft tube cone is guaranteed due to effect 3 (direct feedback due to correlation of p and d^2V_c/dt^2). For discharge or rotational speed

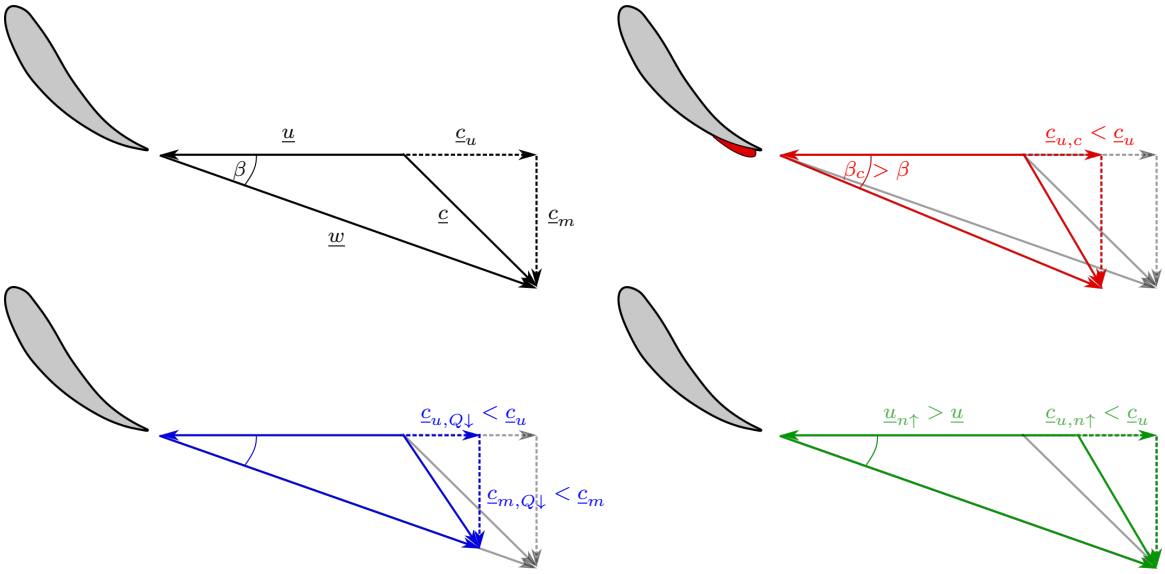

Figure 6.5: Velocity triangles for full load operating point. Top left: Initial velocity triangle for non-cavitating conditions. Top right: Cavitating conditions. Bottom left: Decreased discharge. Bottom right: Increased rotational speed.

variations, these oscillations might have a phase that excites instability but also might have a phase that dampens oscillations.

Especially discharge variations that seem to be more likely compared to variations of rotational speed might also be a possible explanation for the cause of the full load instability. However, then the whole mechanism would be the result of a system instability. This means that the occurrence of the instability highly depends on the test rig or upstream pipe system of the hydro power plant as for different pipe lengths a different traveling time of the pressure wave can be expected. Contrary to this, for the occurrence of blade cavitation there is always a direct feedback (effect 3), which should be almost independent from the system. Due to the fact that for the investigated Francis turbine the full load instability can also be observed on prototype [132], a system dependency cannot be found between model and prototype, which supports the findings from this thesis.

6.5 1D Model

Based on the discussion in section 6.4, the nowadays typical 1D modeling of the cavitation volume oscillation caused by the full load instability based on the parameters mass flow gain factor χ and cavitation compliance C_c (see section 2.5) has to be re-

vised. To consider all relevant effects of the full load instability the following equation is proposed[2]:

$$Q_1 - Q_2 = -\frac{dV_c}{dt} = \chi\frac{dQ_1}{dt} + \epsilon\frac{dn}{dt} + \psi\frac{dh}{dt} + C_c\frac{dh}{dt} \tag{6.1}$$

Therein, ϵ denotes the rotational speed gain factor

$$\epsilon = -\frac{\partial V_c}{\partial n} \tag{6.2}$$

that has already been proposed by Alligné et al. [6] in a similar way. Furthermore, the cavitation gain factor ψ

$$\psi = -\frac{\partial V_c^*}{\partial h} \tag{6.3}$$

is newly introduced. It takes into account the correlation between the cavitation volume in the draft tube and the changed flow angle caused by blade cavitation. The cavitation gain factor has a special character. Even though it is caused by a change of pressure, the actual change of cavitation volume in the draft tube is resulting from the changed swirl. For that reason it is also assigned to the other gain factors. It is important to notice that cavitation compliance (equation 2.7) and cavitation gain factor (equation 6.3) have the same definition. However, they describe different effects and consequently have different values. This is marked by the $*$ in equation 6.3. It has to be highlighted that for the different gain factors a time delay has to be included in the 1D model as proposed by Dörfler et al. [45]. As cavitation compliance and cavitation gain factor depend on pressure level but second one has a time delay while the former has not, this new proposed 1D model should be able to reproduce the physical mechanism of the full load instability.

For the determination of cavitation compliance and the different gain factors with 3D simulations, the different effects have to be identified separately. Mass flow gain factor and rotational speed gain factor can be determined by setting a constant pressure level at the outlet and varying the discharge at the inlet or the rotational speed, respectively. As both, cavitation compliance and cavitation gain factor, are a result of pressure variations, the two effects must be separated. This can be achieved by

[2]Analog to section 2.5 the index DT is omitted for the following equations. Consequently, V_c denotes the cavitation volume in the draft tube.

suppressing cavitation in the runner (Fe0inRU) for C_c or draft tube (Fe0inDT) for ψ, respectively.

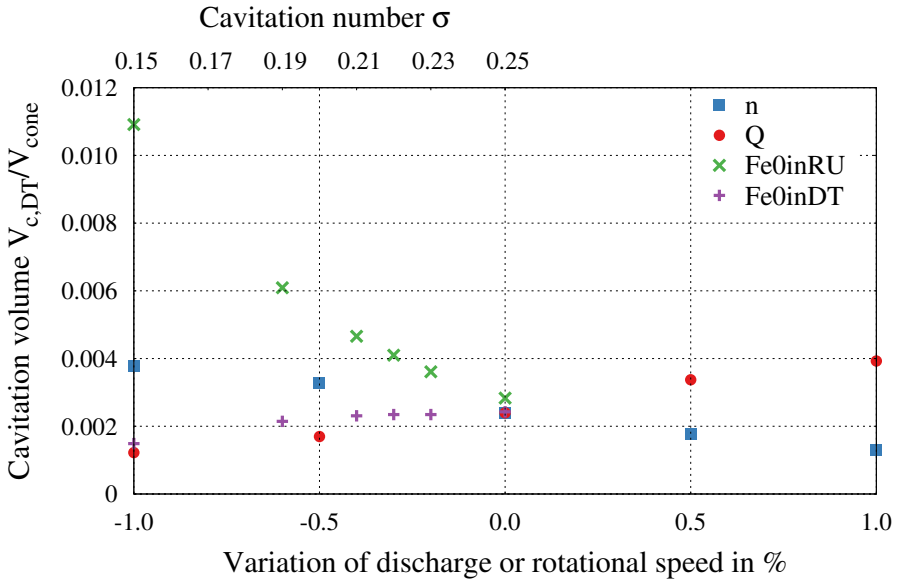

Figure 6.6: Cavitation volume in draft tube for variation of discharge, rotational speed or cavitation number. For variation of cavitation number in one case cavitation in the runner has been suppressed (Fe0inRU), while for the other case cavitation has been suppressed in the draft tube (Fe0inDT). For Fe0inDT a pseudo cavitation volume in the draft tube is presented that is scaled to have the same cavitation volume like no suppression of cavitation. Mesh 14M has been used for the simulations and all simulations have been performed steady state.

Exemplarily, the determination of χ, ϵ, ψ and C_c is shown for the operating point from chapter 5 (guide vane opening 28°). In figure 6.6, the cavitation volume in the draft tube is displayed for a variation of discharge, rotational speed, or cavitation number, respectively. All results are from steady state simulations with mesh 14M. For variation of Q and n the pressure level is set to $\sigma = 0.25$.

The change of cavitation volume in the draft tube due to variations of discharge or rotational speed, respectively, can be approximated by a linear behavior. Cavitation volume $V_{c,DT}$ increases with increasing discharge, while the same behavior can be found for decreasing rotational speed, which is in agreement with the explanations from section 6.4. It is conspicuous that a variation of Q and n result in the same change of $V_{c,DT}$, except of the sign of the variation. For variation of cavitation number no linear relation can be observed. With suppressed cavitation in the runner (Fe0inRU), $V_{c,DT}$ increases with decreasing σ. With decreasing cavitation number the cavitation volume in the draft tube increases stronger, which is probably a cause of increased diameter of the cavitating vortex rope.

For suppressed cavitation in the draft tube (Fe0inDT) a pseudo cavitation volume is displayed in figure 6.6. This pseudo cavitation volume is scaled to have the same cavitation volume $V_{c,DT}$ like for no suppression of cavitation. Down to $\sigma = 0.21$, the cavitation volume in the draft tube remains approximately constant. Further decreasing the cavitation number results in a reduction of the pseudo cavitation volume that becomes stronger with decreasing σ.

7 Conclusion and Outlook

In this thesis, the physical mechanism behind the full load instability in a Francis turbine has been investigated by means of numerical simulations. All simulations were performed at model scale. Due to the necessity to capture the interaction between cavitation regions in the runner and draft tube, two-phase simulations were conducted. In preliminary studies on simplified test cases it was shown that the homogeneous two-phase modeling approach is suitable for cavitation simulations and the inhomogeneous model has no added value. Investigations on the NACA0009 test case with a cavitating tip leakage vortex showed that an appropriate turbulence model has to be selected to capture the regions of vortex cavitation with reasonable agreement. For this test case, the SBES model, which is a state-of-the-art hybrid RANS-LES model, and the SST model with curvature correction showed the best results. However, the use of the SBES model resulted in unphysical oscillations for the Francis turbine and for that reason all investigations regarding the full load instability have been performed with the SST model with curvature correction.

The analysis of the full load instability was made in two steps. In the first step, simulations at six different cavitation numbers were performed of which the three highest pressure levels showed stable conditions while for the other pressure levels the full load instability developed. In the second step, the pressure at the draft tube outlet was gradually decreased from stable to unstable conditions. For both procedures similar observations could be made. During stable conditions, only minor oscillations of pressure and cavitation volume in the draft tube are present and the cavitation volume in the runner is of negligible size. Furthermore, the swirl number is similar for different cavitation numbers at stable conditions. In the range of the instability onset characteristically a small reduction of cavitation number results in a sudden increase of pressure and cavitation volume oscillations. Moreover, a cavitation region at the trailing edge of the runner blade forms that ranges from approximately midspan to the shroud.

All in all, the physical mechanism behind the full load instability can be traced back to three effects. Effect 1 represents the fact that the cavitation volume in the draft tube increases when the pressure is reduced. As pressure is traveling at the speed of sound,

which is infinite for incompressible simulations, this effect instantaneously affects the cavitation in the draft tube. This effect is irrespective of whether stable or unstable conditions are present. Effect 2 describes the behavior of the cavitation volume in the draft tube caused by changes of the cavitation volume in the runner. For a pressure reduction, the cavitation volume in the runner increases. When cavitation occurs on the suction side of the runner blade close to the trailing edge, the relative flow angle increases. This results in a changed velocity triangle that is characterized by reduced c_u, which in turn leads to a reduced swirl number. Finally, the reduced swirl results in a smaller cavitation volume in the draft tube. As the changed swirl has to travel with the flow from the runner outlet into the draft tube, it comes to a time delay at the relevant location of the vortex rope (plane 3) between the counteracting effects 1 and 2. This time delay is indispensable for the development of the full load instability as it is necessary for the formation of a self-oscillation. Since cavitation on the runner blades is not present or of negligible size for stable conditions, effect 2 becomes only relevant for unstable conditions. Furthermore, effect 3 is important for the formation of the full load instability. It describes the change of pressure that is caused by the cavitation volume oscillation. All in all, the existence of the three effects can result in the development of the full load instability. The findings demonstrate that this instability is a result of the interaction between cavitation in the runner and the draft tube. As could be shown by locally suppressing cavitation in the runner or draft tube, respectively, the instability does not develop when one of these regions is cavitation free.

A similar change of the velocity triangle at the runner outlet as described for effect 2 would be possible for either reduced discharge or increased rotational speed. However, the described mechanism is the most likely as only the occurrence of blade cavitation in combination with effect 3 guarantee the correct time delay at the relevant location of the vortex rope. Based on the findings of this thesis, an adopted 1D model has been proposed that can also consider the occurrence of blade cavitation. All in all, this thesis gives an in-depth explanation for the physical mechanism behind the full load instability. This knowledge combined with the adopted 1D model gives the opportunity to assess the risk of full load instability already in the design process and consequently facilitates the design of reliable turbines that can be used for a wide operating range.

Outlook

The present work reveals some deviations between simulation and measurement. For instance, the onset of the instability occurs at a different cavitation number. To reduce the deviations, it is recommended that future work takes into account effects that have not been considered due to simplifications. Consequently, it is advisable to implement a 1D-3D coupling that could take into account the discharge reduction in the period of when the cavitation volume collapses. This would eliminate the uncertainty that is caused by the prescription of a constant mass flow at the inlet boundary condition. Furthermore, increasing the accuracy of the simulations is promising to reduce the deviations between simulation and experiment. This could be possible with the development of new advanced turbulence models that are specially developed for multi-phase flows. Moreover, the development of new cavitation models might increase simulation accuracy. Finally, it is worthwhile to include compressibility in the simulations because the speed of sound is reduced due to the occurrence of cavitation. As the consideration of compressibility reduces the time delay between effect 1 and 2 this might lead to a delayed instability onset in the simulation and consequently decrease deviations to the experiments.

Within this thesis, the transferability to other operating points has been proved. However, one further step would be to validate the described mechanism on a different turbine that also shows the occurrence of the full load instability. This would verify the universality of the physical mechanism.

The understanding of the development of the full load instability enables future research to investigate measures that suppress the occurrence of the instability, which would allow an increased operating range. For example, a changed design of the runner blades appears promising. Furthermore, the adopted 1D modeling gives the opportunity to perform stability analysis of a turbine and detect regions that are critical for operation. However, this new proposed 1D modeling needs some discussion in the community in terms of applicability.

Bibliography

[1] Abdel-Maksoud, M.; Hänel, D.; Lantermann, U.: Modeling and computation of cavitation in vortical flow, *International Journal of Heat and Fluid Flow*, 31(6):1065–1074, 2010

[2] Acosta, A.J.: *A note on partial cavitation of flat plate hydrofoils*, Report E-19.9, California Institute of Technology, 1955

[3] Airy, G.B.: On certain Conditions under which a Perpetual Motion is possible, *Trans. Cambridge Phil. Soc.*, 3:369-372, 1830

[4] Alligné, S.: *Forced and self oscillations of hydraulic systems induced by cavitation vortex rope of Francis turbines*, Ph.D. thesis, École Polytechnique Fédérale de Lausanne, 2011

[5] Alligné, S.; Maruzewski, P.; Dinh, T.; Wang, B.; Fedorov, A.; Iosfin, J.; Avellan, F.: Prediction of a Francis turbine prototype full load instability from investigations on the reduced scale model, in: *IOP Conference Series: Earth and Environmental Science*, vol. 12, p. 012025, IOP Publishing, 2010

[6] Alligne, S.; Nicolet, C.; Tsujimoto, Y.; Avellan, F.: Cavitation surge modelling in Francis turbine draft tube, *Journal of Hydraulic Research*, 52(3):399–411, 2014

[7] ANSYS® CFX: *Release 18.1, Solver Modeling Guide, ANSYS, Inc.*, 2017

[8] ANSYS® CFX: *Release 18.1, Solver Theory Guide, ANSYS, Inc.*, 2017

[9] ANSYS® Fluent: *Release 17.0, Theory Guide, ANSYS, Inc.*, 2017

[10] Arakeri, V.H.: Viscous effects on the position of cavitation separation from smooth bodies, *Journal of Fluid Mechanics*, 68(04):779–799, 1975

[11] Argyropoulos, C.; Markatos, N.: Recent advances on the numerical modelling of turbulent flows, *Applied Mathematical Modelling*, 39(2):693–732, 2015

[12] Arndt, R.; Arakeri, V.; Higuchi, H.: Some observations of tip-vortex cavitation, *Journal of fluid mechanics*, 229:269–289, 1991

[13] Arndt, R.E.: Cavitation in vortical flows, *Annual Review of Fluid Mechanics*, 34(1):143–175, 2002

[14] Avellan, F.: Introduction to cavitation in hydraulic machinery, in: *The 6th International Conference on Hydraulic Machinery and Hydrodynamics, Timisoara, Romania*, 2004

[15] Belahadji, B.; Franc, J.P.; Michel, J.M.: Cavitation in the rotational structures of a turbulent wake, *Journal of Fluid Mechanics*, 287:383–403, 1995

[16] Billah, K.Y.; Scanlan, R.H.: Resonance, Tacoma Narrows bridge failure, and undergraduate physics textbooks, *American Journal of Physics*, 59(2):118–124, 1991

[17] Bilus, I.; Morgut, M.; Nobile, E.: Simulation of sheet and cloud cavitation with homogenous transport models, *International Journal of Simulation Modelling*, 12(2):94–106, 2013

[18] Blake, W.K.: *Mechanics of Flow-Induced Sound and Vibration, Volume 1: General Concepts and Elementary Sources*, Academic Press, 1986

[19] Bouziad, Y.A.: *Physical modelling of leading edge cavitation: computational methodologies and application to hydraulic machinery*, Ph.D. thesis, École Polytechnique Fédérale de Lausanne, 2006

[20] Braisted, D.; Brennen, C.: Auto-oscillation of cavitating inducers, *Polyphase Flow and Transport Technology*, pp. 157–166, 1980

[21] Braun, O.; Taruffi, A.; Ruchonnet, N.; Müller, A.; Avellan, F.: Numerical investigations of the dynamics of the full load vortex rope in a Francis turbine., in: *5th International Workshop on Cavitation and Dynamic Problems in Hydraulic Machinery and Systems*, no. EPFL-TALK-203792, 2013

[22] Brennen, C.; Acosta, A.: The Dynamic Transfer Function for a Cavitating Inducer, *Journal of Fluids Engineering*, 98(2):182–191, 1976

[23] Brennen, C.E.: *Hydrodynamics of pumps*, Concepts ETI Inc. and Cambridge University Press, 1994

[24] Brennen, C.E.: *Cavitation and bubble dynamics*, Cambridge University Press, 1995

[25] Brennen, C.E.: *Fundamentals of multiphase flow*, Cambridge University Press, 2005

[26] Callenaere, M.; Franc, J.P.; Michel, J.M.; Riondet, M.: The cavitation instability induced by the development of a re-entrant jet, *Journal of Fluid Mechanics*, 444:223–256, 2001

[27] Castro, A.M.: *Polydispersed bubbly flow model for ship hydrodynamics with application to Athena R/V*, Ph.D. thesis, University of Iowa, 2011

[28] Celebioglu, K.; Altintas, B.; Aradag, S.; Tascioglu, Y.: Numerical research of cavitation on Francis turbine runners, *International Journal of Hydrogen Energy*, 42(28):17771–17781, 2017

[29] Chen, C.; Nicolet, C.; Yonezawa, K.; Farhat, M.; Avellan, F.; Miyagawa, K.; Tsujimoto, Y.: Experimental study and numerical simulation of cavity oscillation in a conical diffuser, *International Journal of Fluid Machinery and Systems*, 3(1):91–101, 2010

[30] Chen, C.; Nicolet, C.; Yonezawa, K.; Farhat, M.; Avellan, F.; Miyagawa, K.; Tsujimoto, Y.: Experimental study and numerical simulation of cavity oscillation in a diffuser with swirling flow, *International Journal of Fluid Machinery and Systems*, 3(1):80–90, 2010

[31] Chen, C.; Nicolet, C.; Yonezawa, K.; Farhat, M.; Avellan, F.; Tsujimoto, Y.: One-dimensional analysis of full load draft tube surge, *Journal of Fluids Engineering*, 130(4):041106, 2008

[32] Chen, C.; Nicolet, C.; Yonezawa, K.; Farhat, M.; Avellan, F.; Tsujimoto, Y.: One-dimensional analysis of full load draft tube surge considering the finite sound velocity in the penstock, *International Journal of Fluid Machinery and Systems*, 2(3):260–268, 2009

[33] Cheung, S.C.; Yeoh, G.H.; Tu, J.: A review of population balance modelling for isothermal bubbly flows, *The Journal of Computational Multiphase Flows*, 1(2):161–199, 2009

[34] Chirkov, D.; Avdyushenko, A.; Panov, L.; Bannikov, D.; Cherny, S.; Skorospelov, V.; Pylev, I.: CFD simulation of pressure and discharge surge in Francis turbine at off-design conditions, in: *IOP Conference Series: Earth and Environmental Science*, vol. 15, p. 032038, IOP Publishing, 2012

[35] Chirkov, D.; Cherny, S.; Scherbakov, P.; Zakharov, A.: Evaluation of range of stable operation of hydraulic turbine based on 1D-3D model of full load pulsations, *Proceedings of 6th IAHR Working Group on Cavitation and dynamic problems in hydraulic machinery and systems*, pp. 177–184, 2015

[36] Chirkov, D.; Panov, L.; Cherny, S.; Pylev, I.: Numerical simulation of full load surge in Francis turbines based on three-dimensional cavitating flow model, in:

IOP Conference Series: Earth and Environmental Science, vol. 22, p. 032036, IOP Publishing, 2014

[37] Chirkov, D.; Scherbakov, P.; Cherny, S.; Zakharov, A.; Skorospelov, V.; Turuk, P.: Mitigation of self-excited oscillations at full load: CFD analysis of air admission and effects of runner design, in: *IOP Conference Series: Earth and Environmental Science*, vol. 49, p. 062025, IOP Publishing, 2016

[38] Conrad, P.; Weber, W.; Jung, A.: Deep Part Load Flow Analysis in a Francis Model Turbine by means of two-phase unsteady flow simulations, in: *Proceedings of the Hyperbole Conference, Porto, Portugal*, 2017

[39] Crowe, C.T.; Schwarzkopf, J.D.; Sommerfeld, M.; Tsuji, Y.: *Multiphase Flows with Droplets and Particles*, CRC Press, 2011

[40] d'Agostino, L.; Salvetti, M.V.: *Fluid dynamics of cavitation and cavitating turbopumps*, Springer Science & Business Media, 2008

[41] De Lange, D.; De Bruin, G.: Sheet cavitation and cloud cavitation, re-entrant jet and three-dimensionality, *Applied scientific research*, 58(1):91–114, 1997

[42] Decaix, J.; Balarac, G.; Dreyer, M.; Farhat, M.; Münch, C.: RANS and LES computations of the tip-leakage vortex for different gap widths, *Journal of Turbulence*, 16(4):309–341, 2015

[43] Decaix, J.; Balarac, G.; Münch, C.: Rans Computations of a Cavitating Tip Vortex, in: *Advances in Hydroinformatics*, pp. 519–529, Springer, 2016

[44] Decaix, J.; Müller, A.; Favrel, A.; Avellan, F.; Münch, C.: URANS Models for the Simulation of Full Load Pressure Surge in Francis Turbines Validated by Particle Image Velocimetry, *Journal of Fluids Engineering*, 139(12):121103, 2017

[45] Dörfler, P.; Keller, M.; Braun, O.: Francis full-load surge mechanism identified by unsteady 2-phase CFD, in: *IOP Conference Series: Earth and Environmental Science*, vol. 12, p. 012026, IOP Publishing, 2010

[46] Dörfler, P.; Sick, M.; Coutu, A.: *Flow-induced pulsation and vibration in hydroelectric machinery: Engineer's guidebook for planning, design and troubleshooting*, Springer, 2012

[47] Dörfler, P.K.: Evaluating 1D models for vortex-induced pulsation in Francis turbines, in: *3rd IAHR International Meeting of the Workgroup on Cavitation and Dynamic Problems in Hydraulic Machinery and Systems, Brno, Czech Republic, Oct*, pp. 14–16, 2009

[48] Dörfler, P.K.: Analysis of the Francis turbine upper-part-load pulsation Part II - Mechanism of self-excitation, in: *Proceedings of 29th IAHR Symposium on Hydraulic Machinery and Systems*, 2018

[49] Doujak, E.: Effects of increased solar and wind energy on hydro plant operation, *Hydro Review Worldwide*, 2:28–31, 2014

[50] Dowling, A.P.; Ffowcs Williams, J.: *Sound and sources of sound*, Horwood, 1983

[51] Drew, D.A.; Passman, S.L.: *Theory of multicomponent fluids*, vol. 135, Springer Science & Business Media, 1999

[52] Dreyer, M.: *Mind The Gap: Tip Leakage Vortex Dynamics and Cavitation in Axial Turbines*, Ph.D. thesis, École Polytechnique Fédérale De Lausanne, 2015

[53] Dreyer, M.; Decaix, J.; Münch-Alligné, C.; Farhat, M.: Mind the gap - tip leakage vortex in axial turbines, in: *IOP Conference Series: Earth and Environmental Science*, vol. 22, p. 052023, IOP Publishing, 2014

[54] Dreyer, M.; Decaix, J.; Münch-Alligné, C.; Farhat, M.: Mind the gap: a new insight into the tip leakage vortex using stereo-PIV, *Experiments in fluids*, 55(11):1849, 2014

[55] Duttweiler, M.E.; Brennen, C.E.: Surge instability on a cavitating propeller, *Journal of Fluid Mechanics*, 458:133–152, 2002

[56] Escaler, X.; Egusquiza, E.; Farhat, M.; Avellan, F.; Coussirat, M.: Detection of cavitation in hydraulic turbines, *Mechanical systems and signal processing*, 20(4):983–1007, 2006

[57] Escaler, X.; Ekanger, J.V.; Francke, H.H.; Kjeldsen, M.; Nielsen, T.K.: Detection of draft tube surge and erosive blade cavitation in a full-scale Francis turbine, *Journal of Fluids Engineering*, 137(1):011103, 2015

[58] Escaler, X.; Roig, R.; Hidalgo, V.: Sensitivity Analysis of Zwart-Gerber-Belamri Model Parameters on the Numerical Simulation of Francis Runner Cavitation, in: *Proceedings of the 10th International Symposium on Cavitation (CAV2018)*, ASME Press, Baltimore, USA, 2018

[59] Favrel, A.; Landry, C.; Müller, A.; Yamamoto, K.; Avellan, F.: Hydro-acoustic resonance behavior in presence of a precessing vortex rope: observation of a lock-in phenomenon at part load Francis turbine operation, in: *IOP Conference Series: Earth and Environmental Science*, vol. 22, p. 032035, IOP Publishing, 2014

[60] Favrel, A.; Müller, A.; Landry, C.; Yamamoto, K.; Avellan, F.: LDV survey of cavitation and resonance effect on the precessing vortex rope dynamics in the draft tube of Francis turbines, *Experiments in Fluids*, 57(11):168, 2016

[61] Ferziger, J.H.; Peric, M.: *Numerische Strömungsmechanik*, Springer-Verlag, 2008

[62] Fitzpatrick, H.; Strasberg, M.: Hydrodynamic sources of sound, in: *Proceedings of the First Symposium on Naval Hydrodynamics*, pp. 241–280, 1956

[63] Flemming, F.; Foust, J.; Koutnik, J.; Fisher, R.K.: Overload surge investigation using CFD data, *International journal of fluid machinery and systems*, 2(4):315–323, 2009

[64] Franc, J.P.: Partial cavity instabilities and re-entrant jet, in: *Proceedings of the 4th International Symposium on Cavitation*, 2001

[65] Franc, J.P.; Michel, J.M.: *Fundamentals of cavitation*, vol. 76, Springer Science & Business Media, 2005

[66] Friedrichs, J.; Kosyna, G.: Rotating cavitation in a centrifugal pump impeller of low specific speed, *Transactions-American Society of Mechanical Engineers Journal of Fluids Engineering*, 124(2):356–362, 2002

[67] Gohil, P.P.; Saini, R.: Effect of temperature, suction head and flow velocity on cavitation in a Francis turbine of small hydro power plant, *Energy*, 93:613–624, 2015

[68] Gopalan, S.; Katz, J.: Flow structure and modeling issues in the closure region of attached cavitation, *Physics of Fluids*, 12(4):895–911, 2000

[69] Gore, R.; Crowe, C.T.: Effect of particle size on modulating turbulent intensity, *International Journal of Multiphase Flow*, 15(2):279–285, 1989

[70] Gosman, A.; Lekakou, C.; Politis, S.; Issa, R.; Looney, M.: Multidimensional modeling of turbulent two-phase flows in stirred vessels, *AIChE Journal*, 38(12):1946–1956, 1992

[71] Guo, Q.; Zhou, L.; Wang, Z.: Numerical evaluation of the clearance geometries effect on the flow field and performance of a hydrofoil, *Renewable Energy*, 99:390–397, 2016

[72] Gupta, A.; Roy, S.: Euler-Euler simulation of bubbly flow in a rectangular bubble column: experimental validation with Radioactive Particle Tracking, *Chemical Engineering Journal*, 225:818–836, 2013

[73] Habchi, C.: A Gibbs Energy Relaxation (GERM) Model for Cavitation Simulation, *Atomization and Sprays*, 25(4), 2015

[74] Habchi, C.; Bohbot, J.; Schmid, A.; Herrmann, K.: A comprehensive Two-Fluid Model for Cavitation and Primary Atomization Modelling of liquid jets-Application to a large marine Diesel injector, in: *Journal of Physics: Conference Series*, vol. 656, p. 012084, IOP Publishing, 2015

[75] Houde, S.; Iliescu, M.S.; Fraser, R.; Lemay, S.; Ciocan, G.D.; Deschênes, C.: Experimental and numerical analysis of the cavitating part load vortex dynamics of low-head hydraulic turbines, in: *ASME-JSME-KSME 2011 Joint Fluids Engineering Conference*, pp. 171–182, American Society of Mechanical Engineers, 2011

[76] IEC 60193: *Hydraulic Turbines, Storage Pumps and Pump-Turbines-Model Acceptance Tests*, 1999

[77] Iga, Y.; Hashizume, K.; Yoshida, Y.: Numerical analysis of three types of cavitation surge in cascade, *Journal of Fluids Engineering*, 133(7):071102, 2011

[78] Iliescu, M.S.; Ciocan, G.D.; Avellan, F.: Analysis of the cavitating draft tube vortex in a Francis turbine using particle image velocimetry measurements in two-phase flow, *Journal of Fluids Engineering*, 130(2):021105, 2008

[79] Ishii, M.: Thermo-Fluid Theory of Two-Phase Flows, *Eyrolles, Paris*, 1975

[80] Ishii, M.; Hibiki, T.: *Thermo-Fluid Dynamics of Two-Phase Flow*, Springer Science & Business Media, 2010

[81] Ishii, M.; Zuber, N.: Drag coefficient and relative velocity in bubbly, droplet or particulate flows, *AIChE Journal*, 25(5):843–855, 1979

[82] Jackson, R.B.; Quéré, C.L.; Andrew, R.M.; Canadell, J.G.; Peters, G.P.; Roy, J.; Wu, L.: Warning signs for stabilizing global CO_2 emissions, *Environmental Research Letters*, 12(11):110202, 2017

[83] Jacob, T.; Prénat, J.E.: Francis turbine surge: discussion and data base, in: *Hydraulic Machinery and Cavitation*, pp. 855–864, Springer, 1996

[84] Jakobsen, H.A.: *Chemical reactor modeling: multiphase reactive flows*, Springer Science & Business Media, 2014

[85] Jenkins, A.: Self-oscillation, *Physics Reports*, 525(2):167–222, 2013

[86] Ji, B.; Luo, X.; Wu, Y.; Peng, X.; Duan, Y.: Numerical analysis of unsteady cavitating turbulent flow and shedding horse-shoe vortex structure around a twisted hydrofoil, *International Journal of Multiphase Flow*, 51:33–43, 2013

[87] Ji, B.; Peng, X.; Long, X.; Luo, X.; Wu, Y.: Numerical evaluation of cavitation shedding structure around 3D Hydrofoil: Comparison of PANS, LES and RANS results with experiments, in: *Journal of Physics: Conference Series*, vol. 656, p. 012127, IOP Publishing, 2015

[88] Jošt, D.; Skerlavaj, A.; Morgut, M.; Nobile, E.: Numerical Prediction of Cavitation Vortex Rope in a Draft Tube of a Francis Turbine with Standard and Calibrated Cavitation Model, in: *Proceedings of the Hyperbole Conference, Porto, Portugal*, 2017

[89] Junginger, B.; Riedelbauch, S.: Numerical Analysis of a Propeller Turbine Operated in Part Load Conditions, *High Performance Computing in Science and Engineering ' 17: Transactions of the High Performance Computing Center*, pp. 355-368, 2018

[90] Kiceniuk, T.: A Two-Dimensional Working Section for the High-Speed Water Tunnel at the California Institute of Technology, 1964

[91] Kirschner, O.: *Experimentelle Untersuchung des Wirbelzopfes im geraden Saugrohr einer Modell-Pumpturbine*, Ph.D. thesis, Universität Stuttgart, Germany, 2011

[92] Koop, A.H.: *Numerical simulation of unsteady three-dimensional sheet cavitation*, Ph.D. thesis, University of Twente, Enschede, 2008

[93] Koutnik, J.; Krüger, K.; Pochyly, F.; Rudolf, P.; Haban, V.: On cavitating vortex rope form stability during Francis turbine part load operation, in: *IAHR International Meeting of the Workgroup on Cavitation and Dynamic Problems in Hydraulic Machinery and Systems, Barcelona, Spain*, 2006

[94] Koutnik, J.; Nicolet, C.; Schohl, G.A.; Avellan, F.: Overload surge event in a pumped-storage power plant, in: *Proceedings of the 23rd IAHR Symposium on Hydraulic Machinery and Systems*, no. LMH-CONF-2007-007, 2006

[95] Krappel, T.; Ruprecht, A.; Riedelbauch, S.: Turbulence Resolving Flow Simulations of a Francis Turbine with a Commercial CFD Code, in: *High Performance Computing in Science and Engineering '15: Transactions of the High Performance Computing Center, Stuttgart (HLRS) 2015*, ed. Nagel, W.; Kröner, D.; Resch, M., pp. 421-433, Springer International Publishing, 2015

[96] Krepper, E.; Lucas, D.; Prasser, H.M.: On the modelling of bubbly flow in vertical pipes, *Nuclear Engineering and Design*, 235(5):597–611, 2005

[97] Kroner, N.; Bérubé, R.: Maintaining power grid reliability through individual unit stability, *Hydro Vision*, pp. 1–10, 2008

[98] Kunz, R.F.; Boger, D.A.; Chyczewski, T.S.; Stinebring, D.; Gibeling, H.; Govindan, T.: Multi-phase CFD analysis of natural and ventilated cavitation about submerged bodies, in: *Proceedings of the 3rd ASME/JSME Joint Fluids Engineering Conference*, San Francisco, USA, 1999

[99] Kurosawa, S.; Lim, S.; Enomoto, Y.: Virtual model test for a Francis turbine, in: *IOP Conference Series: Earth and Environmental Science*, vol. 12, p. 012063, IOP Publishing, 2010

[100] Landry, C.; Favrel, A.; Müller, A.; Nicolet, C.; Yamamoto, K.; Avellan, F.: Experimental investigation of the local wave speed in a draft tube with cavitation vortex rope, in: *IOP conference series: earth and environmental science*, vol. 22, p. 032037, IOP Publishing, 2014

[101] Le, Q.; Franc, J.P.; Michel, J.: Partial cavities: global behavior and mean pressure distribution, *Transactions-American Society of Mechanical Engineers Journal of Fluids Engineering*, 115:243–243, 1993

[102] Legendre, D.; Magnaudet, J.: The lift force on a spherical bubble in a viscous linear shear flow, *Journal of Fluid Mechanics*, 368:81–126, 1998

[103] Leger, A.T.; Ceccio, S.: Examination of the flow near the leading edge of attached cavitation. Part 1. Detachment of two-dimensional and axisymmetric cavities, *Journal of Fluid Mechanics*, 376:61–90, 1998

[104] Liu, J.; Liu, S.; Wu, Y.; Jiao, L.; Wang, L.; Sun, Y.: Numerical investigation of the hump characteristic of a pump–turbine based on an improved cavitation model, *Computers & Fluids*, 68:105–111, 2012

[105] Luo, H.; Svendsen, H.F.: Theoretical model for drop and bubble breakup in turbulent dispersions, *AIChE Journal*, 42(5):1225–1233, 1996

[106] Luo, X.w.; Bin, J.; Tsujimoto, Y.: A review of cavitation in hydraulic machinery, *Journal of Hydrodynamics, Ser. B*, 28(3):335–358, 2016

[107] Maeda, M.; Yamaguchi, H.; Kato, H.: Laser holography measurement of bubble population in cavitation cloud on a foil section, *Cavitation 91, ASME-FED*, 116:67-75, 1991

[108] Magnoli, M.; Maiwald, M.: Influence of Hydraulic Design on Stability and on Pressure Pulsations in Francis Turbines at Overload, Part Load and Deep Part

Load based on Numerical Simulations and Experimental Model Test Results, in: *IOP Conference Series: Earth and Environmental Science*, vol. 22, p. 032013, IOP Publishing, 2014

[109] Magnoli, M.V.: *Numerical simulation of pressure oscillations in large Francis turbines at partial and full load operating conditions and their effects on the runner structural behaviour and fatigue life*, Ph.D. thesis, Technische Universität München, 2014

[110] Menter, F.; Esch, T.: Elements of industrial heat transfer predictions, in: *Proceedings of the 16th Brazilian Congress of Mechanical Engineering (COBEM)*, Uberlandia, Brazil, 2001

[111] Menter, F.R.: Two-equation eddy-viscosity turbulence models for engineering applications, *AIAA journal*, 32(8):1598–1605, 1994

[112] Menter, F.R.: Best practice: Scale-resolving simulations in ANSYS CFD - Version 2.0, *ANSYS Germany GmbH*, pp. 1–75, 2015

[113] Menter, F.R.: Stress-Blended Eddy Simulation (SBES) - A new Paradigm in hybrid RANS-LES Modeling, in: *Proceedings of the 6th HRLM Symposium*, Strasbourg, France, 2016

[114] Morel, C.: *Mathematical modeling of disperse two-phase flows*, Springer, 2015

[115] Morgut, M.; Jošt, D.; Nobile, E.; Škerlavaj, A.: Numerical predictions of the turbulent cavitating flow around a marine propeller and an axial turbine, in: *Journal of Physics: Conference Series*, vol. 656, p. 012066, IOP Publishing, 2015

[116] Morgut, M.; Nobile, E.: Numerical predictions of cavitating flow around model scale propellers by CFD and advanced model calibration, *International Journal of Rotating Machinery*, 2012(618180), 2012

[117] Morgut, M.; Nobile, E.; Biluš, I.: Comparison of mass transfer models for the numerical prediction of sheet cavitation around a hydrofoil, *International Journal of Multiphase Flow*, 37(6):620–626, 2011

[118] Mössinger, P.; Conrad, P.; Jung, A.: Transient two-phase CFD simulation of overload pressure pulsation in a prototype sized Francis turbine considering the waterway dynamics, in: *IOP Conference Series: Earth and Environmental Science*, vol. 22, p. 032033, IOP Publishing, 2014

[119] Mössinger, P.; Jung, A.: Transient two-phase CFD simulation of overload operating conditions and load rejection in a prototype sized Francis turbine, in: *IOP Conference Series: Earth and Environmental Science*, vol. 49, p. 092003, IOP Publishing, 2016

[120] Motycak, L.; Skotak, A.; Kupcik, R.: Kaplan turbine tip vortex cavitation–analysis and prevention, in: *IOP Conference Series: Earth and Environmental Science*, vol. 15, p. 032060, IOP Publishing, 2012

[121] Müller, A.: *Physical Mechanisms governing Self-Excited Pressure Oscillations in Francis Turbines*, Ph.D. thesis, École Polytechnique Fédérale de Lausanne, 2014

[122] Müller, A.; Bullani, A.; Dreyer, M.; Roth, S.; Favrel, A.; Landry, C.; Avellan, F.: Interaction of a pulsating vortex rope with the local velocity field in a Francis turbine draft tube, in: *IOP Conference Series: Earth and Environmental Science*, vol. 15, p. 032040, IOP Publishing, 2012

[123] Müller, A.; Favrel, A.; Landry, C.; Avellan, F.: Fluid–structure interaction mechanisms leading to dangerous power swings in Francis turbines at full load, *Journal of Fluids and Structures*, 69:56–71, 2017

[124] Müller, A.; Favrel, A.; Landry, C.; Yamamoto, K.; Avellan, F.: On the physical mechanisms governing self-excited pressure surge in Francis turbines, in: *IOP Conference Series: Earth and Environmental Science*, vol. 22, p. 032034, IOP Publishing, 2014

[125] Müller, A.; Favrel, A.; Landry, C.; Yamamoto, K.; Avellan, F.: Experimental Hydro-Mechanical Characterization of Full Load Pressure Surge in Francis Turbines, in: *Journal of Physics: Conference Series*, vol. 813, p. 012018, IOP Publishing, 2017

[126] Müller, A.; Yamamoto, K.; Alligné, S.; Yonezawa, K.; Tsujimoto, Y.; Avellan, F.: Measurement of the self-oscillating vortex rope dynamics for hydroacoustic stability analysis, *Journal of Fluids Engineering*, 138(2):021206, 2016

[127] Ničeno, B.; Boucker, M.; Smith, B.: Euler-Euler Large Eddy Simulation of a Square Cross-Sectional Bubble Column Using the Neptune_CFD Code, *Science and Technology of Nuclear Installations*, 2009(410272), 2008

[128] Nicolet, C.; Zobeiri, A.; Maruzewski, P.; Avellan, F.: On the upper part load vortex rope in Francis turbine: Experimental investigation, in: *IOP Conference*

Series: Earth and Environmental Science, vol. 12, p. 012053, IOP Publishing, 2010

[129] Papula, L.: *Mathematische Formelsammlung für Ingenieure und Naturwissenschaftler*, Springer, 2009

[130] Piomelli, U.: Large-eddy and direct simulation of turbulent flows, *Report of Department of Mechanical Engineering, University of Maryland, USA*, 2001

[131] Prenat, J.E.; Jacob, T.: Comportement à forte charge d'un modèle de turbine Francis et effets d'échelle, in: *Proceedings of the 13th IAHR Symposium, section on hydraulic machinery and cavitaion: Progress in Technology*, vol. 2, Montréal, Canada, 1986

[132] Presas, A.; Valentin, D.; Egusquiza, E.; Valero, C.: Detection and analysis of part load and full load instabilities in a real Francis turbine prototype, in: *Journal of Physics: Conference Series*, vol. 813, p. 012038, IOP Publishing, 2017

[133] Prince, M.J.; Blanch, H.W.: Bubble coalescence and break-up in air-sparged bubble columns, *AIChE Journal*, 36(10):1485–1499, 1990

[134] Rheingans, W.: Power swings in hydroelectric power plants, *Trans. ASME*, 62(3):171–184, 1940

[135] Rockström, J.; Gaffney, O.; Rogelj, J.; Meinshausen, M.; Nakicenovic, N.; Schellnhuber, H.J.: A roadmap for rapid decarbonization, *Science*, 355(6331):1269–1271, 2017

[136] Rusche, H.: *Computational fluid dynamics of dispersed two-phase flows at high phase fractions*, Ph.D. thesis, Imperial College London (University of London), 2003

[137] Rzehak, R.; Krepper, E.: Euler-Euler simulation of mass-transfer in bubbly flows, *Chemical Engineering Science*, 155:459–468, 2016

[138] Sato, Y.; Sekoguchi, K.: Liquid velocity distribution in two-phase bubble flow, *International Journal of Multiphase Flow*, 2(1):79–95, 1975

[139] Saurel, R.; Lemetayer, O.: A multiphase model for compressible flows with interfaces, shocks, detonation waves and cavitation, *Journal of Fluid Mechanics*, 431:239–271, 2001

[140] Schiller, L.: Über die grundlegenden Berechnungen bei der Schwerkraftaufbereitung, *Zeitschrift des Vereines Deutscher Ingenieure*, 77:318–321, 1933

[141] Schlichting, H.: *Grenzschicht-Theorie*, Braun Verlag, 1951

[142] Schmidt, H.: *Entwicklung eines Analyseverfahrens zur Kavitationsdetektion und Lokalisierung in hydraulischen Strömungsmaschinen*, Ph.D. thesis, Universität Stuttgart, Germany, 2019

[143] Schnerr, G.H.; Sauer, J.: Physical and numerical modeling of unsteady cavitation dynamics, in: *Proceedings of the Fourth international conference on multiphase flow*, vol. 1, New Orleans, USA, 2001

[144] Shen, Y.; Dimotakis, P.E.: The influence of surface cavitation on hydrodynamic forces, in: *Proceedings of the 22nd American Towing Tank Conference*, 1989

[145] Shi, J.M.; Rohde, U.; Prasser, H.M.: *Turbulent Dispersion of Bubbles in Poly-dispersed Gas Liquid Flows in a Vertical Pipe*, Technical Report FZD-487, Forschungszentrum Dresden Rossendorf, 2007

[146] Shi, J.M.; Zwart, P.; Frank, T.; Rohde, U.; Prasser, H.M.: Development of a multiple velocity multiple size group model for poly-dispersed multiphase flows, *Annual Report*, 2004

[147] Singhal, A.K.; Athavale, M.M.; Li, H.; Jiang, Y.: Mathematical basis and validation of the full cavitation model, *Transactions-American Society of Mechanical Engineers Journal of Fluids Engineering*, 124(3):617–624, 2002

[148] Smirnov, P.E.; Menter, F.R.: Sensitization of the SST Turbulence Model to Rotation and Curvature by Applying the Spalart-Shur Correction Term, *Journal of Turbomachinery*, 131(4):041010, 2009

[149] Sommerfeld, M.; Van Wachem, B.; Oliemans, R.: *Best practice guidelines for computational fluid dynamics of dispersed multi-phase flows*, European Research Community on Flow, Turbulence and Combustion (ERCOFTAC), 2008

[150] Spalart, P.; Shur, M.: On the sensitization of turbulence models to rotation and curvature, *Aerospace Science and Technology*, 1(5):297–302, 1997

[151] Sridhar, G.; Katz, J.: Drag and lift forces on microscopic bubbles entrained by a vortex, *Physics of Fluids*, 7(2):389–399, 1995

[152] Stocker, T.: *Climate change 2013: the physical science basis: Working Group I contribution to the Fifth assessment report of the Intergovernmental Panel on Climate Change*, Cambridge University Press, 2014

[153] Strasberg, M.: The pulsation frequency of nonspherical gas bubbles in liquids, *The Journal of the Acoustical Society of America*, 25(3):536–537, 1953

[154] Strasberg, M.: Gas bubbles as sources of sound in liquids, *The Journal of the Acoustical Society of America*, 28(1):20–26, 1956

[155] Teske, S.; Sawyer, S.; Schäfer, O.; Pregger, T.; Simon, S.; Naegler, T.; et al.: *Energy [r]evolution - A sustainable world energy outlook 2015*, Available online at: https://www.greenpeace.de/presse/publikationen/energy-revolution (accessed 11 March 2019), 2015

[156] Tomiyama, A.; Tamai, H.; Zun, I.; Hosokawa, S.: Transverse migration of single bubbles in simple shear flows, *Chemical Engineering Science*, 57(11):1849–1858, 2002

[157] Trivedi, C.; Gandhi, B.; Michel, C.J.: Effect of transients on Francis turbine runner life: a review, *Journal of Hydraulic Research*, 51(2):121–132, 2013

[158] Tsujimoto, Y.; Kamijo, K.; Brennen, C.E.: Unified treatment of flow instabilities of turbomachines, *Journal of Propulsion and Power*, 17(3):636–643, 2001

[159] Tsujimoto, Y.; Yoshida, Y.; Maekawa, Y.; Watanabe, S.; Hashimoto, T.: Observations of oscillating cavitation of an inducer, *Journal of fluids Engineering*, 119(4):775–781, 1997

[160] UNEP: *The Emissions Gap Report 2017: A UN Environment Synthesis Report*, Available online at: https://www.unenvironment.org/resources/emissions-gap-report-2017 (accessed 11 March 2019), 2017

[161] UNFCCC, Decision 1/CP.21: Adoption of the Paris Agreement, in: *Paris Climate Change Conference*, 2015

[162] Wack, J.; Riedelbauch, S.: Numerical simulations of the cavitation phenomena in a Francis turbine at deep part load conditions, *Journal of Physics: Conference Series*, 656(1):012074, 2015

[163] Wack, J.; Riedelbauch, S.: Two-phase simulations of the full load surge in Francis turbines, in: *IOP Conference Series: Earth and Environmental Science*, vol. 49, IOP Publishing, 2016

[164] Wack, J.; Riedelbauch, S.: Numerical simulation of a cavitating draft tube vortex rope in a Francis turbine at part load conditions for different σ-levels, *Journal of Physics: Conference Series*, 813(1):012019, 2017

[165] Wack, J.; Riedelbauch, S.: Application of Homogeneous and Inhomogeneous Two-Phase Models to a Cavitating Tip Leakage Vortex on a NACA0009 Hydrofoil, in: *Proceedings of the 10th International Symposium on Cavitation (CAV2018)*, ASME Press, Baltimore, USA, 2018

[166] Wack, J.; Riedelbauch, S.: Cavitation simulations of a tip leakage vortex for a NACA0009 hydrofoil and a Francis turbine at stable full load operating point, in: *High Performance Computing in Science and Engineering '18*, ed. Nagel, W.E.; Kröner, D.H.; Resch, M.M., pp. 351–365, Springer International Publishing, 2019

[167] Wack, J.; Riedelbauch, S.; Yamamoto, K.; Avellan, F.: Two-phase flow simulations of the inter-blade vortices in a Francis turbine, in: *Proceedings of the 9th International Conference on Multiphase Flow*, Florence, Italy, 2016

[168] Willis, R.: On the Mechanism of the Larynx, *Trans. Cambridge Phil. Soc.*, 4:323-352, 1833

[169] Wu, Y.; Liu, S.; Dou, H.S.; Zhang, L.: Simulations of unsteady cavitating turbulent flow in a Francis turbine using the RANS method and the improved mixture model of two-phase flows, *Engineering with Computers*, 27(3):235–250, 2011

[170] Yakubov, S.; Cankurt, B.; Abdel-Maksoud, M.; Rung, T.: Hybrid MPI/OpenMP parallelization of an Euler–Lagrange approach to cavitation modelling, *Computers & Fluids*, 80:365–371, 2013

[171] Yamamoto, K.: *Hydrodynamics of Francis turbine operation at deep part load condition*, Ph.D. thesis, École Polytechnique Fédérale de Lausanne, 2017

[172] Yamamoto, K.; Müller, A.; Favrel, A.; Avellan, F.: Experimental evidence of inter-blade cavitation vortex development in Francis turbines at deep part load condition, *Experiments in Fluids*, 58(10):142, 2017

[173] Yamamoto, K.; Müller, A.; Favrel, A.; Landry, C.; Avellan, F.: Pressure measurements and high speed visualizations of the cavitation phenomena at deep part load condition in a Francis turbine, in: *IOP Conference Series: Earth and Environmental Science*, vol. 22, p. 022011, IOP Publishing, 2014

[174] Yamamoto, K.; Müller, A.; Favrel, A.; Landry, C.; Avellan, F.: Guide Vanes Embedded Visualization Technique For Investigating Francis Runner Inter-Blade Vortices At Deep Part Load Operation, in: *Proceedings of the 6th IAHR meeting of the IAHR Working Group Cavitation and dynamic problems*, pp. 323-330, Ljubljana, Slovenia, 2015

[175] Yamamoto, K.; Müller, A.; Favrel, A.; Landry, C.; Avellan, F.: Numerical and experimental evidence of the inter-blade cavitation vortex development at deep part load operation of a Francis turbine, in: *IOP Conference Series: Earth and Environmental Science*, vol. 49, p. 082005, IOP Publishing, 2016

[176] Yamoah, S.; Martínez-Cuenca, R.; Monrós, G.; Chiva, S.; Macián-Juan, R.: Numerical investigation of models for drag, lift, wall lubrication and turbulent dispersion forces for the simulation of gas–liquid two-phase flow, *Chemical Engineering Research and Design*, 98:17–35, 2015

[177] Yeoh, G.H.; Tu, J.: *Computational Techniques for Multi-Phase Flows*, Elsevier, 2010

[178] Yonezawa, K.; Konishi, D.; Miyagawa, K.; Avellan, F.; Doerfler, P.; Tsujimoto, Y.: Cavitation surge in a small model test facility simulating a hydraulic power plant, *International journal of fluid machinery and systems*, 5(4):152–160, 2012

[179] You, D.; Wang, M.; Moin, P.; Mittal, R.: Large-eddy simulation analysis of mechanisms for viscous losses in a turbomachinery tip-clearance flow, *Journal of Fluid Mechanics*, 586:177–204, 2007

[180] Zaisha, M.; Chao, Y.: Challenges in study of single particles and particle swarms, *Chinese Journal of Chemical Engineering*, 17(4):535–545, 2009

[181] Zhang, G.; Shi, W.; Zhou, L.; Zhang, D.: Effect of the Maximum Density Ratio Between Liquid and Vapor on Cavitating Simulation, *American Journal of Engineering and Applied Sciences*, 8(1):119, 2015

[182] Zuo, Z.; Liu, S.; Liu, D.; Qin, D.; Wu, Y.: Numerical Predictions of the Incipient and Developed Interblade Vortex Lines of a Model Francis Turbine by Cavitation Calculations, *Advances in Mechanical Engineering*, 5:397583, 2013

[183] Zwart, P.J.; Gerber, A.G.; Belamri, T.: A Two-Phase Flow Model for Predicting Cavitation Dynamics, in: *Proceedings of the fifth international conference on multiphase flow*, Yokohama, Japan, 2004

A Additional Results NACA0009

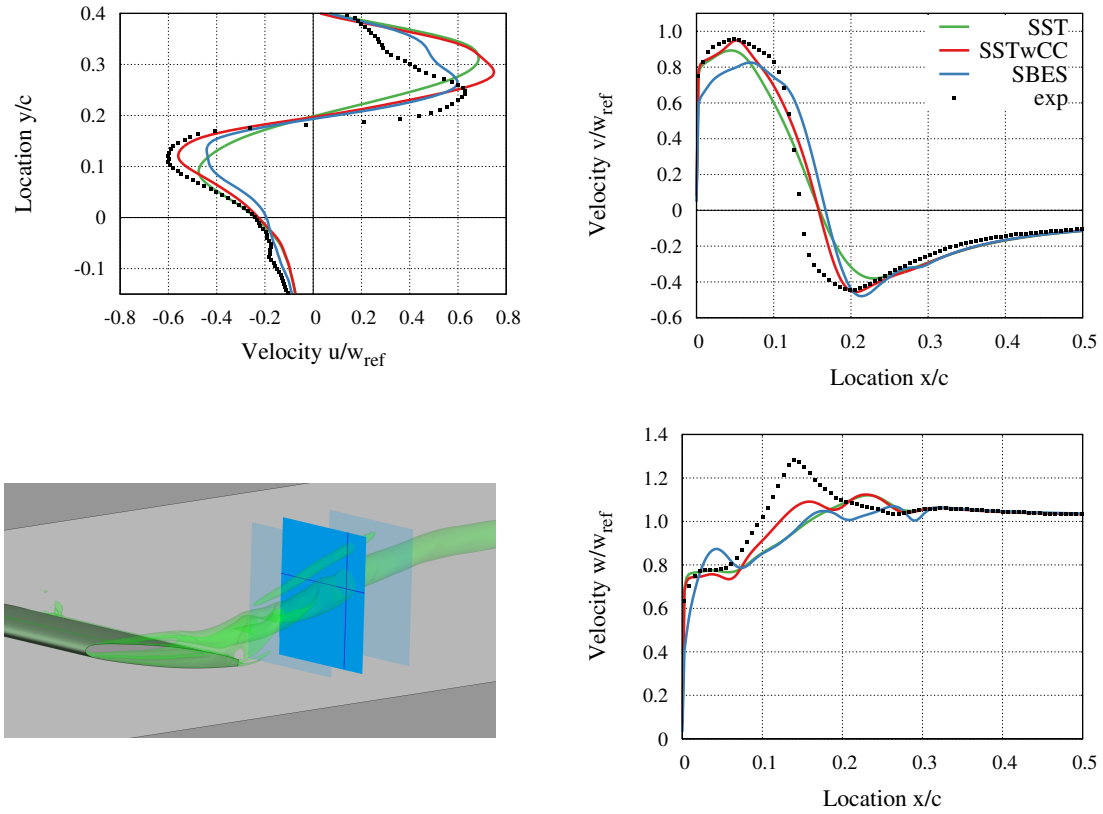

Figure A.1: Distribution of averaged u-, v- and w-component of the velocity along line in x- or y-direction, respectively, at measurement plane $z/c = 1.2$. The lines are located at $x/c = 0.126$ and $y/c = 0.181$. Experiments were performed by Dreyer et al. [54].

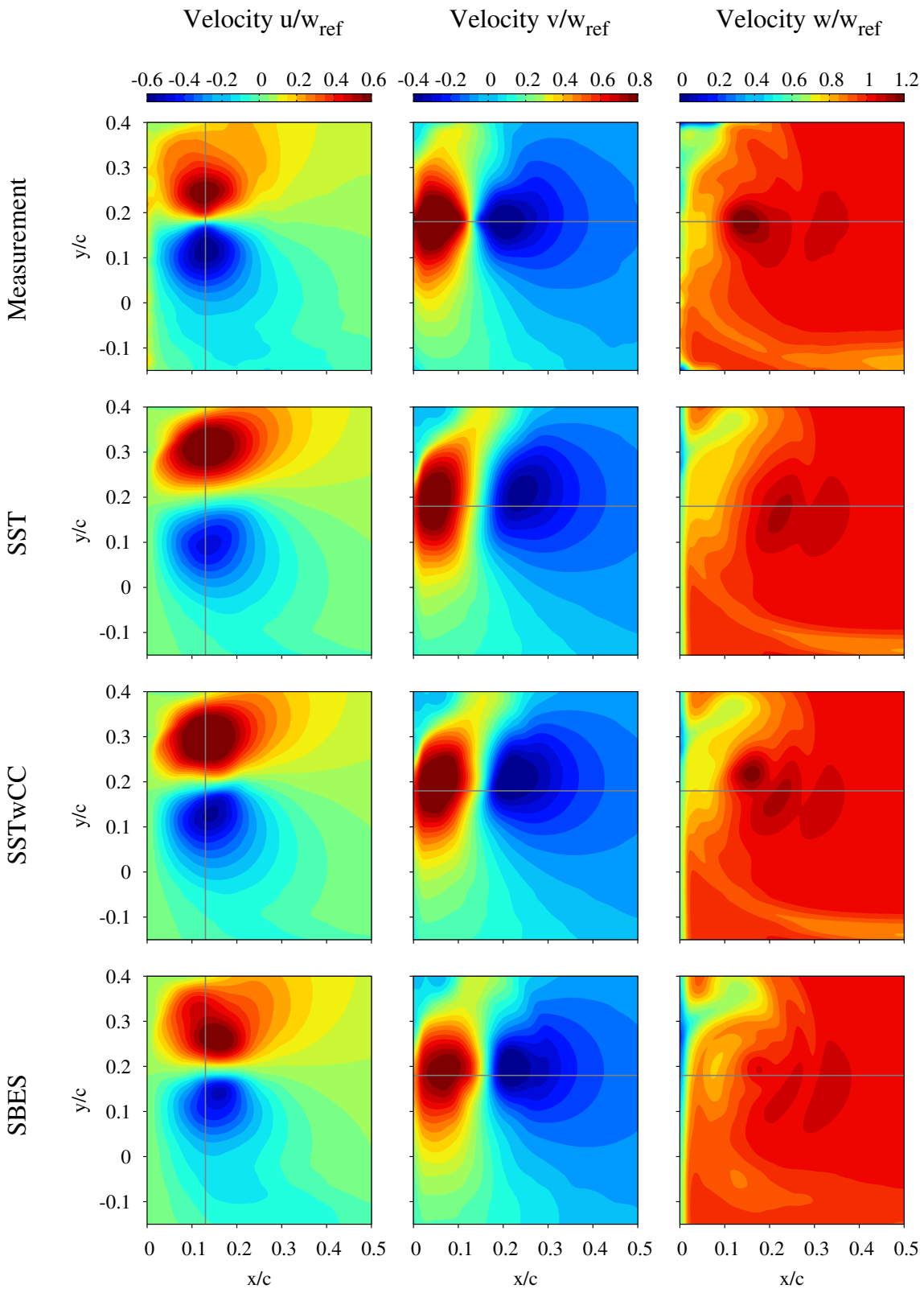

Figure A.2: Contour plot of the dimensionless velocity components u, v and w in measurement plane $z/c = 1.2$ for measurement [54] and single-phase simulations with different turbulence models.

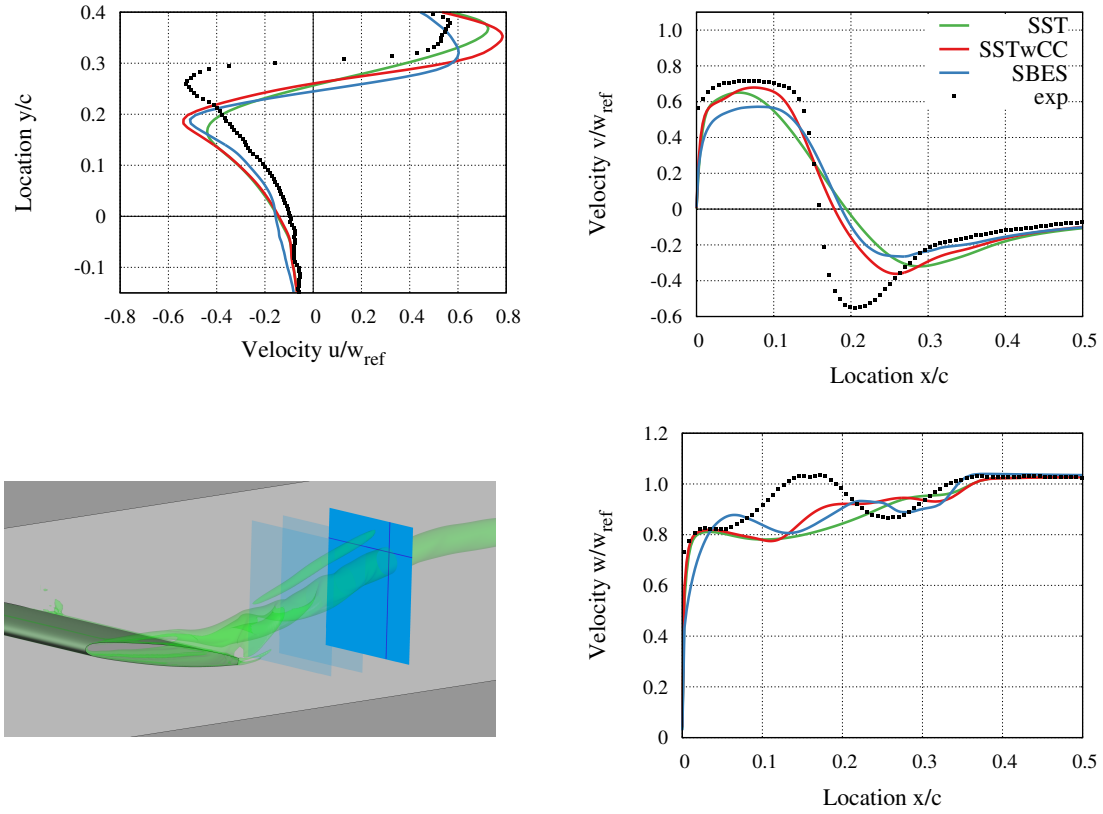

Figure A.3: Distribution of averaged u-, v- and w-component of the velocity along line in x- or y-direction, respectively, at measurement plane $z/c = 1.5$. The lines are located at $x/c = 0.159$ and $y/c = 0.307$. Experiments were performed by Dreyer et al. [54].

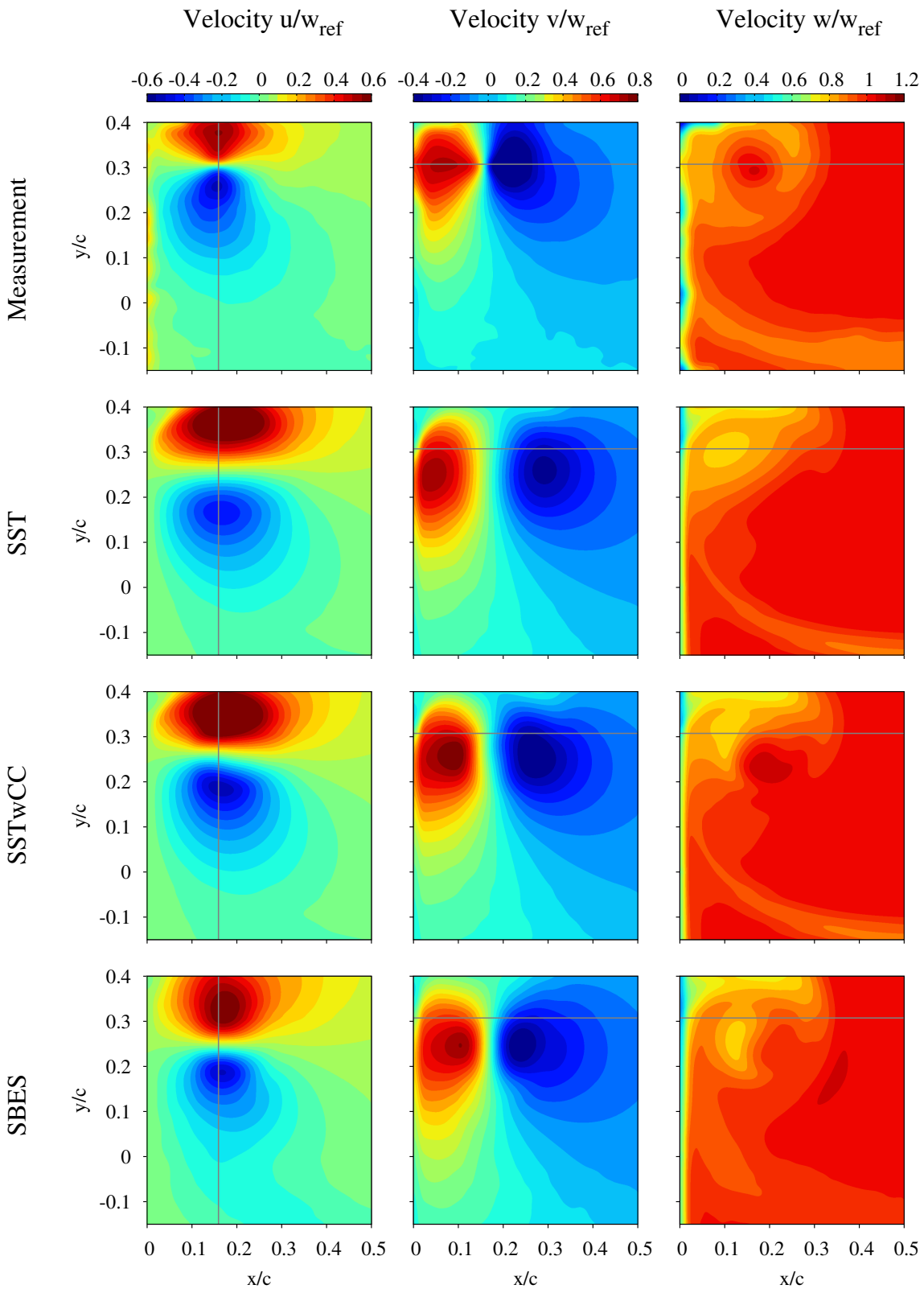

Figure A.4: Contour plot of the dimensionless velocity components u, v and w in measurement plane $z/c = 1.5$ for measurement [54] and single-phase simulations with different turbulence models.

B Discussion on Phase Shift for a Sine Wave

In this section, consequences of a phase shift between two quantities are discussed. As shown in figure 5.25, the cavitation volume oscillation can be approximated by a sine wave:

$$V_{c,DT}(t) \approx y_0 \sin(\omega t + \phi_0) + \Delta y \tag{B.1}$$

Therein, y_0 denotes the amplitude, ω the angular frequency, ϕ_0 the phase and Δy takes into account that the average cavitation volume is above zero. As the phase is not relevant for the following explanations it is set to zero. As already discussed in section 5.2, the link between cavitation volume and discharge is given by continuity equation 2.9:

$$\frac{dV_{c,DT}}{dt} = Q_{DT,out} - Q_{DT,in} \tag{B.2}$$

Furthermore, the cavitation volume is directly linked to the discharge at the draft tube outlet $Q_{DT,out}$ because the discharge at the inlet $Q_{DT,in}$ can be approximated to be constant. The time derivative of the cavitation volume $dV_{c,DT}/dt$ is a result of equation B.1:

$$\frac{dV_{c,DT}}{dt} = y_0 \omega \cos(\omega t) = y_0 \omega \sin(\omega t + 90°) \tag{B.3}$$

As cosine has a phase shift $\Delta\phi = -90°$ compared to sine, this phase shift should with reasonable agreement be applicable for the correlation between $V_{c,DT}$ and $dV_{c,DT}/dt$ or $Q_{DT,out}$. In figure B.1, cavitation volume is presented as function of $dV_{c,DT}/dt$. When no phase shift is applied, an elliptical shape can be observed that is similar to the correlation between $V_{c,DT}$ and $Q_{DT,out}$ in figure 5.37.

The actual correlation between $V_{c,DT}$ and $dV_{c,DT}/dt$ can be found when a phase shift $\Delta\phi = -90°$ is applied to $dV_{c,DT}/dt$, which is also displayed in figure B.1. Then,

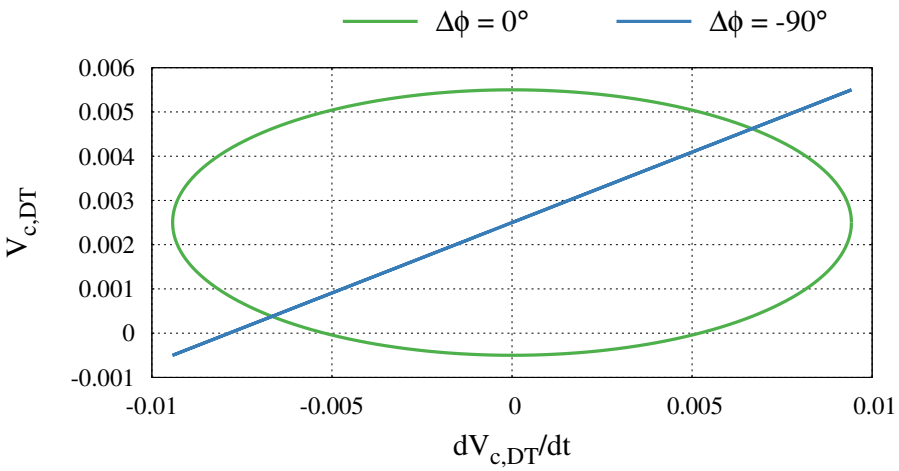

Figure B.1: Exemplary correlation between cavitation volume in draft tube and its first time derivative for shifted ($\Delta\phi = -90°$) and not shifted ($\Delta\phi = 0°$) $dV_{c,DT}/dt$. Oscillation of $V_{c,DT}$ and $dV_{c,DT}/dt$ are based on an ideal sine wave (equations B.1 and B.3).

a straight line can be observed that states a linear correlation between $V_{c,DT}$ and $dV_{c,DT}/dt$. Due to equation B.2, a linear relation can also be stated between $V_{c,DT}$ and $Q_{DT,out}$. This linear correlation is not perfectly met with the simulation results for the full load instability. As shown in figure 5.38, the phase shifted results are indeed not far away from a linear relation but actually show some propeller shape. The explanation for this behavior can be found in the fact that cavitation volume is limited at minimum to zero but has (almost) no limitation at maximum. Consequently, amplitude y_0 may not be constant during one instability cycle.

A variable amplitude is modeled by a sine wave. Compared to constant amplitude y_0, this leads to a smaller amplitude around minimum cavitation volume and a higher amplitude in the region of maximum cavitation volume. The resulting correlation between $V_{c,DT}$ and $dV_{c,DT}/dt$ is displayed in figure B.2. A propeller shape can be observed, which is similar to the observations from section 5.2. Consequently, the deviations from a linear correlation between $V_{c,DT}$ and $Q_{DT,out}$ can be traced back to variances from an ideal sine behavior.

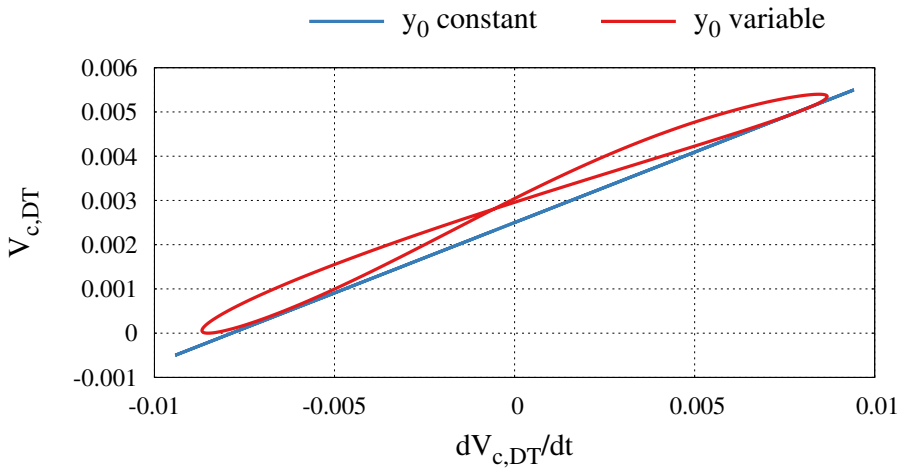

Figure B.2: Exemplary correlation between cavitation volume in draft tube and its first time derivative for shifted ($\Delta\phi = -90°$) $dV_{c,DT}/dt$. Comparison between constant amplitude y_0 and a variable amplitude that is modeled by a sine wave.

C Differential Equation for Negatively Damped Linear Oscillation

In this section, the solution of the differential equation for a negatively damped linear oscillation is presented. The differential equation for negative damping is according to equation 2.13:

$$\ddot{q} - \gamma\dot{q} + \omega^2 q = 0 \tag{C.1}$$

This equation is a homogeneous linear differential equation of the second order with constant coefficients. According to Papula [129] this type of differential equation has the following characteristic polynomial:

$$\lambda^2 - \gamma\lambda + \omega^2 = 0 \tag{C.2}$$

This results in three possible solutions of which the complex-conjugated case is relevant for the investigated case. Finally, this results in the following solution:

$$q = e^{\frac{\gamma}{2}t}\left[C_1 \sin\left(\frac{\sqrt{4\omega^2-\gamma^2}}{2}t\right) + C_2 \cos\left(\frac{\sqrt{4\omega^2-\gamma^2}}{2}t\right)\right] \tag{C.3}$$

To express the cavitation volume oscillation by this solution, two further modifications are necessary. First, a parameter Δy needs to be added that takes into account that the cavitation volume is not oscillating around zero but approximately the average cavitation volume. Secondly, a phase ϕ_0 needs to be introduced that offsets different phases between cavitation volume oscillation from the simulation and negatively damped oscillation. All in all, the following equation is used for the approximation of cavitation volume oscillation by a negative damping:

$$V_c = e^{\frac{\gamma}{2}t}\left[C_1 \sin\left(\frac{\sqrt{4\omega^2-\gamma^2}}{2}t + \phi_0\right) + C_2 \cos\left(\frac{\sqrt{4\omega^2-\gamma^2}}{2}t + \phi_0\right)\right] + \Delta y \tag{C.4}$$

Liste der bisher erschienenen IHS-Mitteilungen

Nr.	Jahr	Verfasser	Titel
1	1986		Beitrag zur 14. Sitzung des VDEW-Arbeitsausschusses „Meßmethoden in Wasserkraftanlagen”. ISBN 3-9802130-0-5
2	1989	Schneider, K. Eichinger, P.	Das Verhalten von Sicherheits-Drosselklappen. Modifikation des Standardcharakteristikenverfahrens zur Berechnung zeitlich zurückliegender Druckverläufe. ISBN 3-9802130-1-3
3	1989	Ruprecht, A.	Finite Elemente zur Berechnung dreidimensionaler, turbulenter Strömungen in komplexen Geometrien. ISBN 3-9802130-2-1
4	1990	Maurer, W.	Drehzahlregelung von Wasserturbinen mit Zustandsreglern. ISBN 3-9802130-3-X
5	1990	Acosta Del Carpio, H.	Das dynamische Verhalten von Kreiselpumpen niedriger spezifischer Drehzahl bei raschen Drehzahländerungen. ISBN 3-9802130-4-8
6	1990	Gronenberg, R.	Untersuchung des dynamischen Verhalten von Rückflußverhinderern unterschiedlicher Bauart. ISBN 3-9802130-5-6
7	1992	Eichinger, P.	Untersuchung des Reibungsverhaltens bei instationären Strömungsvorgängen in Rohrleitungen. ISBN 3-9802130-6-4
8	1993	Chihab, W. S.	Experimentelle und theoretische Untersuchung des Saugrohrs einer Kaplanturbine. ISBN 3-9802130-7-2
9	1994		Aktuelle Forschungsarbeiten des Instituts. ISBN 3-9802130-8-0
10	1994	Feyrer, R.	Kontinuierliche On-Line Berechnung der zulässigen Leistungsänderung in einem Pumpspeicherwerk. ISBN 3-9802130-9-9
11	1996	Zhang, Y.	Finite Elemente zur Berechnung instationärer Strömungen mit bewegten Wänden. ISBN 3-9804376-0-4

Nr.	Jahr	Verfasser	Titel
12	1997	Ginter, F.	Berechnung der instationären, turbulenten Strömung in hydraulischen Strömungsmaschinen. ISBN 3-9804376-1-2
13	1997		Beiträge zum Seminar „Kleinwasserkraft", Stuttgart, 10.10.97 ISBN 3-9804376-2-0
14	1998	Welzel, B.	Numerische Optimierung einer Axialturbine. ISBN 3-9804376-3-9
15	1999	Harbort, T.	Entwicklung eines echtzeitfähigen Simulationsprogramms zur Untersuchung instationärer Vorgänge in Wasserkraftwerken. ISBN 3-9804376-4-7
16	1999		Beiträge zum 2. Seminar „Kleinwasserkraft", Stuttgart, 01.10.99 ISBN 3-9804376-5-5
17	2000	Gentner, Ch.	Experimentelle und numerische Untersuchung der instationären Strömung in einer Axialturbine. ISBN 3-9804376-6-3
18	2000	Steibler, P.	Finite Element Methode zur numerischen Strömungsberechnung mit beliebigen Elementen. ISBN 3-9804376-7-1
19	2000	Lin, J.-C.	Überwachung von Wasserschlössern in Wasserkraftwerken mit Fuzzy-Control. ISBN 3-9804376-8-X
20	2000	Ott, Ch.	Entwurf und Simulation einer Staustufenregelung. ISBN 3-9804376-9-8
21	2001	Bauer, Ch.	Instationäre Berechnung einer hydraulischen Axialturbine unter Berücksichtigung der Interaktion zwischen Leit- und Laufrad. ISBN 3-9807322-0-7
22	2001	Liu, W.	Modeling of Swirling Turbulent Flows. ISBN 3-9807322-1-5
23	2002		Beiträge zum 3. Seminar „Kleinwasserkraft", Stuttgart, 05.10.01 ISBN 3-9807322-2-3

Nr.	Jahr	Verfasser	Titel
24	2001	Janetzky, B.	Ein Verfahren zur Berechnung instationärer Strömungen mit freier Oberfläche. ISBN 3-9807322-3-1
25	2002	Anz, R.	Systemidentifikation und Reglerselbsteinstellung in Wasserkraftanlagen. ISBN 3-9807322-4-X
26	2002	Maihöfer, M.	Effiziente Verfahren zur Berechnung dreidimensionaler Strömungen mit nichtpassenden Gittern. ISBN 3-9807322-5-8
27	2003		Beiträge zum 4. Seminar „Kleinwasserkraft“, Stuttgart, 19.09.03 ISBN 3-9807322-6-6
28	2003	Batrekhy, S.	Numerische und experimentelle Strömungsuntersuchungen an Rechen von Wasserkraftanlagen. ISBN 3-9807322-7-4
29	2005		Beiträge zum 5. Seminar „Kleinwasserkraft“, Stuttgart, 14.10.05 ISBN 3-9807322-8-2
30	2007	Helmrich, T.	Simulation instationärer Wirbelstrukturen in hydraulischen Maschinen. ISBN 978-3-9807322-9-1
31	2010	Lippold, F.	Zur Simulation von Fluid-Struktur-Wechselwirkungen mit flexiblen Kopplungsverfahren. ISBN 978-3-9812054-0-4
32	2011	Kirschner, O.	Experimentelle Untersuchung des Wirbelzopfes im geraden Saugrohr einer Modell-Pumpturbine. ISBN 978-3-9812054-1-1
33	2016	Ruopp, A.	Optimierung von symmetrischen Gezeitenströmungsturbinen und deren Analyse in großräumigen Gezeitenströmungsgebieten. ISBN 978-3-9812054-2-8
34	2016	Wang, H.	Very large eddy simulation for prediction of flow instabilities in turbomachinery. ISBN 978-3-9812054-3-5

Nr.	Jahr	Verfasser	Titel
35	2017	Neipp, A.	Ein- und zweistufige axiale Entspannungsturbine zur Energierückgewinnung. ISBN 978-3-9812054-4-2
36	2018	Stens, C.	Investigation of a fast transition from pump mode to generating mode in a reversible pump turbine. ISBN 978-3-9812054-5-9
37	2018	Krappel, T.	Turbulenzauflösende Strömungssimulation einer Francisturbine in Teillast. ISBN 978-3-9812054-6-6
38	2019	Schmidt, H.	Entwicklung eines Analyseverfahrens zur Kavitationsdetektion und Lokalisierung in hydraulischen Strömungsmaschinen. ISBN 978-3-9812054-7-3
39	2019	Schlipf, M.	Automatisierte Mehrzieloptimierung hydraulischer axialer Strömungsmaschinen. ISBN 978-3-9812054-8-0
40	2019	Brost, V.	Wiederaufbau des Stromnetzes mit einem Inselverbund aus Wasserkraftanlagen. ISBN 978-3-9812054-9-7
41	2019	Mössinger, P.	Numerische Untersuchung der Strömung bei transienten und instabilen Betriebszuständen von Francis-Turbinen. ISBN 978-3-9812054-00-9
42	2020	Tismer, A.	Entwicklung einer Softwareumgebung zur automatischen Auslegung von hydraulischen Maschinen mit dem Inselmodell. ISBN 978-3-948328-01-6
43	2020	Frey, A.	Untersuchung von periodischen und turbulenten Strömungsfluktuationen einer Francis-Turbine im Teillastbetrieb mit Laser-Doppler-Anemometrie. ISBN 978-3-948328-02-3

ISBN 978-3-948328-03-0